Spring 1-1-2015

Performance Quantification of Heliogyro Solar Sails Using Structural, Attitude, and Orbital Dynamics and Control Analysis

Daniel Vernon Guerrant
University of Colorado Boulder, dguerrant@gmail.com

PERFORMANCE QUANTIFICATION OF HELIOGYRO SOLAR SAILS USING STRUCTURAL, ATTITUDE, AND ORBITAL DYNAMICS AND CONTROL ANALYSIS

by

DANIEL VERNON GUERRANT

B.S., California Polytechnic State University at San Luis Obispo, 2005

M.S., California Polytechnic State University at San Luis Obispo, 2005

A thesis submitted to the

Faculty of the Graduate School of the

University of Colorado in partial fulfillment

of the requirement for the degree of

Doctor of Philosophy

Department of Aerospace Engineering Sciences

2015

This thesis entitled:
Performance Quantification of Heliogyro Solar Sails Using
Structural, Attitude, and Orbital Dynamics and Control Analysis
written by Daniel Vernon Guerrant
has been approved for the Department of Aerospace Engineering Sciences

_____
Dr. Dale A. Lawrence

_____
Dr. W. Keats Wilkie

Date_____

The final copy of this thesis has been examined by the signatories, and we find that both the content and the form meet acceptable presentation standards of scholarly work in the above mentioned discipline.

Guerrant, Daniel Vernon (Ph.D., Aerospace Engineering Sciences)

Performance Quantification of Heliogyro Solar Sails Using Structural, Attitude, and Orbital Dynamics and Control Analysis

Thesis directed by Professor Dale A. Lawrence

Solar sails enable or enhance exploration of a variety of destinations both within and without the solar system. The heliogyro solar sail architecture divides the sail into blades spun about a central hub and centrifugally stiffened. The resulting structural mass savings can often double acceleration verses kite-type square sails of the same mass. Pitching the blades collectively and cyclically, similar to a helicopter, creates attitude control moments and vectors thrust. The principal hurdle preventing heliogyros' implementation is the uncertainty in their dynamics. This thesis investigates attitude, orbital and structural control using a combination of analytical studies and simulations. Furthermore, it quantifies the heliogyro's ability to create attitude control moments, change the thrust direction, and stably actuate blade pitch. This provides engineers a toolbox from which to estimate the heliogyro's performance and perform trades during preliminary mission design. It is shown that heliogyros can create an attitude control moment in any direction from any orientation. While their large angular momentum limits attitude slewing to only a few degrees per hour, cyclic blade pitching can slew the thrust vector within a few minutes. This approach is only 13% less efficient than slewing a square sail during Earth escape, so it does not offset the overall acceleration benefits of heliogyros. Lastly, a root pitch motor should be able to settle torsional disturbances within a few rotations and achieve thrust performance comparable to that of flat blades. This work found no significant dynamic hurdles for heliogyros, and it provides key insight into their practical capabilities and limitations for future mission designers.

DEDICATION

To my wife, Tania, and my son, Carter.

ACKNOWLEDGEMENTS

I would like to thank:

Dr. Dale Lawrence for all his guidance and insight and for never letting me get away with anything unsubstantiated or imprecisely worded as my advisor.

Dr. W. Keats Wilkie for spearheading heliogyro research at NASA, acting as my NASA mentor, and hosting me for two internships at NASA Langley Research Center.

Dr. Jay Warren at NASA Langley Research Center for guidance with structural dynamics and corroborative finite element simulation work in Abaqus.

Andy Heaton (NASA Marshall Space Flight Center) and Dr. Laura Jones (NASA Jet Propulsion Laboratory) for guidance in spacecraft mission design and attitude control and for hosting me for internships.

the NASA Office of the Chief Technologist for supporting this work with Space Technology Fellowship NNX11AM89H.

CONTENTS

TABLES

FIGURES

NOMENCLATURE

a	semi-major axis [km]
a^*	characteristic acceleration [mm/s^2]
a_v	acceleration along the spacecraft velocity vector [mm/s^2]
A	state-space system dynamics matrix
A_s	total sail area [m^2]
$\hat{\boldsymbol{b}}_x$	body frame axis (see Table 1.3)
B	state-space system control matrix
$\mathcal{B}$	denotes body frame (see Table 1.3)
c	blade chord [m]
C	state-space system observation matrix
C_s	coefficient of RCD specular reflectivity
C_d	coefficient of RCD diffuse reflectivity
$\hat{\boldsymbol{d}}_x$	despun frame axis (see Table 1.2)
D	state-space system feed-through matrix
$\mathcal{D}$	denotes despun frame (see Table 1.2)
f	true anomaly [deg, rad]
f_n	nth rung Fourier integrand
f_{RCD}	fraction of the blade area covered in RCD
$\boldsymbol{F}$	net spacecraft solar radiation pressure (SRP) force vector [N]
h	sail membrane thickness [m]
i	blade number index
I	rigid-body spacecraft principal mass moment of inertia [kg·m^2]

J_n	nth rung mass moment of inertia [kg·m^2]
k	harmonic number
K	stiffness or control gain [Nm/rad, Nms/rad]
$\hat{\boldsymbol{l}}$	local horizontal with respect to the Sun and coplanar with $\boldsymbol{v}$ (see Table 1.1)
$\mathcal{L}_i$	denotes ith blade frame (see Table 1.4)
m	total spacecraft mass [kg, g]
$\boldsymbol{M}$	net spacecraft SRP moment vector [Nm], subscript "d" indicates desired moments
n	finite element node/rung index (always subscripted) or orbit mean motion [rad/s]
N	number of finite elements
N_b	number of blades
N_{bat}	number of battens on each blade excluding blade tip
$\hat{\boldsymbol{p}}$	reference axis for clock angle (see Table 1.1)
P	Solar radiation pressure [Pa] (P_0 = 4.563e−6 Pa at 1 AU)[56]
$\boldsymbol{r}$	orbit position vector [km]
R	heliogyro blade radius/span [m]
$\boldsymbol{s}$	Sun-spacecraft vector, coincides with $\boldsymbol{r}$ in heliocentric orbits (see Table 1.1)
$\mathcal{S}$	denotes Sun frame (see Table 1.1)
t	time [s]
t_∞	time to escape [d]
T_n	nth rung spanwise tension [N]
$\boldsymbol{u}$	state-space system control input vector
U_n	root-to-quarter-point transfer function
V_n	input-voltage-to-quarter-point transfer function

v	laser Doppler vibrometer velocity output time history [μm/s]
$\boldsymbol{v}$	orbit velocity vector [km/s]
w	controller bandwidth [rad/s]
x	spanwise position [m]
$\boldsymbol{X}$	pitch and pitch rate state vector [rad, rad/s]
y	in-plane, chordwise position from centerline [m]
$\boldsymbol{Y}$	state-space system output vector [rad, rad/s]
z	out-of-plane position [m]
α_{xx}	profile amplitude [rad, deg], subscript "*co*" = collective, "*hp*" = half-p, "*cy*" = cyclic
α_n	linear model amplitude coefficient for the *n*th rung [rad]
$\boldsymbol{\alpha}$	vector of linear model amplitude coefficients [rad]
$\alpha_n^{(k)}$	cosine coefficient of the *k*th harmonic for the *n*th rung [rad]
$\beta_n^{(k)}$	sine coefficient of the *k*th harmonic for the *n*th rung [rad]
γ	sail cone angle/Sun angle, angle between $\boldsymbol{s}$ and $\hat{\boldsymbol{d}}_1$ [rad, deg]
γ^*	Sun angle for maximum lateral thrust, $\gamma^* = \sin^{-1}(\sqrt{3}/3) = 35°$ (Ref. 56)
δ	clock angle between $\hat{\boldsymbol{p}}$ and $\hat{\boldsymbol{d}}_3$ [rad, deg]
ϵ	escape factor
ζ	damping ratio
η	optical efficiency
θ	blade pitch, subscript *n* for *n*th rung or *i* for *i*th flat blade [rad, deg]
κ	blade material damping coefficient [$\mathrm{Nm^2s/rad}$]
λ_1	blade root flap bending angle [rad, deg]
μ	Earth's gravitational parameter [398,600.4415 $\mathrm{km^3/s^2}$]

ρ	sail membrane density [kg/m^3]
σ_s	sail system loading [g/m^2]
σ_n	*n*th rung spanwise stress [Pa]
τ	torque about the blade twist axis [Nm]
υ_n	*n*th rung vertical membrane deflection angle [rad]
ϕ	harmonic phase angle [rad]
ϕ_{xx}	half-p (*xx* = *hp*) or cyclic (*xx* = *cy*) phase angle [rad, deg]
χ_i	*i*th blade angle relative to blade 1 in the rotation plane, $\chi_1 = 0$ [rad, deg]
Ψ	in-plane moment M_{23} azimuth angle [rad, deg]
ψ_i	*i*th blade azimuth angle in the spin plane [rad, deg]
ω	spin axis precession rate [rad/s]
ω_b	base or first harmonic frequency [rad/s]
Ω	heliogyro spin rate [rad/s, RPM]

Bold indicates a vector. Hat notation indicates a unit vector. Delta Δ indicates a difference.

CHAPTER 1. INTRODUCTION

A. Motivation for Solar Sailing

Mankind has been successfully exploring the solar system for over half a century almost exclusively with chemical propulsion and, in a handful of cases, with electric propulsion. The principal limitation of both these systems is their finite propellant supply, which caps the amount of energy they are able to impart to change a spacecraft's orbit. There are many conceivable missions both within the solar system and to interstellar destinations that are either impractical or impossible using chemical or electric propulsion. Solar sails offer an alternative approach with the promise to greatly enhance our ability to explore, understand, and ultimately expand into space beyond the limitations of traditional propulsion.

Solar sails use the direct momentum transfer of solar photons to generate thrust, thus they have an unlimited supply of propellant. Large reflective membranes are deployed and oriented to direct thrust in the desired direction. To a first order approximation, the thrust vector is normal to the reflective surface. Their chief limitation is the tiny solar radiation pressure (SRP) available, only 4.56 μPa at 1 AU.[56] Therefore, the solar sail must either be extraordinarily large to achieve higher thrust or the mission must be extraordinarily long to allow time for the solar sail to impart the required energy. Ref. 50 gives an overview of mission concepts that are enabled or enhanced by solar sails, divided into two categories. The first are high-energy destinations such as Solar Polar Orbiter (SPO) that achieves a high heliocentric inclination to image the solar poles or destinations in the Kuiper Belt, Oort Cloud, or interstellar space. The second mission type uses the continuous thrust solar sails provide to maintain novel orbits often called "non-Keplerian". Some example missions are Geostorm (displace the Earth-Sun L1 point sunward for increased solar storm warning time), GeoSail (continuously rotate the argument of perigee of a highly

elliptical orbit to maintain apogee in the Earth's magnetic tail), and Polesitter (hover above one of the Earth's poles for continuous communication or remote sensing coverage).

B. Solar Sail Architectures and History

Solar sail architectures have traditionally fallen into three categories, examples of which are shown in Figure 1.1. The first and most studied architecture is square with two cross booms I call "kite sail". Notable recent examples include two 20-meter ground demonstration test articles developed for the NASA In-Space Propulsion Technology Program, ca. 2005.[40] One of these designs, shown in Figure 1.1a, was further developed into the Sunjammer concept.[4,5] Additionally, several nanosatellite CubeSat examples exist including NASA Marshall Space Flight Center's (MSFC) NanoSail-D,[3,41] the German Space Agency's (DLR) Gossamer program,[25] the Planetary Society's LightSail-1,[6,15,39] and the Surry Space Centre's CubeSail.[46] The principal advantage of kite sail designs is that deployment of their primary sail-supporting structures is rigid enough to ground test prior to space flight. This is a huge risk-mitigation factor for early solar sails. As a square sail's area grows, the mass of supporting structure—generally deployable booms or trusses—begins to dominate the overall mass of the sail system, and it becomes increasingly difficult to prevent buckling. This is the chief drawback of the kite sail architecture. An additional complicating factor is acreage management of the very large and delicate sail membranes. Manufacture, ground handling, packaging, and deployment of expansive sail membranes only a few microns thick are extremely delicate and risky operations.

Another solar sail architecture is the spinning disk sail. The disk sail deploys and flattens the membrane with centrifugal forces alone, eliminating the massive booms of kite-type sails. This makes the disk sail, in principal, the most efficient and lightest solar sail. Chief disadvantages are the same deployment and packaging issues associated with kite sails and the difficulty of attitude

control; however, this architecture is the only controlled solar sail spaceflight example to date. The Japan Aerospace Exploration Agency (JAXA) IKAROS solar sail, launched in 2010 and shown in Figure 1.1b, successfully demonstrated an innovative spinning membrane control approach using thin film liquid crystal devices (LCDs) integrated into the perimeter of the sail membrane. These LCDs switch the local reflectivity between diffuse and specular states, changing the resulting solar radiation pressure acting on those portions of the sail. Synchronizing switching of the LCDs with the sail spin rate can generate inertially-fixed torques for two-axis attitude control.[24] While a completely successful demonstration, IKAROS' net acceleration is orders of magnitude below that necessary for solar-sail science applications (shown later).

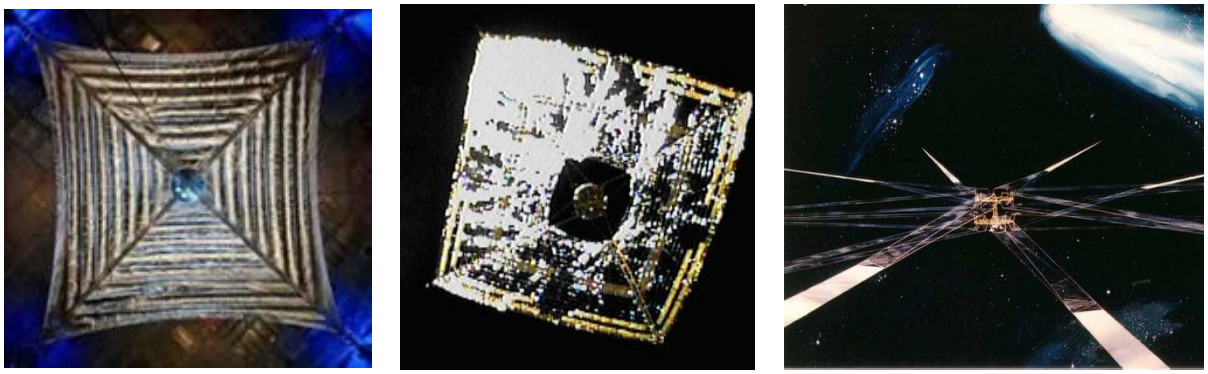

a) L'Garde 20 m ground demonstrator (2005)[40] **b) JAXA 14.7 m IKAROS in flight (2010)[64]** **c) JPL 17 km heliogyro concept (1978)[54]**

Figure 1.1: Example solar sail architectures

The third "canonical" solar sail architecture is the heliogyro, first proposed by Richard MacNeal in 1967.[51] The heliogyro is a helicopter-like, spinning solar sail that divides the membrane into several very high aspect ratio blades spun about a central hub. Changing the blade pitch collectively (all blades at a constant pitch) and cyclically (sinusoidally with blade azimuth in the rotation plane), controls the attitude and thrust vector. The blades stow compactly on spools and then slowly unrolled during deployment, aided by centrifugal forces. This simple deployment and packaging concept straightforwardly scales to extremely large sail areas. Heliogyros possess

the primary advantage of the spinning disk sail, namely low areal density, while avoiding many of the difficulties associated with stowage and deployment of large membrane areas.

Despite these compelling benefits, few heliogyro designs exist in literature. NASA Jet Propulsion Laboratory (JPL) conducted the most in-depth heliogyro study to date in the 1970s for an ambitious Comet Halley rendezvous mission.[21,22,37,54,62] Their final design featured a dozen blades, each 8 m by 7500 m, in two tiers as shown in Figure 1.1c. Ultimately, NASA selected a solar electric propulsion approach over the heliogyro, due primarily to the perceived high risk associated with unproven solar sail technology.[21] NASA eventually canceled the entire Halley mission due to cost overruns.[56] Later, a MIT design team conducted a study in 1989 as an entry into a solar sail race to Mars for the Columbus Quincentenary Commission.[7] One of the original MIT design team members subsequently performed further heliogyro blade control and dynamics investigations.[8,9] More recently, CU Aerospace and the University of Illinois studied an extremely large heliogyro concept starting in 2003 that they dubbed Ultrasail.[12,13] They worked on a CubeSat demonstration mission to deploy a 250 m long strip of sail material between two CubeSats and investigate the dynamics of a single heliogyro blade.[14]

C. Coordinate Reference Frames

Heliogyros are complex mechanical systems with many moving parts rotating and deforming with respect to each other, so I use several coordinate frames herein. First, the Sun frame $\mathcal{S}$ first axis is the Sun-spacecraft vector $\boldsymbol{s}$, and the spacecraft orbital velocity vector $\boldsymbol{v}$ anchors the frame's rotation about this axis. This is done by restricting the second axis, the local horizontal with respect to the sun $\hat{\boldsymbol{l}}$, to lie in the orbit plane and in the same semicircle as $\boldsymbol{v}$. In a circular, heliocentric orbit, $\hat{\boldsymbol{l}}$ is coincident with $\boldsymbol{v}$, but this more general definition holds in eccentric and planet-centric orbits. The vector $\hat{\boldsymbol{p}}$ completes the right handed coordinate system. In heliocentric

orbits, $\hat{\boldsymbol{p}}$ is coincident with the orbit angular momentum. This frame is summarized in Table 1.1, and it can be considered inertial on the time scales of structural and attitude dynamics analysis.

Table 1.1: Sun coordinate frame $\mathcal{S}$: $\{\hat{s}, \hat{l}, \hat{p}\}$

$\hat{\boldsymbol{s}}$	Sun-spacecraft unit vector, coincides with $\boldsymbol{r}$ in heliocentric orbits
$\hat{\boldsymbol{l}}$	local horizontal with respect to the Sun in the orbit plane and same semicircle as $\boldsymbol{v}$
$\hat{\boldsymbol{p}} = \hat{\boldsymbol{s}} \times \hat{\boldsymbol{l}}$	completes right-handed system, reference axis for clock angle δ

Next is the despun frame $\mathcal{D}$, defined by a two angle rotation from the Sun frame shown in Figure 1.2. For consistency in these and all subsequent heliogyro visualizations herein, the Sunlight is incident at a 45° angle from the left and the viewer is 15° above the $\hat{\boldsymbol{d}}_1\hat{\boldsymbol{d}}_2$ plane. From initial alignment (Figure 1.2a), rotate the despun frame by a clock angle δ about $\hat{\boldsymbol{d}}_1$ (Figure 1.2b) followed by a cone angle γ rotation about $\hat{\boldsymbol{d}}_3$ away from the Sun vector (Figure 1.2c). The cone angle is the angle between $\boldsymbol{s}$ and $\hat{\boldsymbol{d}}_1$, and the clock angle is between $\hat{\boldsymbol{p}}$ and $\hat{\boldsymbol{d}}_3$. These definitions are such that a positive γ with $\delta = 0$ produces a thrust component along $+\hat{\boldsymbol{l}}$ and $+\boldsymbol{v}$, thereby increasing orbit energy. A positive γ with $\delta = 90°$ produces a thrust component along $+\hat{\boldsymbol{p}}$, which could crank the inclination or line of nodes in a heliocentric orbit. These are both examples of utilizing a SRP force perpendicular to the Sun line that I call lateral thrust. Lateral thrust is maximized at a cone angle $\gamma^* = \sin^{-1}(\sqrt{3}/3) = 35°$ in flat sails with perfect reflection.[56]

Clock angle does not affect the net SRP thrust $\boldsymbol{F}$ and attitude control torque $\boldsymbol{M}$ in the despun frame since this angle is part of the rotation from Sun to despun frames. It does, however, set the direction of the attitude-dependent portion of lateral thrust in the Sun frame. The cyclic profile also produces lateral thrust, but its direction is set by the cyclic phase (explained in Chapter 1.D).

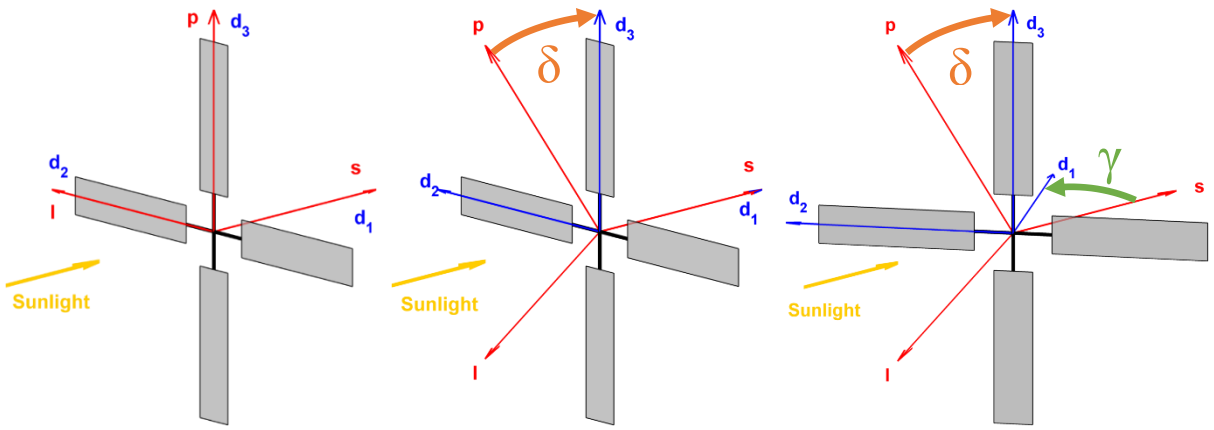

a) γ = 0° and δ = 0° **b) γ = 0° and δ = 45°** **c) γ = 35° and δ = 45°**

Figure 1.2: Despun and Sun coordinate frame rotations

The despun frame, described in Table 1.2, is similar to the spacecraft body frame, except the body frame rotates about $\hat{\boldsymbol{d}}_1$ at the nominal spin rate Ω. The second despun axis $\hat{\boldsymbol{d}}_2$ is defined through the rotation described above and is the reference axis for measuring first blade azimuth ψ_1. All heliogyro illustrations herein freeze rotation at $\psi_1 = 0$ (i.e. the first blade is aligned with $\hat{\boldsymbol{d}}_2$); however, the choice of blade to label "first" is arbitrary due to spacecraft symmetry. The despun frame is useful because the $\boldsymbol{F}$ and $\boldsymbol{M}$ of a given pitch profile are constant in this frame when averaged over the pitch profile period. This allows the despun frame results to be plugged into solar sail trajectory analyses in the literature, most of which assume an ideal, flat plate with perfect reflection. I call this the "flat sail", which could take any shape (e.g. square, disk, etc.). An idealized kite sail, the most commonly studied architecture, is a subset of flat sails.

Table 1.2: Despun coordinate frame $\mathcal{D}$: $\{\hat{d}_1, \hat{d}_2, \hat{d}_3\}$

$\hat{\boldsymbol{d}}_1$	primary spin axis, reference axis for cone angle γ
$\hat{\boldsymbol{d}}_2$	$\perp \hat{\boldsymbol{d}}_1$, coplanar with $\boldsymbol{s}$, reference axis for first blade azimuth ψ_1
$\hat{\boldsymbol{d}}_3 = \hat{\boldsymbol{d}}_1 \times \hat{\boldsymbol{d}}_2$	completes right hand system, reference axis for clock angle δ

Next is the body coordinate frame $\mathcal{B}$ described in Table 1.3, which relates to the despun frame by the first blade's azimuth angle ψ_1.

Table 1.3: Body coordinate frame $\mathcal{B}$: $\{\hat{b}_1, \hat{b}_2, \hat{b}_3\}$

$\hat{\boldsymbol{b}}_1$	axis to blade 1 mid-chord at the root
$\hat{\boldsymbol{b}}_2 = \hat{\boldsymbol{b}}_3 \times \hat{\boldsymbol{b}}_1$	completes right-handed system
$\hat{\boldsymbol{b}}_3$	major body axis assumed coincident with $\hat{\boldsymbol{d}}_1$

The last frame is the *i*th blade frame $\mathcal{L}_i$ described in Table 1.4, representing the flat or undeformed blade position. This relates to the body frame by a rotation about the spin axis from the first blade to the *i*th blade χ_i, and a rotation about that blade's long axis equal to the blade pitch at the root θ_i. This is the frame used for blade dynamics analyses and for calculation of the SRP force for attitude control investigations.

Table 1.4: Flat *i*th blade coordinate frame $\mathcal{L}_i$: $\{\hat{x}, \hat{y}, \hat{z}\}$

$\hat{\boldsymbol{x}}$	axis along blade span
$\hat{\boldsymbol{y}}$	axis along blade chord
$\hat{\boldsymbol{z}}$	blade normal, coincident with $\hat{\boldsymbol{d}}_1$ and $\hat{\boldsymbol{b}}_3$ when $\theta_i = 0$

The direction cosine matrices (DCMs) between frames combine the following single-axis rotation matrices:

$$\mathrm{ROT1}(\theta) = \begin{bmatrix} 1 & 0 & 0 \\ 0 & \cos\theta & \sin\theta \\ 0 & -\sin\theta & \cos\theta \end{bmatrix} \tag{1.1}$$

$$\mathrm{ROT2}(\theta) = \begin{bmatrix} \cos\theta & 0 & -\sin\theta \\ 0 & 1 & 0 \\ \sin\theta & 0 & \cos\theta \end{bmatrix} \tag{1.2}$$

$$\mathrm{ROT3}(\theta) = \begin{bmatrix} \cos\theta & \sin\theta & 0 \\ -\sin\theta & \cos\theta & 0 \\ 0 & 0 & 1 \end{bmatrix} \tag{1.3}$$

where θ represents the given angle and not blade pitch as used elsewhere. DCMs here use the notation ${}^{A}\boldsymbol{x} = [AB]\,{}^{B}\boldsymbol{x}$ where:

$$[\mathcal{DS}] = \mathrm{ROT3}(\gamma)\mathrm{ROT1}(\delta) \tag{1.4}$$

$$[\mathcal{BD}] = \text{ROT3}(\psi_1)\text{ROT1}\left(\frac{\pi}{2}\right)\text{ROT3}\left(\frac{\pi}{2}\right) \tag{1.5}$$

$$[\mathcal{L}_i\mathcal{B}] = \text{ROT1}(\theta_i)\text{ROT3}(\chi_i) \tag{1.6}$$

Note that $[\mathcal{BD}]$ is a single rotation of the first blade's azimuth angle. The two constant, π/2 rotations merely renumber the axes to get $\hat{\boldsymbol{b}}_3$ coincident with $\hat{\boldsymbol{d}}_1$. This is an axis numbering choice to reconcile coordinate systems used in disparate papers and has no physical effect.

D. Heliogyro Blade Pitch Profiles for Attitude and Thrust Control

Conventional spacecraft attitude actuators such as reaction wheels, thrusters, or magnetorquers are generally considered impractical on solar sails due to the sail's large mass moment of inertia, excessive propellant use (given a sail's typically long mission life), or the lack of strong magnetic fields in typical solar sail orbits. Therefore, solar sails preferentially use SRP for attitude control, sometimes supplemented by conventional means. They do this by offsetting the center of pressure (CP) from the center of mass (CM). Methods that shift the CM around the CP include a mass on a moveable boom[46,47,6568] or masses sliding along the sail deployment booms.[1,2,47,60] Alternatively, the CP is shifted relative to the CM, such as with moveable vanes,[1,2,5,47,65,66] membrane twisting/warping and translating,[47,65,66] membrane billowing,[23] and changing the local reflectivity.[11,24,58] These methods are limited in their ability to generate SRP attitude control moments—referred to herein as control moment authority (CMA)—because they affect a small portion of the sail's total mass or area and/or have a limited range of motion.

The heliogyro takes the concept of control vanes to its extreme; the entire sail is divided into moveable vanes. This gives the heliogyro a large CMA; however, spinning solar sails in general and heliogyros in particular have a very large angular momentum. On one hand, this makes them resistant to disturbance torques, but it also makes attitude maneuvers slow and

difficult. Additionally, a spinning sail's attitude control system must actuate at the spin rate in order to keep the control moment fixed in inertial space. IKAROS used liquid crystal devices (LCDs) that switched on and off instantly,[24] but a heliogyro will need mechanisms capable of continuously varying the blade pitch at rotation rates.

The father of the heliogyro, Richard MacNeal, suggested three blade pitch profiles for control in all six degrees of freedom: collective (blades at a constant pitch), cyclic (blades pitch sinusoidally once per revolution), and half-p (blades pitch sinusoidally once every two revolutions).[51,54] Figure 1.3 summarizes the effects of each of the three pitch profiles for the nominal, Sun-facing case ($\gamma = 0$). The first row in Figure 1.3 is a visualization of a four-blade heliogyro showing the direction of positive spin rate Ω, incident Sunlight direction, and force and moment vector components. Each blade's pitch (relative to the blade rotation plane) and the coordinate frame axes are also annotated.

Each profile is shown at the pitch amplitude yielding the largest force or moment in the useful direction per the "effect" row, assuming flat blades and perfect reflection. Collective yields the largest spin moment (M_1) at 35° blade pitch, as this angle has the largest lateral thrust on each individual blade. The half-p profile yields the largest in-plane moment (M_2 or M_3) at 75° pitch amplitude, as this amplitude balances the two competing goals for maximizing M_2: blade pitch should be close to zero above $\boldsymbol{d_2}$ (top half of the cycle) and close to ±90° below d_2 (bottom half of the cycle). Cyclic yields the largest lateral thrust (F_l or F_p) at 42° pitch amplitude, as this amplitude balances the two competing goals for maximizing F_l: blade pitch should be close to +35° above $\boldsymbol{l}$ (top half of the cycle) and close to −35° below $\boldsymbol{l}$ (bottom half of the cycle). In this Sun-facing case, note that the cyclic profile (Figure 1.3c) produces no net attitude control moment but does generate

thrust in the sail's rotation plane, a capability absent from most other sail architectures. As will be shown later, however, the cyclic profile can generate useful control moments in other situations.

	(a) Collective	(b) ½-Period Cyclic (Half-p)*	(c) 1-Period Cyclic (Cyclic)
Pitch Profile Illustrations	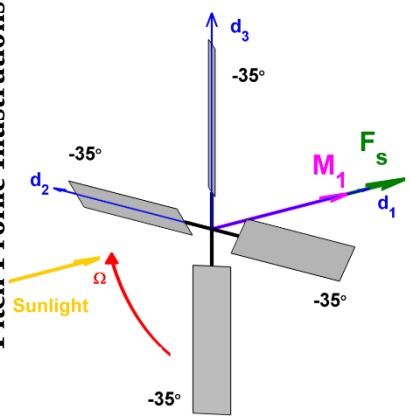	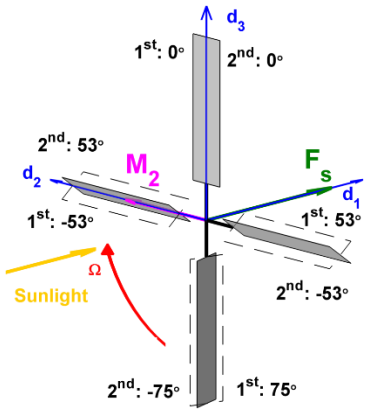	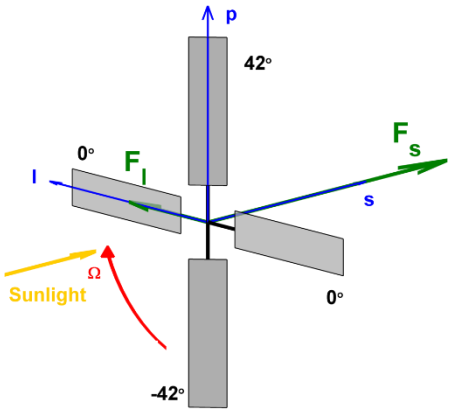
Effect	Spin-axis torque (M_1)	In-plane torque (M_2 or M_3)	Thrust perpendicular to the sun line (F_l or F_p), no torque
Use	Spin control during sail deployment as moment of inertia grows	Spin axis precession for attitude stabilization and slewing	Change thrust direction with lateral thrust (faster than slewing)

*The half-p profile period is two revolutions. Dashed lines indicate the blade position for the second revolution.

Figure 1.3: Heliogyro blade pitch profile descriptions for the Sun-facing case

It should be noted that these pitch profiles are not necessarily the best ways to achieve the desired force and moment effects. In infinitely stiff blades, the ideal pitch profile would step change between the competing goals listed in the previous paragraph. In reality, the blades have very little stiffness, so a sinusoidal oscillation is used to minimize excitation of structural modes. Waveforms somewhere between step functions and single-frequency sinusoids may be more efficient, even with flexible blades, a possibility I consider in Chapter 4.E.3.

E. Typical Solar Sail Operations

This dissertation is intended to be generally applicable, but it is important it be relevant to common solar sail missions and near-term heliogyro designs. Many solar sail missions share

operational modes such as maintaining cone angles of 0° or 35° for long periods, as these orientations beget the largest SRP thrust away from and perpendicular to the Sun line, respectively. I have selected several modes that appear frequently for near-term missions to test my algorithms and strategies. Table 1.5 describes several solar sail operational modes covering the most common missions (see Ref. 56 Ch. 6 and Ref. 50 for more detail).

Table 1.5: Typical solar sail mission operational modes

#	Mode	Goal	Cone Angle	Component to Maximize
1*	Sail deployment	Increase angular momentum to maintain spin rate as moment of inertia grows	0°	M_1
2	Earth-Sun Sub-L1 halo orbit	Displace Earth-Sun L1 point Sunward for increased solar storm warning time	0°	F_s
3	Planetary spiral in/out	Increase/decrease orbit energy	0° †	$\boldsymbol{F} \bullet \boldsymbol{v}$
4	Heliocentric spiral in/out	Increase/decrease orbit energy	±35°	$\pm F_l$
5a	Heliocentric cranking (coast)	Change the orbit inclination	±35°	$\pm F_p$
5b	Heliocentric cranking (slew)	Rapidly slew the spacecraft 70° twice per orbit at the orbit nodes	±35° to ∓35°	$\pm M_2$
6	Emergency attitude recovery	Recover from undesirably high cone angles	up to ±90°	$\mp M_2$

*Specific to spinning solar sails.
†Specific to heliogyros, which can slew the thrust with cyclic. Flat sails would slew 180° per orbit.[56]

These operational modes apply to solar sails generally, except as noted. The planetary spiral in/out (mode 3) requires that the solar sail thrust vector be slewed at orbit rates to maximize thrust along the velocity vector. The heliogyro's large angular momentum makes it inefficient to vector the thrust by spin axis precession in this mode, as much of the solar thrust is taken by precession moments. Instead, the thrust vector would typically be slewed using cyclic profiles with the heliogyro facing the Sun throughout, which is the topic of Chapter 3. Changes in cone angle require a $\pm M_2$ moment in the despun frame. Smaller $\pm M_3$ moments will also be needed to reject attitude disturbances and change the clock angle, but these do not drive the selection of the

blade pitch profile used in each mode. The pitch profile selection to achieve a desired attitude control moment is covered in Chapter 2. The list in Table 1.5 is not all-inclusive, and the approaches developed here would apply to other operational modes.

F. Research Questions and Expected Contributions

Before even a small heliogyro demonstrator could be undertaken, a deeper understanding of its dynamics will be needed. Blade pitch control is directly responsible for attitude control, which controls the heliogyro's trajectory. All of these problems are interrelated, so a study of one is incomplete without the other two. This work uses a combination of analytical and computational investigation to understand the heliogyro's ability to provide both attitude control and main propulsion. Throughout, I have striven to ground my research in realistic scenarios and to simplify the control algorithms' implementation, so that the tactics, strategies, and laws can be readily tailored to future missions. This work also provides key insight for future mission designers into the heliogyro's practical capabilities and limitations, hopefully facilitating a demonstration mission like the HELIOS concept of Chapter 1.G in the near future. In particular, this thesis addresses three essential questions about heliogyro dynamics and control:

1. How can one achieve a desired attitude and thrust with blade pitch profiles?

While there is a large body of work discussing attitude control of square- and disk-type solar sails, very little work on heliogyro attitude control has been done to date. The most applicable, non-heliogyro work uses tip vanes; however, these three-axis stabilized, so they avoid the heliogyro's complications of constant rotation and actuation. All work discussing heliogyro attitude control[13,36,51,52,54] is limited to Sun-facing and considers a single force or moment component rather than evolution of the whole force and moment vectors with changing attitude. Furthermore, the only combination pitch profile mentioned is collective plus cyclic,[51,52,54] and its

use is not explored in any detail. Unfortunately, undesirable force and moment components arise for non-zero cone angles, making it difficult to inertially fix the force and moment vectors with a change in attitude. Furthermore, attitude control via spin axis precession (M_2 and M_3) will be required throughout the mission to counter various disturbance torques.

These factors necessitate combination pitch profiles, and motivate the investigation of Chapter 2 into the heliogyro's ability to maintain attitude control at all orientations in all operational modes. This chapter investigates the answers to:

a) How do the forces and moments created by the pitch profiles of Figure 1.3 vary with attitude and can one combine pitch profiles to compensate for these changes?
b) Is it possible to meet multiple goals simultaneously, such as spin-up, lateral thrusting, spin axis precession, and disturbance torque rejection?
c) What combination pitch profile is optimal for each operational mode of Table 1.5, for example, to generate the most lateral thrust or slew the attitude the fastest?
d) How does the pitch profile map to the attitude control moment, what factors dominate this mapping, and is it possible to invert the mapping and determine the pitch profile required to meet a desired attitude control moment?

The CMA sets the upper bound on the heliogyro's ability to generate attitude control torques to change its attitude and spin rate. Chapter 2 presents a comprehensive understanding of how CMA varies with cone angle and desired forces, yielding quantitative trade-offs useful for determining the heliogyro's ability to counter disturbance torques and what trajectories it can follow. Within, I define and analyze three distinct attitude control tactics, each of which combines two pitch profiles. These tactics optimize the pitch profile to achieve three distinct attitude control goals: Spin Control, Precession, and Lateral Thrust. Taken together, they cover all the operational

modes of Table 1.5, providing quantitative constraints on heliogyro performance for mission design and simulation. I normalize these results to eliminate dependence on heliogyro dimensions or distance from the sun. This chapter helps mission designers determine if the heliogyro would even work for a given mission and whether or not it is an enabling architecture. Furthermore, these results inform blade controller design by indicating what the expected pitch amplitudes and pitch rates would be, and they inform blade construction by demonstrating the benefits of being able to illuminate both sides of the blade.

2. How does the heliogyro compare to a flat sail for Earth escape?

Solar sail trajectory studies almost exclusively assume a flat sail with a given characteristic acceleration and perfect reflection, such as Refs. 10, 16-19, 28, 47-50, 56, and many others. Attitude changes are usually assumed to be instantaneous, and in no case is there any relationship between thrust and slew rate. This is generally reasonable in heliocentric orbits with periods of many months; however, attitude control must be considered in planet-centric orbits. The maximum slew rates of the heliogyro are often slower than orbit rates, and there is a reduction in available thrust proportional to the desired slew rate. Fortunately, the heliogyro has an alternative, unique method of changing the thrust direction with cyclic profiles without having to slew.

Chapter 3 addresses the planet-centric trajectory most relevant to near-term heliogyro missions: Earth escape. Early technology demonstration missions like HELIOS will likely launch as a secondary payload for cost reasons, and ride-share opportunities to interplanetary space are scarce. Unfortunately, planet-centric orbit is the most difficult regime for solar sails to operate. Compared with heliocentric orbit, Earth orbit has much higher orbit rates, faster attitude control maneuvering, eclipsing, and a constantly changing incident sunlight vector relative to the orbit frame. Therefore, CHAPTER 3 will focus on this most difficult regime by comparing various

strategies for adding orbital energy with a heliogyro, in particular, the comparison between traditional solar sail strategies that slew the spacecraft, and heliogyro-specific strategies using cyclic profiles. This chapter addresses the pertinent questions of:

a) What is the optimal strategy to escape Earth orbit for a heliogyro?

b) Can the heliogyro slew fast enough to follow the prescribed trajectories?

c) How do strategies that slew the spacecraft compare to the non-slewing strategies when accounting for the performance penalty required to create attitude torques for slewing?

d) Is the heliogyro architecture preferred over a flat sail, considering the performance gain from less structural mass and the performance penalty of using cyclic profiles?

Chapter 3 confirms results with analytical performance metrics and orbital dynamics simulations. McInnes develops a non-dimensional quantity that I call the "escape factor" for use in comparing his strategies.[56] Chapter 3 develops new formulations of the escape factor and applies it to heliogyro-specific strategies for direct comparison with generalized, flat sail strategies to determine which is the better architecture for this application. I also present a new heliogyro escape strategy with locally optimal control of the cyclic pitch profile. Lastly, I derive a method of measuring the escape factor directly from simulation results for analytical validation, and I perform that validation with orbital simulations.

3. How can one control the pitch of highly flexible blades, ensuring stability?

The primary concern with heliogyros is the uncertainty associated with structural dynamics of controlling blade twist,[56] so I spent the most time on this topic. Heliogyro blades have three degrees of freedom (DOF) each: flap bending out the plane of rotation, lead-lag bending in the plane of rotation, and twist deformation about the radial axis. The centrifugal stiffening should effectively confine the flap and lead-lag bending to a couple degrees over the whole blade length,[53]

but twist dynamics pose a legitimate concern. Material stiffness and damping in twist are very small, so active control and damping of blade pitch appears to be required. As used herein, pitch is the local angle between the heliogyro blade and the plane of rotation, and twist is the local angle between the blade and the blade root (the undeformed, flat blade state).

Past work on blade twist stability has been limited to the linearized dynamics,[7,8,9,12,20,26,27,29-31,38,44,53] but nonlinear effects can substantially alter the torsional dynamics, even at moderate excitation amplitudes.[34] Chapter 4 develops a finite element model (FEM) for blade twist to investigate these issues, and it addresses the following questions:

a) Is control at the blade root sufficient? What form should a root control law take?
b) What is the steady-state blade shape for an arbitrary root pitch profile? In other words, what is the system's response to root excitation?
c) Does the nonlinear system experience frequency coupling, and at what frequencies?
d) How can one ensure adequate twist stability in the closed loop linear system? This is a necessary but not a sufficient condition for nonlinear stability.
e) Since material damping is presumed to be small, what is the relationship between material damping available and required controller bandwidth for stability?
f) How can one enhance blade stiffness for greater stability margin in a mass-efficient way?
g) Is it reasonable to assume flat blades and instantaneous changes in blade pitch profile for attitude and trajectory analyses?
h) If control at the blade root alone proves insufficient, what are some possible blade tip actuators? What would their performance and stability be?

Chapter 4 presents a control law for root pitch, analyzes the stability of the linearized system, adapts the control law for the nonlinear system, and examines some nonlinear stability

issues and their mitigation measures. It also covers some structural dynamics experiments performed in a vacuum chamber that give confidence that my FEM is reasonably representing the blade dynamics and to measure the structural damping. Lastly, Chapter 4 briefly introduces some additional control system concepts for the blade tip that are effective but do not appear necessary or practical at this time. I intend to show that there are no insurmountable structural dynamics issues with controlling blade twist from the root, and that this approach is feasible. The blade dynamics investigations also inform decisions about blade construction, and root motor and mechanism design. They give insight into methods of increasing blade stiffness and material damping. Furthermore, understanding the effects of small material damping is critical to controller design, as it drives the control system bandwidth requirement.

G. Heliogyro Design Concept Performance Comparison to Other Sail Designs

The uncertainty in heliogyro dynamics begs the question, "What are the potential benefits of heliogyros relative to other solar sails?" One can begin to answer that question by substituting a heliogyro into various other, well-developed solar sail concepts and estimating the performance enhancement. By "well-developed," I mean that the concept has a sufficiently detailed sail system mass budget in the literature to allow for substitution of a heliogyro. Many papers on solar sail trajectories use an arbitrarily low sail loading σ_s (the ratio of sail system mass to area) not based on any rigorous mass budget. While it is invalid simply to "plug in" a heliogyro to such scenarios, the heliogyro is an excellent way to achieve their ambitious sail loading.

For comparison with other architectures, I use the concept under joint development at NASA Langley Research Center (LaRC), JPL, MSFC, the University of Colorado, and Duke University. This mission is dubbed HELIOS, for High-Performance, Enabling, Low-Cost, Innovative, Operational Solar Sail.[71-74] HELIOS would be a small-scale technology demonstrator,

and it is designed to fit within the Evolved Expendable Launch Vehicle (EELV) Secondary Payload Adapter (ESPA). Where physical parameters are necessary in my analysis, I use the baseline HELIOS-like parameters listed in Table 1.6. For comparison, Table 1.6 also lists the parameters from the original, somewhat more ambitious, JPL Halley's Comet Rendezvous. Figure 1.4 illustrates the HELIOS deployment sequence, typical of heliogyros.

Table 1.6: Heliogyro reference parameters

Parameter	HELIOS[74]	Halley's Comet Rendezvous[54]	Units
Blade chord, c	0.75	8	m
Blade length, R	220	7500	m
Sail substrate	Mylar	Kapton	--
Sail substrate thickness	2.54	2	μm
Coatings	Al, Al	Al, Cr	--
Coating thickness	0.2	0.12	μm
Sail membrane density, ρ	1.6	1.5	g/cm^3
Sail membrane mass per blade	0.676	165	kg
Batten mass (each), m_{bat}	3	50	g
Number of battens per blade, N_{bat}	3	150	
Blade tip batten mass, $m_{tip\text{-}bar}$	0.007	1.667	kg
Blade assembly mass, m_{blade}	0.693	234	kg
Number of blades, N_b	6	12	
Sail deployment system mass, m_{truss}	8.3	1019	kg
Sail system mass, m_s	13.3	3837	kg
Bus mass, m_{bus}	5	861	kg
Total spacecraft mass, m	18.3	4698	kg
Spin rate, Ω	1	0.26	RPM
Sail area, A_s	990	625,000	m^2
Sail system loading, σ_s	13.4	6.1	g/m^2
Characteristic acceleration, a^*	0.46	1.12	mm/s^2

The characteristic acceleration a^* is an oft-used solar sail performance metric defined as the acceleration felt by the spacecraft with the sail normal to the Sun at 1 AU:[56]

$$a^* = (1+\eta)P_0\frac{A_s}{m} \tag{1.7}$$

where the SRP at 1AU is P_0 = 4.56e−6 Pa, and I use an optical efficiency η = 0.85.

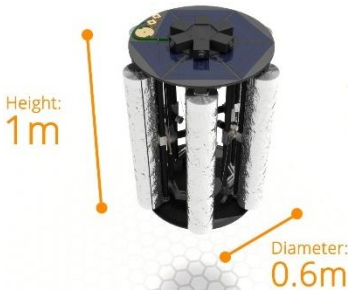

a) Stowed

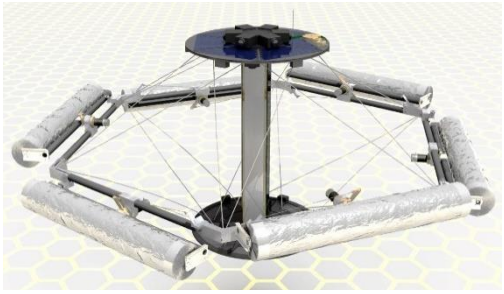

b) Hex truss is deployed and the bus sped up to about 5 RPM with magnetorquers.

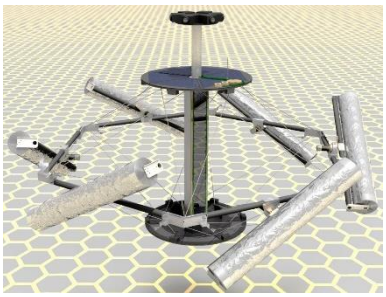

c) The blade reels are pitched collectively.

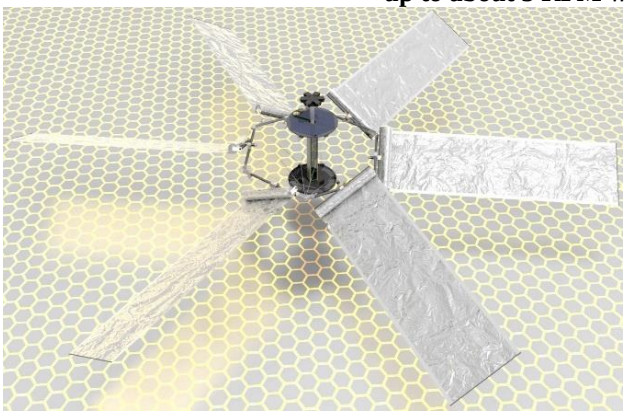

d) The blades are initially deployed rapidly at a constant angular momentum.

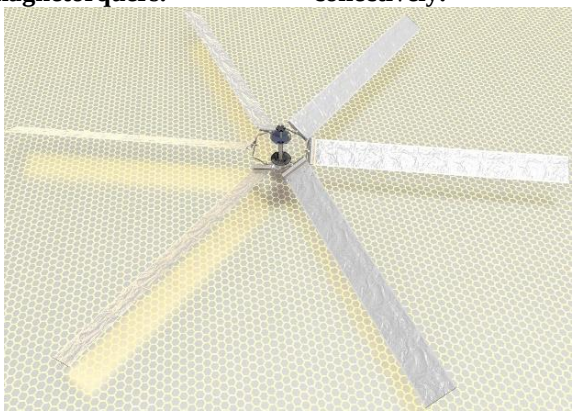

e) Initial deployment stops when spin rate drops to 1 RPM.

f) Blades continue deploying slowly (2 cm/s) using collective to add momentum and maintain 1 RPM.

g) Full deployment takes 2 to 3 hrs.

Figure 1.4: HELIOS deployment sequence screenshots*

*"HELIOS Advanced Solar Sail Concept," NASA Langley Research Center YouTube Channel, https://youtu.be/4F97NdwvmUM, December 12, 2014

Table 1.7 shows how a heliogyro like HELIOS can considerably improve upon past and future designs. I estimate the change in performance by separating the mass associated with each mission's sail system from the spacecraft bus and then adding in a corresponding mass for a HELIOS-like sail system. HELIOS' characteristic acceleration of 0.46 mm/s^2 is high enough for most near- to mid-term missions[50] and is higher than all the missions listed in Table 1.7. This table breaks the analysis into two parts: near-term (small-scale) and mid-term (large-scale). The former uses a heliogyro sail system loading of 13.3 g/m^2, representative of the current HELIOS design. The latter uses a loading of 7.2 g/m^2, representative of a scaled-up HELIOS design with more and larger blades that achieves loading similar to the original Halley's Comet mission.

Table 1.7: Performance enhancement of solar sail designs using a heliogyro

Mission	**Original**					**Heliogyro (same A_s)**		**Heliogyro (same m)**		**Heliogyro (same a^*)**	
Parameter:	A_s	m	m_s	σ_s	a^*	a^*	Δa^*	a^*	Δa^*	m	Δm
Units:	m^2	kg	kg	g/m^2	mm/s^2	mm/s^2	%	mm/s^2	%	kg	%
	Near-term (heliogyro σ_s = 13.3 g/m^2)										
NanoSail-D[*]	10	3.84	1.35	135	0.023	0.033	46	0.205	800	2.59	-33
Surrey CubeSail[46]	25	3.06	1.38	55	0.063	0.096	52	0.263	316	1.88	-38
IKAROS[64]	200	329	16	80	0.007	0.0072	4	0.028	306	317	-4
Sunjammer[†]	1200	41	30.1	25	0.245	0.373	53	0.464	90	18.3	-56
	Mid-term (heliogyro σ_s = 7.2 g/m^2)										
Geostorm[59]	5000	250	75	15	0.155	0.183	18	0.321	107	205	-18
SPO (tip vanes)[47]	19,770	598	272	14	0.256	0.327	28	0.486	90	427	-29
SPO (spar masses)[47]	26,797	681	356	13	0.305	0.400	31	0.559	83	455	-33
SPO (bus boom)[47]	28,392	722	397	14	0.305	0.415	36	0.588	93	455	-37

[*] Alhorn, Dean, "NSD Inertial Properties," internal NASA MSFC spreadsheet, May, 16, 2011, used with permission.

[†] Personal communication with Billy Derbes, Sunjammer program engineering consultant to L'Garde, Inc. in Tustin, California, on April 26, 2013. No published numbers available.

Table 1.7 has three comparisons using a heliogyro instead of the originally designed sail: 1) the change in characteristic acceleration a^* for the same sail area A_s, 2) the change in a^* using the same total mass m, and 3) the change in mass possible with the same a^*. The largest benefit comes from swapping in a heliogyro of the same mass as the original sail. This allows the sail to be much bigger, substantially increasing a^*. There is less improvement by substituting sails of the same area or characteristic acceleration, because the sail generally makes up a smaller portion of the spacecraft's overall mass for near- to mid-term missions. IKAROS in particular sees less benefit because the original sail system is less than 5% of the total mass.

While the heliogyro is at least 80% better than all the concepts of Table 1.7 for the same mass, heliogyros truly excel in the far-term missions. These missions generally require sails of many square kilometers making up over 80% of the total spacecraft mass. Deploying such large sails becomes extremely challenging for traditional kite sails due to such issues as boom buckling, packaging and deployment. The heliogyro, on the other hand, was designed from the onset with these large sail areas in mind, and it is the only practical means of deploying such expansive membranes thus far conceived. To increase size, merely add more spools, increase the blade chord, or roll longer blades around each spool. The membrane size is limited only by the available launch volume, so sail loading could approach the membrane areal density itself.

Succinctly, the principal advantage of heliogyros is their superior scalability to many square kilometers at low sail loading, and the principal concern is the perceived risk in their dynamics. This risk is compounded by the inability to ground test such expansive systems in a relevant environment. Therefore, I attempt to alleviate some of the principal concerns associated with practical operation of heliogyros with this thesis. I have not yet encountered any serious road blocks, and many concerns evaporate upon detailed examination of the first principals.

CHAPTER 2. ATTITUDE CONTROL VIA BLADE PITCHING

Heliogyros can generate attitude control torques by pitching the blades using the blade pitch profiles illustrated in Figure 1.3, either singly or in combination. While highly nonlinear, it is straightforward to calculate the net spacecraft force and moment vectors $\boldsymbol{F}$ and $\boldsymbol{M}$ given an arbitrary heliogyro orientation and blade pitch profile by summing each blade's SRP force and moment contributions. I wrote the `HGForce` algorithm to perform this forward mapping from blade pitch profile inputs to resultant $\boldsymbol{F}$ and $\boldsymbol{M}$ outputs. A combined trajectory and attitude control system, on the other hand, must produce desired $\boldsymbol{F}$ and $\boldsymbol{M}$ vectors by commanding suitable blade pitch profiles. That is, the inverse mapping of `HGForce` is needed to determine blade pitch profile commands for the lower-level pitch control system. Unfortunately, the inverse mapping is highly nonlinear and has many local minima, making an iterative gradient-based solution difficult. Also, the `HGForce` mapping is not locally onto, hence a given combination of desired $\boldsymbol{F}$ and $\boldsymbol{M}$ may not have a corresponding blade pitch profile solution. The expression for an individual blade pitch profile consists of independent parameters for the collective α_{co}, half-p α_{hp}, and cyclic α_{cy} amplitudes and the half-p ϕ_{hp} and cyclic ϕ_{cy} phases. These five parameters determine the ith blade's pitch θ_i as a function of its spin azimuth ψ_i through:

$$\theta_i(\psi_i) = -\alpha_{co} + \alpha_{hp} \sin\left[\frac{1}{2}\left(\psi_i - \phi_{hp} - \frac{\pi}{2}\operatorname{sign}\alpha_{hp}\right)\right] + \alpha_{cy}\sin\left(\psi_i - \phi_{cy}\right) \qquad (2.1)$$

$$\psi_i = \Omega t + \chi_i = \psi_1 + \chi_i \qquad \chi_i = 2\pi\frac{i-1}{N_b} \qquad (2.2)$$

The "$-\alpha_{co}$" and "$-(\pi/2)\operatorname{sign}\alpha_{hp}$" terms establish a convenient sign convention so that positive amplitudes α_{co} and α_{hp} yield positive moments M_1 and M_2 respectively and vice versa in the despun reference frame. This chapter presents the `HGForce` forward mapping and three variations of the inverse mapping optimized for a particular mission goal.

A. Forward Mapping with the `HGForce` Algorithm

For preliminary insight, `HGForce` makes several simplifying assumptions. First, the heliogyro blades are perfectly reflective on both sides. This implies no SRP force components tangential to the blade, but these forces are expected to be small. It also implies aluminization on both sides of the membrane, which could raise thermal emission concerns at orbits closer to the sun than Earth.[56] Second, it ignores self-shadowing (one blade shadowing another blade), which could occur when the heliogyro is near edge-on to the Sun. Third, `HGForce` is quasi-static; it does not take into account attitude dynamics. This means the cone angle, clock angle, and spin rate are assumed fixed, and `HGForce` varies the blade azimuth ψ to find the spin-averaged force and moment vectors.

Lastly, `HGForce` models the heliogyro as a set of flat blades with freedom in pitch alone. Chapter 4.E provides a detailed treatment of nonlinear blade twist dynamics. As will be shown in that chapter, it is possible to achieve net SRP force and moment vectors within 10% of those generated by a flat blade in most cases, and these control disturbances settle within a few minutes. The related assumption is that there is no in-plane (lead-lag) or out-of-plane (flapwise) bending, and the centrifugal tension is more effective at confining these motions than it is for twist. MacNeal derived an equation for the maximum flap angle, seen at the blade root, λ_1 under a static load (Eq. (18) of Ref. 51):

$$\lambda_1 = \frac{PR}{\sigma_1 h} \tag{2.3}$$

where σ_1 is the root tension stress. HELIOS would have a maximum flap bending away from the Sun of 0.04° at 1 AU using the parameters of Table 1.6. The lead-lag bending from blade pitching would be even smaller due to the smaller SRP components in this direction. This is just a static

load equation, but there is no forced excitation of these bending modes and little coupling expected. Therefore, this entire thesis ignores the flap and lead-lag bending.

For any given cone and clock angle relative to the Sun, the five pitch profile inputs produce six outputs: the net force and moment components on the spacecraft. Assuming perfect reflection on a flat blade, the SRP force on the *i*th blade is:

$$\boldsymbol{F_i} = 2A_iP(\hat{\boldsymbol{s}} \bullet \hat{\boldsymbol{z}}_{\boldsymbol{i}})^2\hat{\boldsymbol{z}}_{\boldsymbol{i}} = 2A_iP\left({}^{\mathcal{L}_i}s_3\right)^2\hat{\boldsymbol{z}}_{\boldsymbol{i}} \tag{2.4}$$

where A_i is the area of one blade, ${}^{\mathcal{L}_i}s_3$ is the component of $\hat{\boldsymbol{s}}$ normal to the blade in the blade frame. The *i*th blade normal $\hat{\boldsymbol{z}}_{\boldsymbol{i}}$ and Sun vector $\hat{\boldsymbol{s}}$ in the blade frame coordinates are:

$${}^{\mathcal{L}_i}\hat{\boldsymbol{z}}_{\boldsymbol{i}} = \left[0, 0, \text{sign}\left({}^{\mathcal{L}_i}s_3\right)\right]^T \tag{2.5}$$

$${}^{\mathcal{L}_i}\hat{\boldsymbol{s}} = [\mathcal{L}_i\mathcal{B}][\mathcal{B}\mathcal{D}][\mathcal{D}\mathcal{S}][0,0,1]^T \tag{2.6}$$

The "sign(${}^{\mathcal{L}_i}s_3$)" ensures the blade normal is out the dark side of the blade regardless of which side is illuminated. As will be shown throughout, being able to illuminate both sides of the blade is key to maximizing heliogyro performance. Combining the ψ_1 and χ_i rotations into a single ψ_i rotation about the third axis, the third, *z*-axis component of the Sun vector is:

$${}^{\mathcal{L}_i}s_3 = \cos\theta_i\cos\gamma - \sin\theta_i\sin\psi_i\sin\gamma \tag{2.7}$$

where θ_i is given by Eq. (2.1). The blade's SRP moment on the rotor hub in the blade frame is:

$${}^{\mathcal{L}_i}\boldsymbol{M_i} = [R/2\,, 0, 0]^T \times {}^{\mathcal{L}_i}\boldsymbol{F_i} \tag{2.8}$$

Use the rotation matrices (1.4) to (1.6) to express Eqs. (2.4) & (2.8) in the despun frame thus:

$$\begin{aligned} {}^{\mathcal{D}}\boldsymbol{F_i} &= 2A_iP\,\text{sign}\left({}^{\mathcal{L}_i}s_3\right)\left({}^{\mathcal{L}_i}s_3\right)^2\begin{bmatrix}\cos\theta_i\\ \sin\theta_i\sin\psi_i\\ -\sin\theta_i\cos\psi_i\end{bmatrix} \\ {}^{\mathcal{D}}\boldsymbol{M_i} &= RA_iP\,\text{sign}\left({}^{\mathcal{L}_i}s_3\right)\left({}^{\mathcal{L}_i}s_3\right)^2\begin{bmatrix}-\sin\theta_i\\ \cos\theta_i\sin\psi_i\\ -\cos\theta_i\cos\psi_i\end{bmatrix} \end{aligned} \tag{2.9}$$

At this point, the individual blade contributions may be summed per Eqs. (2.10) to find the instantaneous $\boldsymbol{F}$ and $\boldsymbol{M}$:

$$^{\mathcal{D}}\boldsymbol{F} = \sum_{i=1}^{N} {}^{\mathcal{D}}\boldsymbol{F_i} \qquad\qquad {}^{\mathcal{D}}\boldsymbol{M} = \sum_{i=1}^{N} {}^{\mathcal{D}}\boldsymbol{M_i} \tag{2.10}$$

Alternatively, the equations may be spin-averaged by assuming a constant spin rate Ω and integrating the $\boldsymbol{F}$ and $\boldsymbol{M}$ over two revolutions (the period of half-p) per:

$$^{\mathcal{D}}\boldsymbol{F} = \frac{2AP}{4\pi}\int_0^{4\pi} \operatorname{sign}\left({}^{\mathcal{L}_1}s_3\right)\left({}^{\mathcal{L}_1}s_3\right)^2 \begin{bmatrix} \cos\theta_1 \\ \sin\theta_1 \sin\psi_1 \\ -\sin\theta_1 \cos\psi_1 \end{bmatrix} d\psi_1 \tag{2.11}$$

$$^{\mathcal{D}}\boldsymbol{M} = \frac{RAP}{4\pi}\int_0^{4\pi} \operatorname{sign}\left({}^{\mathcal{L}_1}s_3\right)\left({}^{\mathcal{L}_1}s_3\right)^2 \begin{bmatrix} -\sin\theta_1 \\ \cos\theta_1 \sin\psi_1 \\ -\cos\theta_1 \cos\psi_1 \end{bmatrix} d\psi_1 \tag{2.12}$$

Spin-averaging make these values more representative of the long-term effect on the spacecraft attitude and trajectory. Note that Eqs. (2.11) & (2.12) integrate the azimuth and pitch of blade one then multiply by the total sailcraft area, which is simpler than separately integrating each blade and summing. Accounting for differences in notation and reference frames, these equations are identical to those derived in Ref. 51 except Eqs. (2.11) & (2.12) multiply by sign($^{\mathcal{L}i}s_3$) to account for illumination of either side of the blade. There is no explicit solution to the integral of Eqs. (2.11) & (2.12), so I approximate it numerically.

The forces and moments presented herein are spin-averaged then normalized per:

$$\bar{\boldsymbol{F}} = \frac{\boldsymbol{F}}{2AP\sin\gamma^*\cos^2\gamma^*} \qquad\qquad \bar{\boldsymbol{M}} = \frac{\boldsymbol{M}}{RAP\sin\gamma^*\cos^2\gamma^*} \tag{2.13}$$

so they are independent of the heliogyro's dimensions and distance from the Sun and hence universally applicable. Recall that $\gamma^* = 35°$ is the Sun angle yielding the most lateral thrust. The

force is divided by the maximum possible lateral thrust (a flat sail at $\gamma = \gamma^*$), and the moment is divided by the maximum possible spin moment ($\alpha_{co} = \gamma^*$ at $\gamma = 0$).

The equations for the resulting forces and moments are complex, involving several variables related through trigonometric functions, multiplied by and within other trigonometric functions, so the answer is rarely intuitive. I built the graphical user interface (GUI) shown in Figure 2.1 in Mathworks' Matlab to assist my own understanding of these concepts. This GUI has sliders for all five pitch profile parameters and all three angles in the rotation from sun to body frames. It also allows the camera to remain fixed in the Sun or despun reference frames. The box for blade aspect ratio only affects the visualization since the force and moment magnitudes are normalized per Eq. (2.13). At the bottom right are five push buttons allowing for various methods of capturing data and visualizing the heliogyro and its forces and moments in motion.

This GUI led to all the insights of this chapter, and it made visualization much easier than a two-dimensional representation or plot. As an example that I did not analyze in depth, pressing the "Plot 1 Pd." button plots the forces and moments over one or two revolutions. Cases with a cyclic profile showed small fluctuations in the forces and moments corresponding to the number of blades, so more blades minimized the amplitude of these fluctuations. Also, even numbers of blades experienced fluctuation in force but not moment components, while odd numbers of blades had fluctuating moment but not force components. The spin-averaged results depicted in this paper were always the same, but this phenomenon could excite structural modes and should be investigated further.

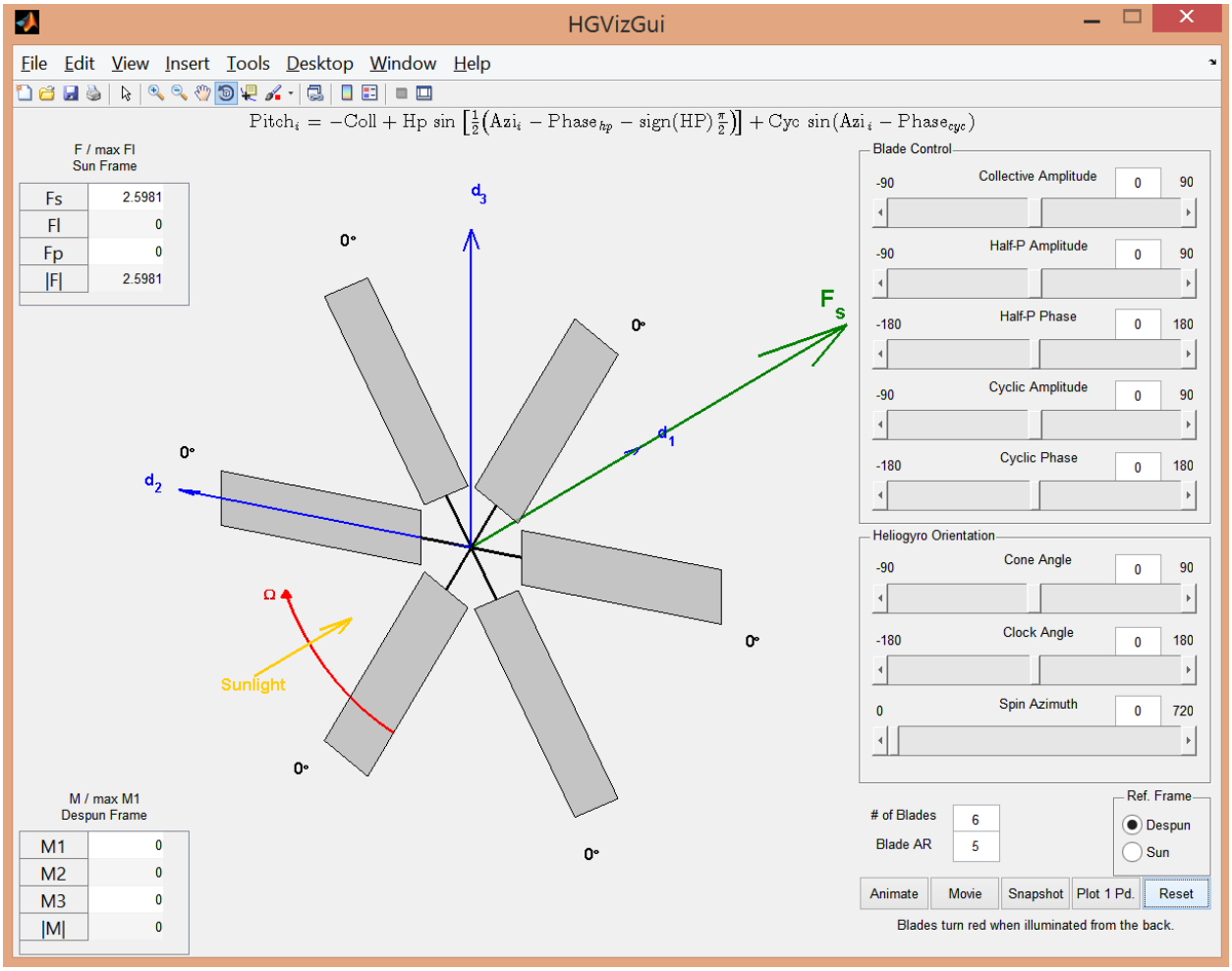

Figure 2.1: Heliogyro visualization GUI for `HGForce`

The achievable set of ***F*** and ***M*** constitute a compact sub-manifold of $\mathbb{R}^6$ of dimension at most five. This mapping is not directly invertible with only five pitch profile inputs; in particular, there is no independent control over the total force magnitude. One possible additional pitch profile parameter that I conceived but did not investigate I call "attenuate". It would be just like collective, except that each blade would alternate the sign of the blade pitch. When sun-facing, this would "shutter" the blades, reducing the solar thrust without producing any moments in systems with even numbers of blades. At face value undesirable, the ability to "turn the sail off" has many applications, including asteroid or comet rendezvous, station-keeping at sub-L1 for Geostorm,[48] and Earth escape (Chapter 3). This represents another unique capability of heliogyros.

A different method of making the inversion possible is to reduce the number of outputs by focusing on either the force or moment components rather than both. The next section formulates a limited inverse mapping for each attitude control tactic that restricts the problem to three inputs (two pitch profile amplitudes and one phase) and three outputs (attitude control moment components). These restricted inversions suffice for determining a set of locally optimal tactics for the mission modes identified in Table 1.5. They could also seed a more comprehensive global optimization.

B. Attitude Control Tactics

This chapter presents three tactics for generating attitude control moments that each combine two pitch profiles. I name the tactics Spin Control, Precession, and Lateral Thrust after their primary use, but they can each perform all three functions to some degree. For example, the Spin Control Tactic is best at changing the angular momentum about the spin axis $\boldsymbol{d_1}$, but it can also precess the spin axis or create lateral thrust. I use cylindrical coordinates for the moments in this chapter with the in-plane moment magnitude M_{23} and azimuth Ψ vice the components M_2 & M_3. The tactics can then maximize the in-plane moment along a desired azimuth.

Each attitude control tactic restricts the system to three inputs (two profile amplitudes and one phase), each of which primarily controls one of three outputs (M_1, M_{23}, and Ψ). Restricting the problem thus makes the control inversion possible. A multivariate linear regression of the forward mapping of `HGForce` can be solved for an approximate inversion that serves as the initial guess for Matlab's constrained minimization function `fmincon` that finds the exact control inputs (objective variables) for a desired moment vector $\boldsymbol{M_d}$ (objective function). Since Ψ is always achievable by varying the pitch profile phase, I set it as constraint. The objective functions are M_1 and M_{23}. If the desired moment magnitude is impossibly large, the function returns the largest

possible moment in the desired direction, which is the CMA in that direction. In this analysis, in-plane and spin moments are equally weighted, but other weights may be preferable.

1. *Spin Control Tactic*

One of the first steps after launch is to deploy the heliogyro's blades by slowly unreeling them from their stowage spools (mode 1 of Table 1.5). The deploying blades' increasing moment of inertia would slow the spin rate by conservation of angular momentum, so a collective profile is needed to add angular momentum and maintain spin rate. This would normally occur at cone angle $\gamma = 0°$ for maximum M_1, but disturbance torques may cause the spacecraft attitude to drift. Figure 2.2 shows the resulting moments for a 35° collective profile as the cone angle increases.

When $\gamma \neq 0°$, this profile generates an unwanted M_2 component, and M_1 drops to zero as the heliogyro points edge-on to the Sun ($\gamma = 90°$). Figure 2.2b illustrates this mechanism at a cone angle of 35°. The top blade is directly Sun-facing, while the bottom blade is angled away from the Sun at 70°. The pressure differential creates an M_2 moment in the same sign as γ, so it is important to note that this M_2 is destabilizing in that it would increase $|\gamma|$ during spin-up (vice-versa during spin-down). Therefore, active attitude correction is required during blade deployment. Fortunately, one can zero out the undesired M_2 and restore the desired M_1 with a "cyclic moment correction". This correction overlays a cyclic profile onto the collective with amplitude $\alpha_{\bar{c}y}$ and phase $\phi_{\bar{c}y} = 0$ or 180°. The $\alpha_{\bar{c}y}$ has the same sign as γ if $\phi_{\bar{c}y}$ is set to 180° and the opposite sign if $\phi_{\bar{c}y}$ is set to 0°. Furthermore, the 35° collective does not necessarily produce the largest M_1 when $\gamma \neq 0°$. Therefore, the exact value of the cyclic moment correction and optimal collective pitch must be determined by solving the nonlinear equations. Although it is more involved computationally, this is operationally simpler, smoother, and more reliable than periodically interrupting the spin up to restore the desired attitude with a separate slewing maneuver.

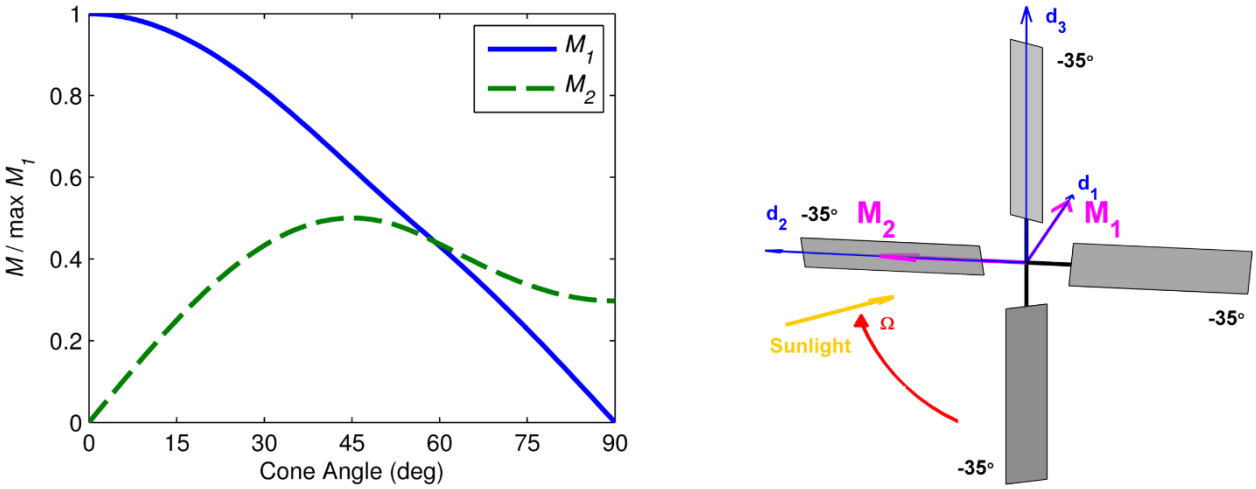

a) Moments **b) Example visualization at γ = 35°**

Figure 2.2: 35° collective profile moment variation with cone angle

Figure 2.3 shows the optimal collective profile with the cyclic moment correction applied. The required α_{cy}^{-} varies nearly linearly at a slope of about 2/3 the cone angle. This completely zeroes the unwanted moment M_2 (not shown) and largely restores the desired moment M_1 (blue line), even when γ = 90°. Figure 2.3b shows that the upper blade is now pitched away from the Sun and the lower blade towards the Sun exactly enough to remove the tipping-over moment.

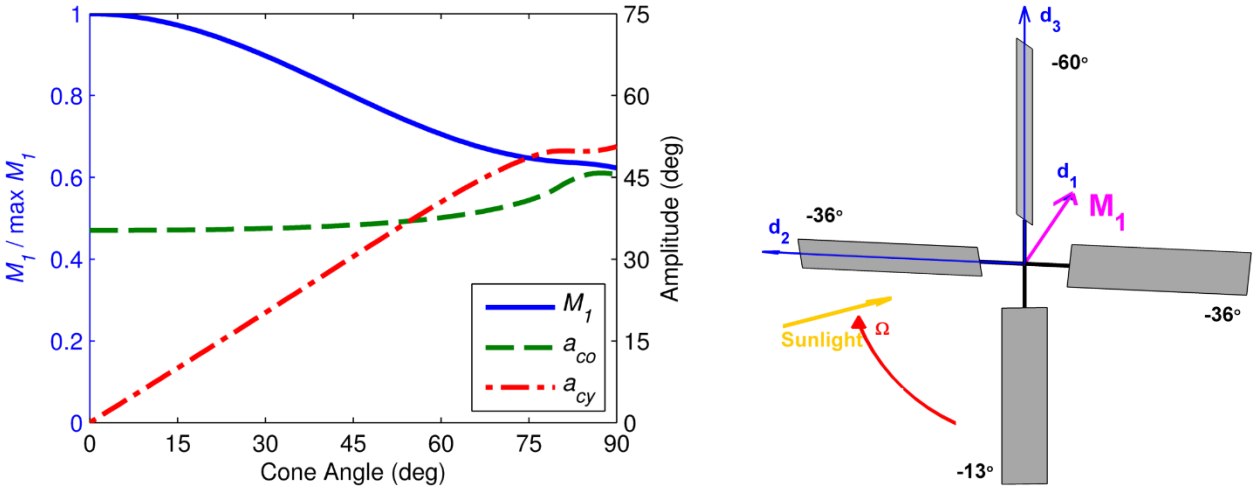

a) Variation with cone angle **b) Example visualization at γ = 35°**

Figure 2.3: Spin Control Tactic CMA about the spin axis with M_{23} = 0

So far, this tactic has only zeroed the in-plane moments about $\boldsymbol{d_2}$, but attitude control during blade deployment will require CMA in all in-plane directions to maintain desired attitude in the presence of disturbances. To provide these desired in-plane moments, one must add two cyclic

profiles together; the first (α_{cy}^{-} at ϕ_{cy}^{-} = 180°) is the cyclic moment correction described above to zero the unwanted in-plane moment, and the second (α_{cy}^{+}, ϕ_{cy}^{+}) generates the desired in-plane control moment. The net cyclic amplitude α_{cy} and phase ϕ_{cy} is calculated below, first by expanding the multiple angle trigonometric functions and considering that ϕ_{cy}^{-} = 0 or π always:

$$\begin{aligned}\alpha_{cy}\sin(\psi_i-\phi_{cy}) &= \alpha_{cy}^{+}\sin(\psi_i-\phi_{cy}^{+})+\alpha_{cy}^{-}\sin(\psi_i-\phi_{cy}^{-})\\ \alpha_{cy}(\cos\phi_{cy}\sin\psi_i-\sin\phi_{cy}\cos\psi_i) &\\ &= \alpha_{cy}^{+}(\cos\phi_{cy}^{+}\sin\psi_i-\sin\phi_{cy}^{+}\cos\psi_i)+\alpha_{cy}^{-}\cos\phi_{cy}^{-}\sin\psi_i\end{aligned} \tag{2.14}$$

Convert from polar (α_{cy}, ϕ_{cy}) to Cartesian (b_{cy}, c_{cy}) using $b_{cy} = \alpha_{cy}\cos\phi_{cy}$ and $c_{cy} = \alpha_{cy}\sin\phi_{cy}$:

$$\begin{aligned}b_{cy}\sin\psi_i-c_{cy}\cos\psi_i &= b_{cy}^{+}\sin\psi_i-c_{cy}^{+}\cos\psi_i+b_{cy}^{-}\sin\psi_i\\ &= (b_{cy}^{+}+b_{cy}^{-})\sin\psi_i-c_{cy}^{+}\cos\psi_i\end{aligned} \tag{2.15}$$

Collect sines and cosines of ψ_i and cancel:

$$\begin{aligned}c_{cy} &= c_{cy}^{+}\\ b_{cy} &= b_{cy}^{+}+b_{cy}^{-}\end{aligned} \tag{2.16}$$

Convert back from Cartesian to polar, substitute original terms and simplify:

$$\begin{aligned}\alpha_{cy} &= \sqrt{(b_{cy})^2+(c_{cy})^2}\\ &= \sqrt{(\alpha_{cy}^{+}\cos\phi_{cy}^{+}+\alpha_{cy}^{-}\cos\phi_{cy}^{-})^2+(\alpha_{cy}^{+}\sin\phi_{cy}^{+})^2}\\ \phi_{cy} &= \tan^{-1}\left(\frac{c_{cy}}{b_{cy}}\right)\end{aligned} \tag{2.17}$$

$$\begin{aligned}\alpha_{cy} &= \sqrt{(\alpha_{cy}^{-})^2+2a_{cy}^{-}\alpha_{cy}^{+}\cos\phi_{cy}^{-}\cos\phi_{cy}^{+}+(\alpha_{cy}^{+})^2}\\ \phi_{cy} &= \tan^{-1}\left(\frac{\alpha_{cy}^{+}\sin\phi_{cy}^{+}}{\alpha_{cy}^{-}\cos\phi_{cy}^{-}+\alpha_{cy}^{+}\cos\phi_{cy}^{+}}\right)\end{aligned} \tag{2.18}$$

Figure 2.4 shows the resulting CMA along with the required profile parameters for an additional cyclic amplitude of $\alpha_{cy}^{+} = 25°$. Each curve represents a different cone angle. The curves show the variation of cyclic control phase ϕ_{cy}^{+} from 0 to 180°, and the results are symmetrical in M_3. This α_{cy}^{+} yields a control moment M_{23} similar to the Precession Tactic of Chapter 2.B.2 while preserving most of the original M_1. Moreover, this tactic retains a useful in-plane CMA even edge-on to the Sun ($\gamma = \pm 90°$), so it can recover from any attitude. Note that the back sides of the blades must be allowed to be illuminated to achieve this CMA above about 30° cone angle. Therefore, it is advantageous to aluminize both sides of the blade.

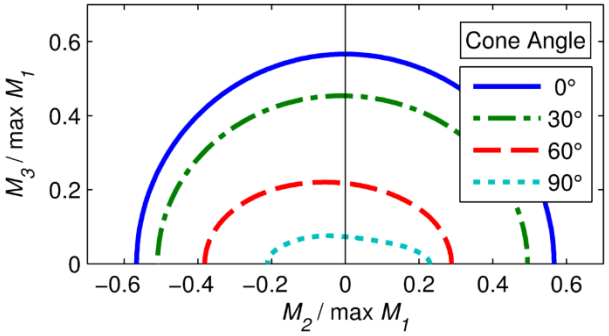

a) In-plane CMA

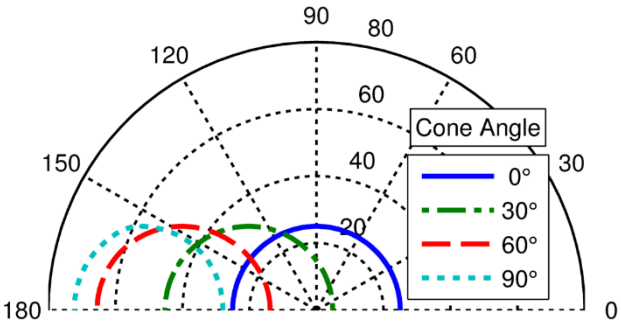

b) Cyclic profile (radius: α_{cy}, angle: ϕ_{cy})

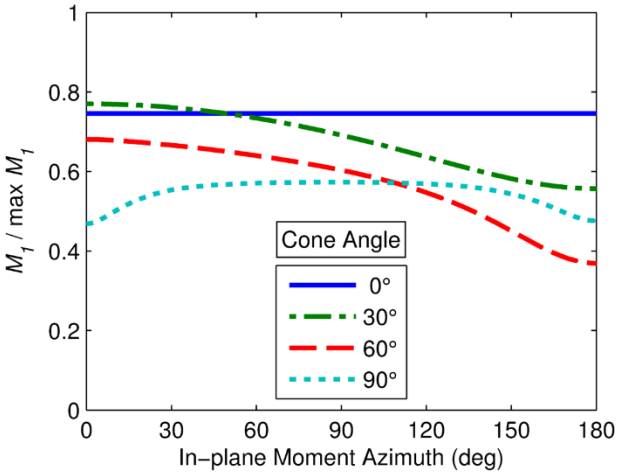

c) Spin axis CMA

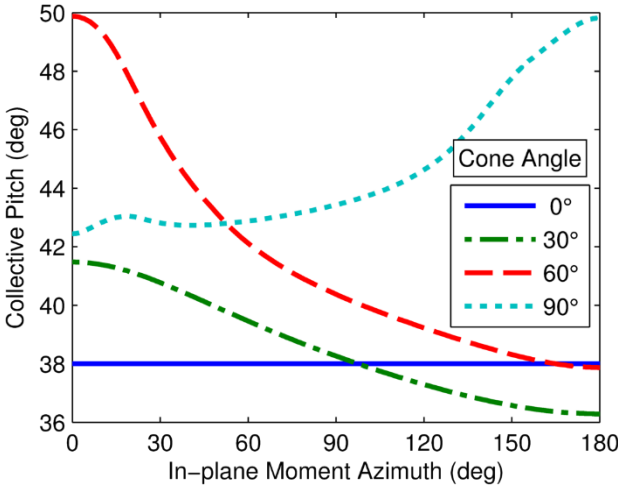

d) Collective pitch to maximize M_1

Figure 2.4: Spin Control Tactic with $\alpha_{cy}^{+} = 25°$

Notice in Figure 2.4a that there is more CMA in the $\pm M_2$ direction than along $\pm M_3$ at high cone angles. Figure 2.5 illustrates this mechanism by showing two cases of the Collective tactic at a 60° cone angle. For understanding, focus on the single blade responsible for the most in-plane

moment. This is the top blade in Figure 2.5a, which is pointed only 4° off from the Sun, so M_2 is high. In Figure 2.5b, the right blade is the largest contributor to M_3, but this blade can only ever have a minimum Sun angle equal to the cone angle (60° in Figure 2.5), regardless of blade pitch angle. Therefore, the heliogyro will always have the most in-plane CMA along $\pm M_2$, and this reasoning applies to all attitude control tactics, not just Spin Control. Fortunately, $\pm M_2$ is the component required to change cone angle and reduction of cone angle would the first step in recovering from undesirable attitudes, such as edge-on to the Sun.

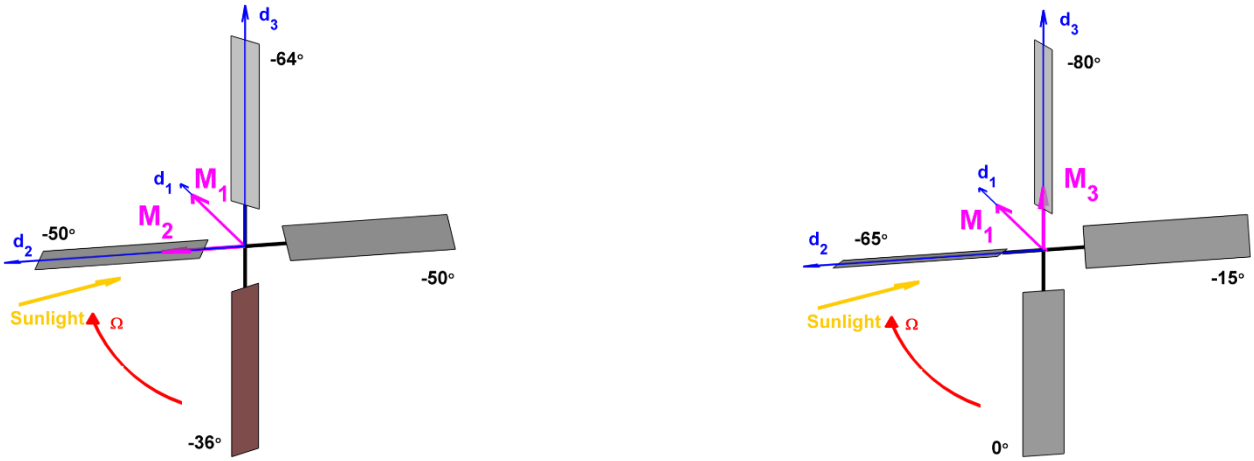

a) $\phi_{cy}^{+} = 0°$ (red indicates backside illumination) **b) $\phi_{cy}^{+} = 90°$**

Figure 2.5: Spin Control Tactic M_2 vs. M_3 CMA at α_{co} = 35°, α_{cy}^{+} = 25°, and γ = 60°

The results of Figure 2.4 are obtained by numerically computing the α_{cy}^{-} and α_{co} to maximize M_1 for a given α_{cy}^{+}; the in-plane moment is a dependent variable. For use in attitude control however, one must find the inverse of the `HGForce` mapping, i.e. the required pitch profile to achieve a desired moment (or maximize the magnitude in a desired direction when the desired magnitude is not achievable). The presence of local minima requires a reasonable seed in a gradient descent solution for this inverse. My approach is to first obtain an approximate inverse function by fitting the functional behavior with parameterized models:

$$\phi_{cy}^{+} \cong \Psi_d \tag{2.19}$$

$$\frac{\bar{M}_1}{\sin(2\alpha_{co})} \cong b_1 + b_2\alpha_{cy}^{+} + b_3 \sin 2\gamma + \gamma\left[b_4 + b_5 \cos\left(2\phi_{cy}^{+}\right) + b_6 \cos\phi_{cy}^{+}\right] \tag{2.20}$$

$$\alpha_{cy}^{-} \cong \gamma(c_1 + c_2\alpha_{co}) \qquad \phi_{cy}^{-} = 180° \tag{2.21}$$

$$\frac{\bar{M}_{23}}{\alpha_{cy}^{+}} \cong \sin(2\alpha_{co})\left[d_1 + d_2\gamma + d_3\gamma \cos\left(2\phi_{cy}^{+}\right)\right] \tag{2.22}$$

using least squares regression to determine their parameter values. I determined the form of these parameterized models by visually inspecting the forward mapping while using the regression R^2 to gage which of the tested terms were the largest contributors. Table 2.1 provides the resulting *b*, *c*, and *d* coefficient values and the regression R^2. These R^2 are all above 90%, so, these approximate solutions may suffice for first-cut mission planning. Two slices of this six-dimensional problem are visualized in Figure 2.6 by plotting the Spin Control Tactic's forward mapping from control inputs to M_1 and M_{23} with the regression fits in shaded gray. These plots illustrate how nonlinear the inverse problem is, and they emphasize the importance of a good initial estimate for an iterative search of the precise solution to the inverse problem. α_{cy}^{-}

Table 2.1: Spin Control Tactic regression (deg)

Coefficient	Eq. (2.20), α_{co}	Eq. (2.21), α_{cy}^{-}	Eq. (2.22), α_{cy}^{+}
1	1.1033	0.7012	0.0222
2	-0.0127	-0.0013	-1.76e−4
3	-0.0105		3.63e−5
4	-0.0036		
5	-0.0008		
6	0.0014		
Regression R^2	94%	99.9%	93%

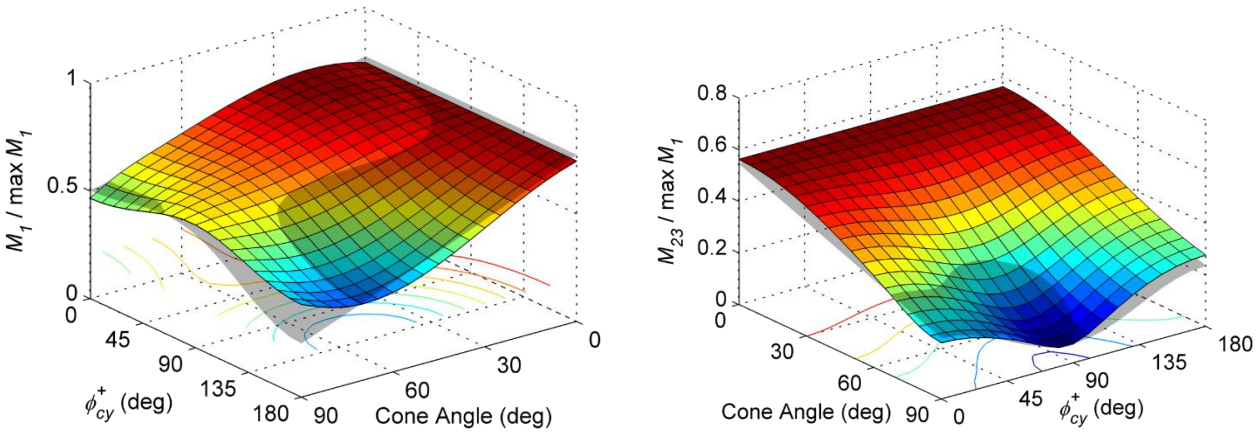

a) Spin moment magnitude **b) In-plane moment magnitude**

Figure 2.6: Spin Control Tactic and fits (shaded) vs. γ & ϕ^+_{cy} at α_{co} = 40° & α^+_{cy} = 25°

Figure 2.7 shows the Spin Control Tactic nonlinear inversion at γ = 0, the most likely application of this tactic. The three subplots correspond to the pitch profile inputs required to achieve a range of desired moments M_{2d} and M_{3d} while keeping the desired spin-up moment M_{1d} constant at 60% of the maximum. The "*d*" subscript indicates this is a desired moment, and it is therefore an objective function in the constrained optimization. The area outside of the "Max M_{23}" line is impossibly high for these conditions, but a higher M_{23} could be achieved at the expense of M_1. The cyclic profile (Figure 2.7b and c) is centered about the origin because there is no cyclic moment correction when γ = 0. At higher cone angles, both the point of zero cyclic amplitude (at the origin of Figure 2.7b) and the hub of the cyclic phase contours (at the origin of Figure 2.7c) shift up the $+M_2$ axis since this moment automatically arises when $\gamma > 0$ (see Figure 2.2).

Thus the Spin Control Tactic is fully realized with three components: a collective to provide spin control torque M_1, a cyclic moment correction for non-zero cone angles, and an additional cyclic for spin axis precession torque M_{23}. This tactic is capable of meeting both in-plane and spin moments simultaneously, but it cannot produce in-plane moments alone. Such solutions would be outside the local minimum trough explored with this attitude control tactic.

After blade deployment, large spin moments would not normally be required, though, so the next section presents a tactic that allows for primarily in-plane moments.

2. *Precession Tactic*

The half-p pitch profile is the primary method of controlling spacecraft attitude after blade deployment (e.g. modes 2, 4, 5b, and 6 of Table 1.5). It produces in-plane moments M_2 & M_3 to precess the spin axis. Figure 2.8 shows moment components for a 75° amplitude half-p profile with variation in cone angle and half-p phase. Similar to the spin moment of uncompensated collective (Figure 2.2), the in-plane moment in Figure 2.8a decreases to zero as the cone angle reaches 90° with a half-p profile alone. Furthermore, Figure 2.8b shows an unwanted spin moment M_1 that arises when $\gamma \neq 0°$ and $\Psi \neq \pm 90°$, so half-p must also be combined with a cyclic moment correction. In this case, the cyclic moment correction zeroes the unwanted M_1 instead of the unwanted M_2 in the Spin Control Tactic.

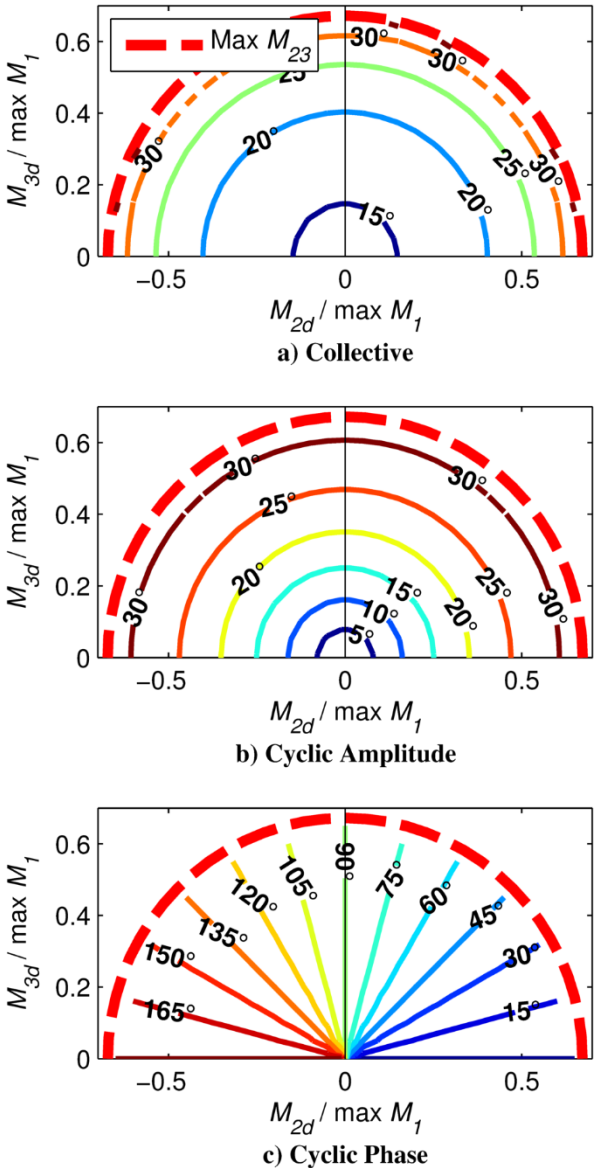

Figure 2.7: Spin Control Tactic pitch profile required to meet a desired M_2 and M_3 with $\bar{M}_1$ = 0.6 at γ = 0°

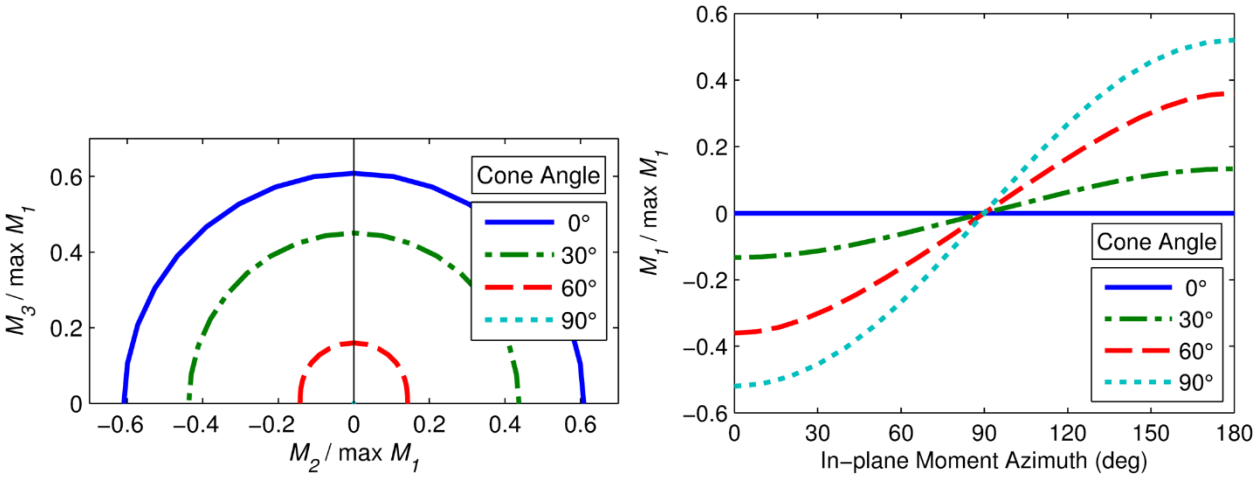

a) In-plane moment (M_{23} = 0 at γ = 90°) **b) Spin moment**

Figure 2.8: 75° Half-p profile variation with cone angle

Figure 2.9 shows the complete Precession Tactic with the combined half-p and cyclic profiles for maximum CMA, found by iterative solution of Eq. (2.12). The half-p amplitude of Figure 2.9c maximizes the in-plane moment of Figure 2.9a, and the cyclic amplitude of Figure 2.9b eliminates the unwanted M_1 (not shown). This cyclic moment correction is nearly linear with a slope of about $\gamma/2$ vs. $2\gamma/3$ for the Spin Control Tactic. The cyclic moment correction partly restores the desired in-plane moment M_{23} (compare Figures 2.9a and 2.8a), similar to the Spin Control tactic's restoration of M_1. Also like the Spin Control Tactic, it provides the CMA to recover from the worst-case orientation, γ = 90° (mode 6 of Table 1.5). This would require both sides of the blade to be illuminated, and achieving this CMA would require backside illumination at around 50° cone angle and above.

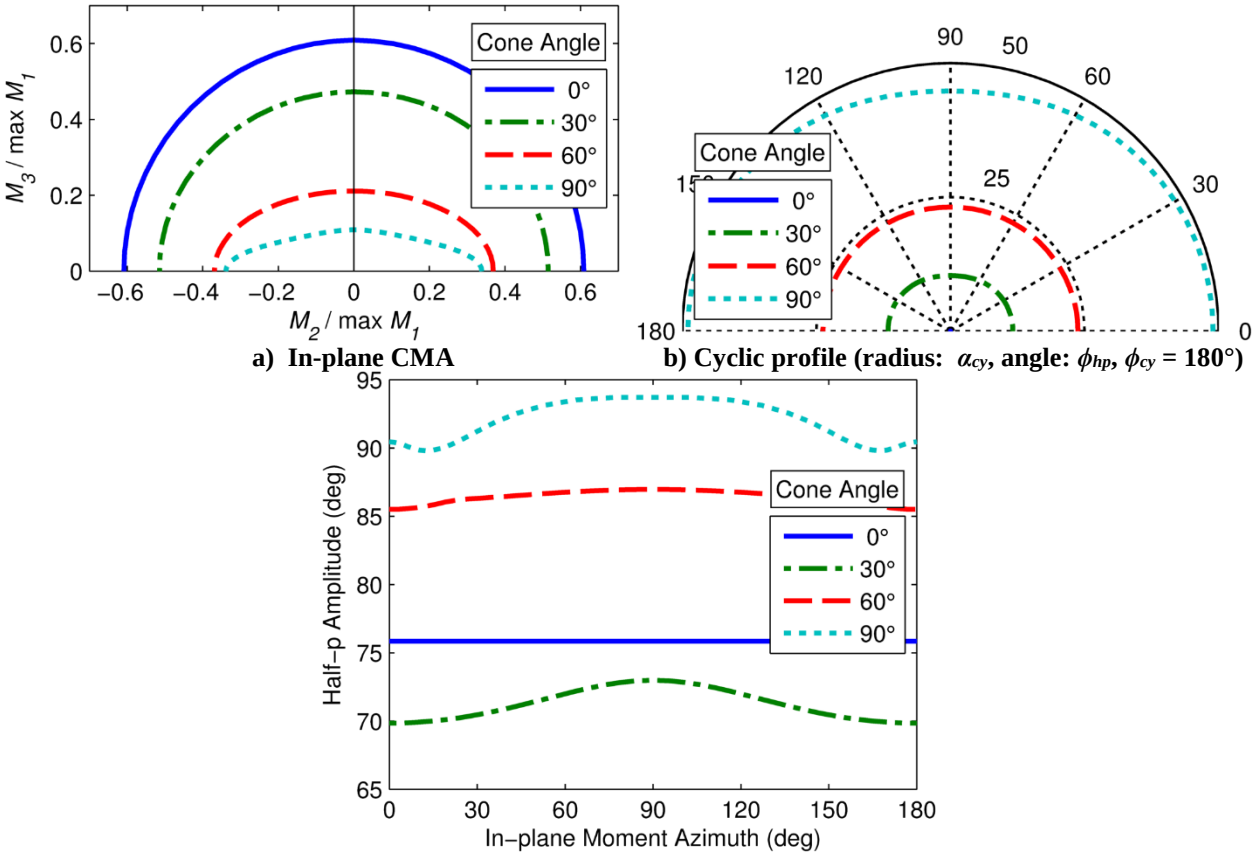

a) In-plane CMA **b) Cyclic profile (radius: α_{cy}, angle: ϕ_{hp}, ϕ_{cy} = 180°)**

c) Half-p amplitude to maximize M_{23}

Figure 2.9: Precession Tactic

One attitude disturbance torque would come from the small flapwise deflection of the blades away from the Sun due to SRP. At non-zero cone angles, this creates an M_3 that would tend to precess the spin axis in a cone about the Sun line that can be approximated with Eq. (35) of Ref. 51:

$$M_3 = \frac{1}{2} PR^2 \sin 2\gamma \sin \lambda_1 \tag{2.23}$$

Given the maximum flapwise deflection of 0.04° predicted for HELIOS from Eq. (2.3), this disturbance torque would be less than 0.002 normalized units. Therefore, this tactic should have no trouble achieving or maintaining any attitude in the presence of this solar disturbance torque.

Cyclic on top of a half-p profile can zero the unwanted spin moment, but it can also provide limited spin control authority about M_1; simply vary α_{cy} to meet the desired M_1. Unfortunately,

the Precession Tactic M_1 CMA is poor compared to the Spin Control Tactic, and the CMA drops to zero when $\Psi = \pm 90°$ (See Figure 2.8b.). Therefore, one should use the Spin Control Tactic when the primary goal is to spin-up or -down; however, the Precession Tactic could provide some limited control to maintain Ω during attitude maneuvers if Ψ is away from ±90°.

Overall, this tactic is simpler than Spin Control; it does not superimpose two cyclic profiles, and the desired spin moment is generally zero. This makes inversion easier with fewer parameters to fit. Furthermore, an $M_{1d} = 0$ can always be met, so it becomes a constraint instead of an objective function. The initial pitch profile estimate comes from the approximate inverse models:

$$\phi_{hp} \cong \Psi_d \tag{2.24}$$

$$\frac{\bar{M}_{23}}{\alpha_{hp}} \cong b_1 + b_2\gamma + b_3\gamma\cos\left(2\phi_{hp}\right) \tag{2.25}$$

$$\alpha_{cy} \cong \gamma\left(c_1 + c_2\alpha_{hp}\right) \qquad \phi_{cy}^{-} = 180° \tag{2.26}$$

with linear regression coefficients b and c and regression R^2 given in Table 2.2. Again, all regressions have an R^2 above 90%, so these models provide reasonable initial values for iteration. Figure 2.10 plots two slices of the Precession Tactic's forward mapping with the fits of Eq. (2.25) in shaded gray. In Figure 2.10b, the mapping becomes very flat above about 70° half-p amplitude, indicating that the solution is not very sensitive to this parameter near the maximum M_{23}. Limiting this tactic to half-p amplitudes <70° would simplify it and keep $\boldsymbol{F}$ higher without significant CMA penalty.

Table 2.2: Precession Tactic regression (deg)

Coefficient	Eq. (2.25) α_{hp}	Eq. (2.26) α_{cy}
1	0.00838	0.7016
2	-6.85e−5	-0.0028
3	1.66e−5	
Regression R^2	93%	97%

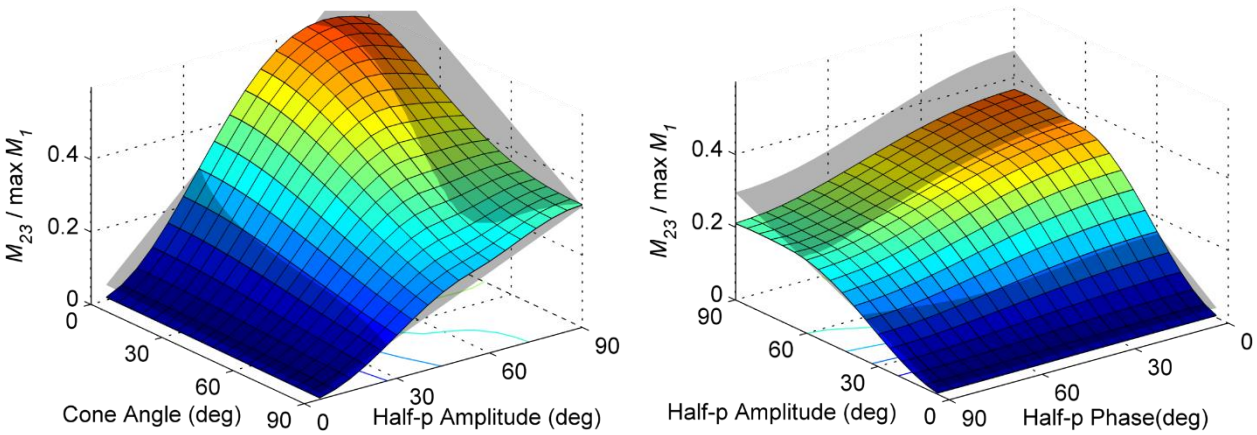

a) Variation with γ and α_{hp} at ϕ_{hp} = 0° **b) Variation with α_{hp} and ϕ_{hp} at γ = 60°**

Figure 2.10: Precession Tactic in-plane moment magnitude and fits (shaded)

Figure 2.11 gives the Precession Tactic inverse solution at a 35° cone angle, a likely application of this tactic (modes 4 & 5 in Table 1.5). The cyclic amplitude of Figure 2.11a does not vary much with the desired M_{23}. Also, the half-p phase in Figure 2.11c does not match up exactly with the desired in-plane moment azimuth Ψ because the cone angle is non-zero. For example, the slope of the 45° phase line is less than one, when it would equal one at γ = 0°.

The primary reason to change a solar sail's attitude is to change the direction of solar thrust. Reorienting the entire sail surface by spin axis precession does provide the largest change in solar thrust, but attitude maneuvers can take hours for a heliogyro (see Chapter 2.C). Furthermore, a large fraction of the solar thrust is diverted to creating the precession torque while maneuvering. The next section discusses an alternate method of vectoring the solar thrust with a cyclic profile, a process that can occur in a matter of minutes instead of hours (see Chapter 4).

3. *Lateral Thrust Tactic*

The third and final tactic combines collective and cyclic profiles, similar to the Spin Control Tactic but with a different goal. As shown in Figure 1.3c, the cyclic profile can generate lateral thrust without precessing the spin axis, useful when a relatively rapid change in thrust direction is required such as an Earth escape spiral (mode 3 of Table 1.5). The heliogyro would normally be Sun-facing in this case so thrust could be quickly changed to any direction (see Chapter 3), but maintaining this attitude against disturbance torques would still require CMA in all directions.

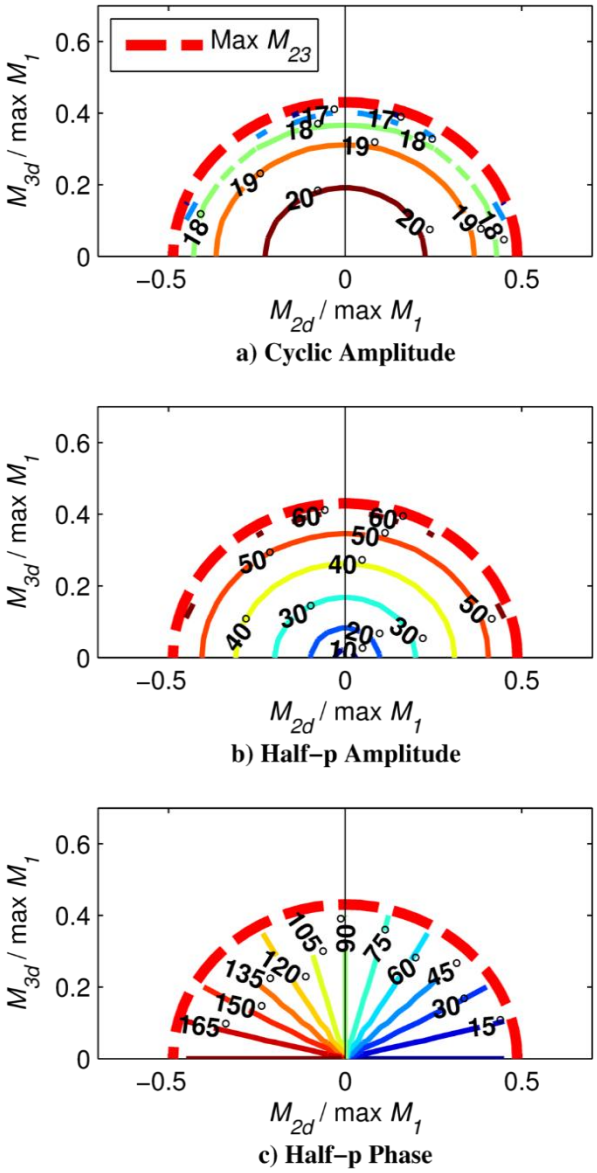

Figure 2.11: Precession Tactic required pitch profile to meet a desired M_2 and M_3 with $M_1 = 0$ at $\gamma = 35°$

The Lateral Thrust Tactic starts with the same approach as the Spin Control Tactic: a collective (α_{co}), a cyclic moment correction (α_{cy}^{-}), and an additional cyclic profile (α_{cy}^{+}, ϕ_{cy}^{+}). This tactic, however, crosses into a different local minimum trough where the cyclic amplitude is large enough to completely eliminate M_1. With this tactic, cyclic amplitude sets M_1, while the collective primarily determines M_{23} (opposite the Spin Control Tactic). In both cases, the additional cyclic phase ϕ_{cy}^{+} sets the in-plane moment azimuth Ψ. Lastly, it would generally be desired to maximize the lateral thrust in a direction set by the clock angle δ and independent of Ψ. Unfortunately, the

direction of the lateral thrust created by this tactic is inextricably bound to Ψ via ϕ_{cy}^{+}. The sign of α_{co}, however, determines whether the in-plane force and moment are in the same direction or opposite each other. Therefore, when $M_{2d} < 0$, the collective sign is flipped and ϕ_{cy}^{+} rotated 180° thereby maximizing $+F_l$.

The Lateral Thrust Tactic CMA is given in Figure 2.12 with plots of the resulting profile inputs. Notice that the authority in the M_3 direction drops off dramatically between 30° and 60° cone angles. The 75° cone angle curve replaces the 90° curve, since this tactic does not have full CMA at high cone angles. Fortunately, it would not be needed at high cone angles, as the Precession Tactic could operate in this regime. Figure 2.12b illustrates the 180° flip in ϕ_{cy}^{+} to keep thrusting in the $+F_l$ direction also evident in the collective sign change of Figure 2.12c. This tactic generally has the highest blade pitches, so nonlinear effects play the greatest role. This makes solution convergence difficult, curtails the $\pm M_3$ CMA at high cone angles, and leads to the waviness in Figure 2.12c. The solution is not particularly sensitive to collective, though,

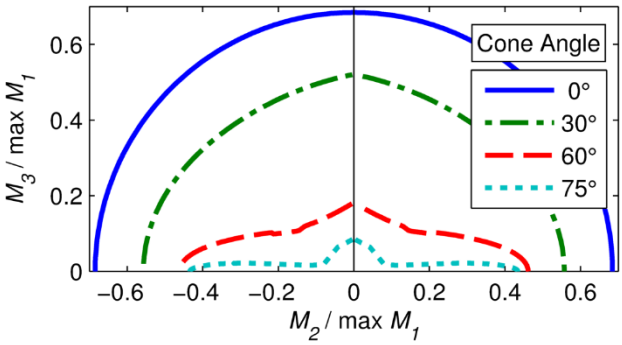

a) In-plane CMA

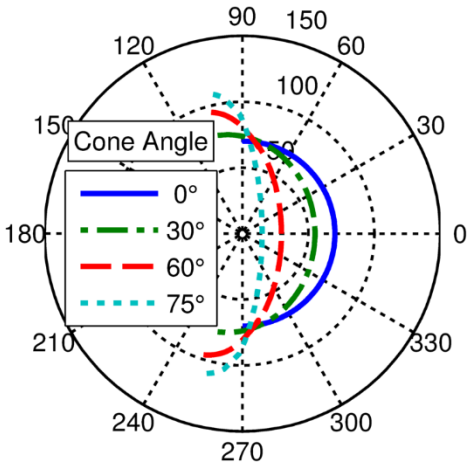

b) Polar plot of cyclic profile (α_{cy}, ϕ_{cy})

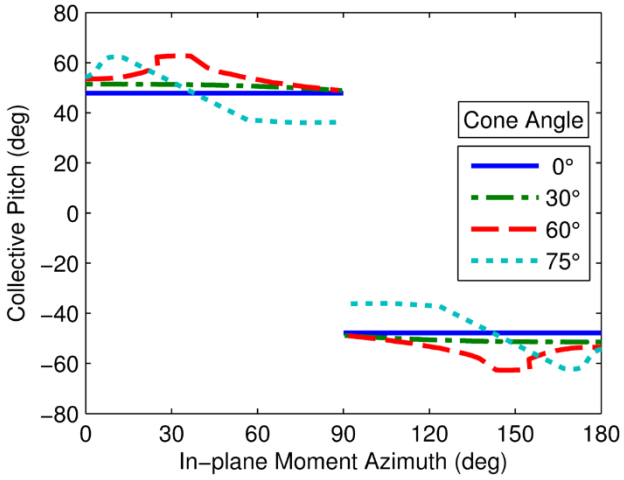

c) Collective pitch

Figure 2.12: Lateral Thrust Tactic

so the problem could be simplified by limiting the collective to 50° or less for near-maximum in-plane CMA. Furthermore, these large blade pitch angles mean that backside illumination of the blades occurs at all cone angles when maximizing the CMA.

As with the other two tactics, the inversion process for the Lateral Thrust Tactic begins with the initial estimate from a linear regression fit of the forward mapping. For this tactic, I found the forward mapping to have the approximate form:

$$\phi_{cy}^{+} \cong \Psi_d \tag{2.27}$$

$$\frac{\bar{M}_{23}}{\sin 2\alpha_{co}} \cong b_1 + b_2\gamma + b_3\gamma \cos 2\phi_{cy}^{+} \tag{2.28}$$

$$\alpha_{cy}^{-} \cong \gamma(c_1 + c_2\alpha_{co}) \qquad \phi_{cy}^{-} = 180° \tag{2.29}$$

$$\begin{aligned}\alpha_{cy}^{+} \cong d_1 + d_2\alpha_{co} + \cos\phi_{cy}^{+} \sin\gamma\,(d_3 + d_4\alpha_{co}) \\ + \cos 2\phi_{cy}^{+}\,(d_5 \sin\gamma + d_6 \sin 2\gamma)\end{aligned} \tag{2.30}$$

with fit coefficients *b*, *c*, and *d* and regression R^2 given in Table 2.3, and Figure 2.13 gives two slices of this mapping. The regression is restricted to cases where $\alpha_{cy} < 90°$ to increase coefficient accuracy in the areas most useful for this tactic. This omits area where nonlinear effects push the solution to very high cyclic amplitudes such as Ψ near ±90° and the cone angles above 65°, such as in Figure 2.13a. Even so, the large amplitudes of this tactic make linear regression of α_{cy}^{+} difficult; the R^2 of Eq. (2.30) is only 85% even with six terms, and adding further terms yields little improvement. Figure 2.13b illustrates the lack of $\pm M_3$ CMA at high cone angles, evidenced by the dramatic drop off in M_{23} when ϕ_{cy}^{+} (related to Ψ) is near 90°.

The resulting inversion is shown in Figure 2.14 for 0° cone angle, as this is the most likely attitude for implementation of this tactic. As designed, the M_{23} depends mostly on collective (Figure 2.14b) and very little on cyclic amplitude (Figure 2.14a), opposite the case in the Spin Control Tactic. Figure 2.14b & c illustrate the flip in sign at $M_2 = 0$ previously described.

Table 2.3: Lateral Thrust Tactic regression (deg)

Coefficient	Eq. (2.28) α_{co}	Eq. (2.29) α_{cy}^{-}	Eq. (2.30) α_{cy}^{+}
1	0.6895	0.701049	57.3130
2	-0.0063	-0.001091	0.2403
3	0.0019		55.4580
4			-0.7359
5			-44.6979
6			19.1768
Regression R^2	95%	99.9%	85%

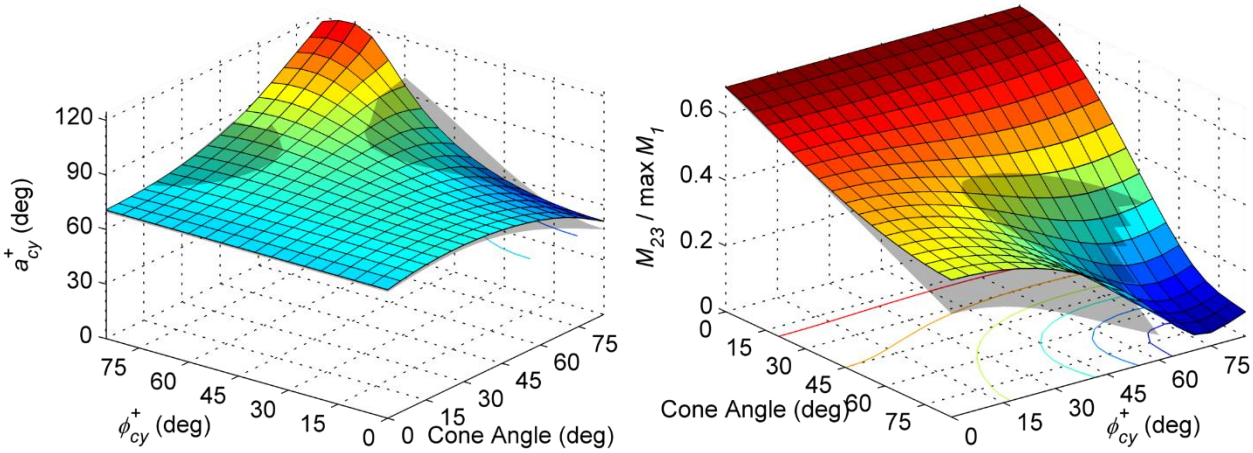

a) Additional cyclic amplitude **b) In-plane moment magnitude**

Figure 2.13: Lateral Thrust Tactic and fits (shaded) vs. γ and ϕ_{cy}^{+} at α_{co} = 50°

C. Tactic Comparison

The operational modes listed in Table 1.5 cover many practical solar sail mission scenarios. Each mode can be optimally served with one of the attitude control tactics developed in Chapter 2.B. Which tactic is optimal often depends on a tradeoff between the tactics' precession and lateral thrust capabilities. Since large spin moments would not generally be needed after blade deployment, the principal comparison is between the Precession and Lateral Thrust Tactics.

1. *Lateral Thrust Capability*

Per the frame definitions, a positive cone angle produces positive, attitude-based lateral thrust (e.g. $+F_l$ for $\delta = 0°$), and a cyclic profile can also produce lateral thrust. Figure 2.15 shows the heliogyro's maximum lateral thrust capability versus cone angles. The "Attitude-dependent" line is equivalent to the capabilities of a flat sail, so only negative lateral thrust is possible at negative cone angles. The "Net" line highlights the heliogyro's unique lateral thrusting capability, as it can produce a positive lateral thrust at all cone angles. The "Cyclic-dependent" line is difference between the other two. This line touches zero at 35° cone angle because no pitch profile can improve upon a flat sail at this angle. Otherwise, the cyclic profile is able to improve upon a flat sail's lateral thrust by pitching the individual blades closer to the optimal 35°. The "cyclic amplitude" corresponds to the right axis and is the amplitude that maximizes $+F_l$. The resulting optimal cyclic amplitude is found to be an affine function of cone angle: a straight line with a slope of −1.15°/degree and intercept of 41°. Figure 2.15 represents the heliogyro's lateral thrusting capability when it is not producing any attitude control moments, but such moments would be required during real operations.

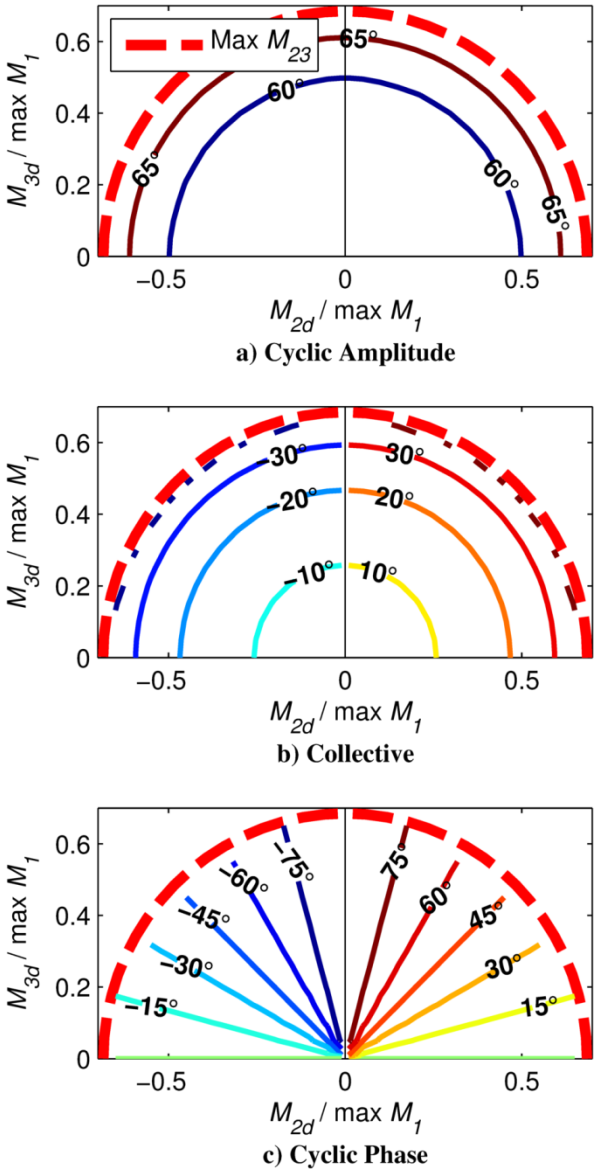

Figure 2.14: Lateral Thrust Tactic required pitch profile to meet a desired M_2 and M_3 with $M_1 = 0$ at $\gamma = 0°$

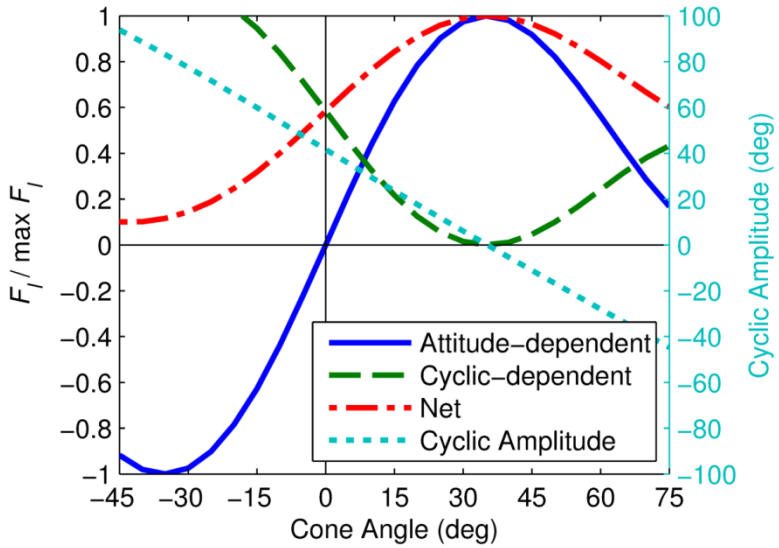

Figure 2.15: Maximum lateral thrust when no moment is desired and δ = 0°

Figure 2.16 compares these two tactics for a range of M_{2d} and cone angles, given M_{1d} = M_{3d} = 0. A positive M_2 increases γ and vice versa, so this is the most useful moment when a change in cone angle is primarily desired, such as operational modes 5b (70° slew maneuver) and 6 (recovery from high cone angles). To aid comparison, red shading indicates where each tactic has the lower lateral thrust. The Precession Tactic only produces attitude-dependent lateral thrust, so it cannot produce positive lateral thrust when $\gamma \leq 0°$. The Lateral Thrust Tactic uses the cyclic profile to increase lateral thrusting at low and negative cone angles. Therefore, when only small moments are required to maintain attitude, use the Lateral Thrust Tactic for cone angles less than about 20° and the Precession Tactic for higher cone angles. The next section covers cases requiring large moments for rapid slewing of the cone angle.

One final note is that both attitude control tactics reduce the lateral thrust from the maximum possible shown in Figure 2.15. This is because lateral thrust is not an objective function in the attitude control tactics' optimization. Figure 2.15 optimizes the cyclic profile to maximize lateral thrust when no moment is desired, whereas the attitude control tactics optimize the combined pitch profile to meet the desired moment without regard for lateral thrust. Any time one

desires an attitude control moment at non-zero cone angles, the cyclic moment correction must be applied to achieve the desired moment direction. This correction is almost entirely dependent on the cone angle and not the desired moment, so even very small desired moments can require large cyclic amplitudes at high cone angles. Therefore, it would be advantageous to have a generous attitude control dead band when the primary goal is to maximize thrust (as opposed to meeting the desired attitude control moment). For example, during mode 4 or 5a of Table 1.5, use a cyclic profile to maximize lateral thrust while allowing the cone angle to drift ±15°, then apply the Precession Tactic to restore the 35° cone angle. This is one case where a piecemeal approach would be advantageous rather than constantly applying the Precession tactic with its attendant cyclic moment correction.

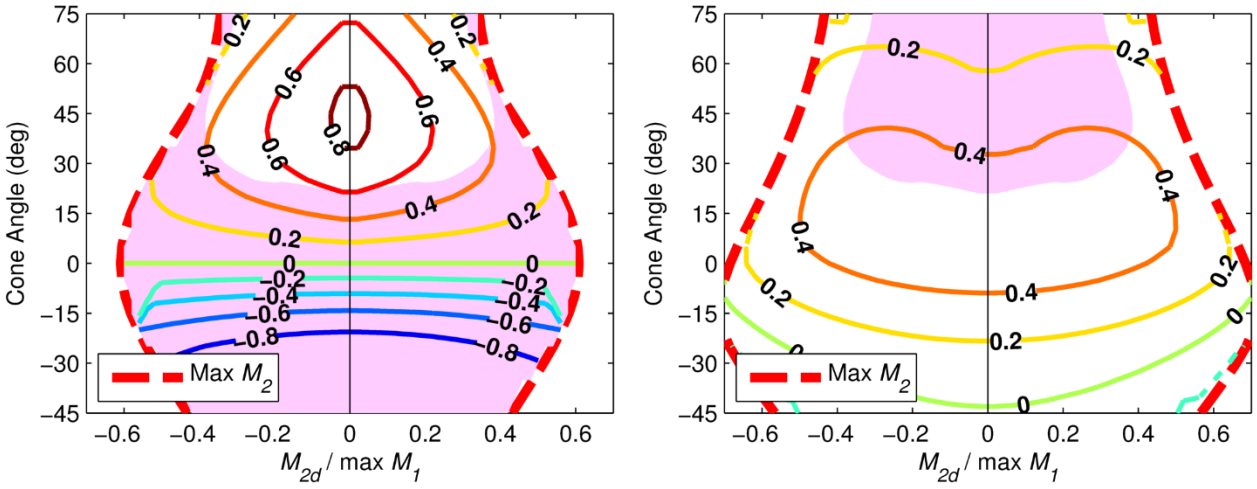

a) Precession Tactic **b) Lateral Thrust Tactic**

Figure 2.16: F_1 vs. M_{2d} and γ at M_{1d} = M_{3d} = 0 with the sub-optimal regions shaded in red

Attitude disturbance torques would not be confined to the M_2 direction depicted in Figure 2.16. Figure 2.17 compares the two tactics' lateral thrust at a 35° cone angle for all feasible in-plane moments. The Precession Tactic yields a higher lateral thrust for all desired moments except when $|M_{3d}|$ is low and $|M_{2d}|$ is high, like the conditions in Figure 2.16. This is due to two effects. First, cyclic does double duty in the Lateral Thrust Tactic—as the moment correction α_{cy}^{-} and the α_{cy}^{+} to eliminate M_1—neither of which is to maximize lateral thrust. Therefore, this tactic

requires high cyclic amplitudes even at low required moments, reducing available thrust. Furthermore, Figure 2.17a shows that the lateral thrust generated by the Precession Tactic is completely decoupled from the in-plane moment azimuth Ψ. With the Lateral Thrust Tactic, however, the ϕ_{cy} sets Ψ and the cyclic-dependent lateral thrust direction. Therefore, the Precession Tactic will keep more lateral thrust intact when the desired thrust and moment directions are not aligned (in this case, when the desired M_3 is large relative to the desired M_2).

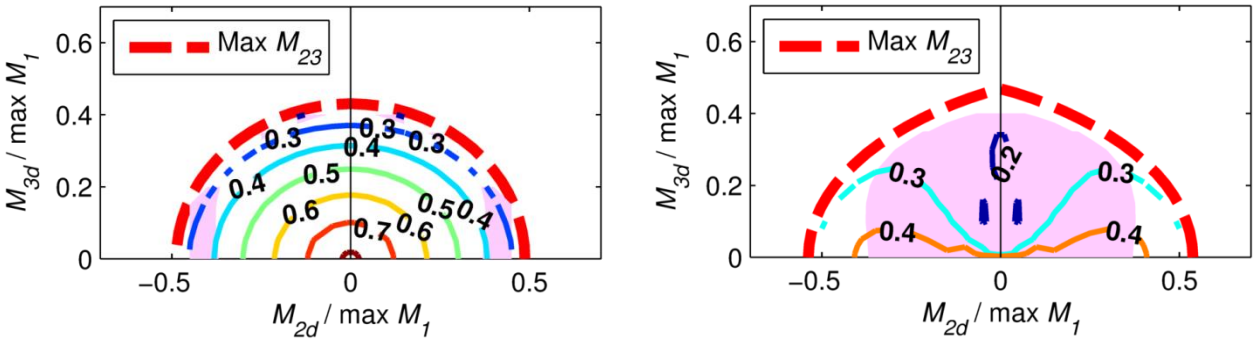

a) Precession Tactic **b) Lateral Thrust Tactic**

Figure 2.17: F_1 vs. M_{2d} and M_{3d} at γ = 35° with sub-optimal regions shaded in red

2. Estimated Slew Times

One way to compare spin axis precession rates is by estimating the time for a slew maneuver to change the cone angle. First, approximate HELIOS' mass moment of inertia as six flat plates, a ring, and a cylinder:[70]

$$I_s = m_s \,\mathrm{diag}\left[\frac{c^2}{24}+\frac{R^2}{6}, \frac{c^2}{24}+\frac{R^2}{6}, \frac{c^2+R^2}{12}+\left(\frac{R}{2}+r_{hex}\right)^2\right] \tag{2.31}$$

$$= \mathrm{diag}[40{,}333;\ 40{,}333;\ 81{,}667]\ \ kg\cdot m^2$$

$$I_{truss} = m_{truss} r_{hex}^2\,\mathrm{diag}[1,1,2] \tag{2.32}$$

$$r_{hex} = \frac{c}{2}\left(1+\sqrt{2}\right)$$

$$I_{bus} = m_{bus}\,\mathrm{diag}\left[\frac{r_{bus}^2}{4}+\frac{h_{bus}^2}{12}, \frac{r_{bus}^2}{4}+\frac{h_{bus}^2}{12}, \frac{r_{bus}^2}{2}\right] \tag{2.33}$$

$$r_{bus} = 0.3\ m, \qquad h_{bus} = 0.9\ m$$

$$I_{tot} = I_s + I_{truss} + I_{bus} = \text{diag}[40{,}337;\ 40{,}337;\ 81{,}674]\ \ kg \cdot m^2 \tag{2.34}$$

where the `diag` function is a diagonal matrix representing the principal moments of inertia about the heliogyro center of mass, assumed coincident with the plane of rotation and spin axis. Comparing equations (2.31) & (2.34), the sail blades comprise 99.99% of the total mass moment of inertia due to their extreme length. For comparison, a square sail of the same area and mass would have principal moments of inertia of about [1098, 1098, 2195] kg·m^2, or 2.7% that of the heliogyro. Considering that HELIOS' 1 RPM spin rate gives it an angular momentum of 8553 Nms, slewing the heliogyro is considerably more difficult than for a square sail. Fortunately, the lateral thrusting capability partially obviates the need for rapid slewing.

The instantaneous maximum precession rate about $\hat{\boldsymbol{d}}_3$ (for a change in γ) is given by:

$$\omega_{3max}(\gamma) = \frac{M_{2max}(\gamma)}{\Omega I_{3tot}} \tag{2.35}$$

The $M_{2max}(\gamma)$ line is plotted for both tactics in Figure 2.16. The Precession Tactic's maximum moment with HELIOS' parameters at 1 AU is 0.23 Nm at γ = 0 and 0.13 Nm at γ = 90°, giving HELIOS a maximum slew rate of 5.6°/hr at γ = 0 and 3.1°/hr at γ = 90°. Break down the terms of Eq. (2.35) to get a rough idea of what could possibly improve this extremely slow slew rate. From Eq. (2.12), the maximum moment is proportional to:

$$M_{2max} \propto RA_sP \tag{2.36}$$

and the largest contributor to moment of inertia about the spin axis is:

$$I_{3tot} \cong \frac{m_s R^2}{3}$$
$$81{,}674\ kg \cdot m^2 \cong 80{,}667\ kg \cdot m^2 \tag{2.37}$$

Therefore, the factors most affecting maximum slew rate are:

$$\omega_{3max} \propto \frac{AP}{\Omega m_s R} \tag{2.38}$$

so the slew rate could be increased by:

a) increasing the ratio of sail area to blade radius, e.g. more blades or wider blades,

b) moving closer to the Sun,

c) lowering the spin rate, or

d) lowering sail loading (m_s/A_s), e.g. thinner membrane or fewer battens and other features, especially towards the blade tip.

Other considerations prevent changes to the number of blades, blade chord, and membrane thickness for HELIOS. The only pertinent variable is spin rate, currently 1 RPM for solarelastic stability reasons,[26,27,74] but this is an ongoing area of research and subject to change.

Numerical integration of the slew rate $\omega_{3max}(\gamma)$ is required to find the minimum slew times.

$$\gamma(t_f) = \gamma(t_0) + \int_{t_0}^{t_f} \omega_{3max}(\gamma) dt \tag{2.39}$$

Figure 2.18 shows the results of this integration from an initial cone angle of zero. Since there is negligible angular acceleration with the heliogyro's spinning architecture, the time to slew between two cone angles can merely be subtracted and the time to slew ± a given cone angle would be doubled. For example, it would take about 13.3 hr to slew from +35° to –35° and 45 hr to slew from +90° to –90° with the Precession Tactic.

The Lateral Thrust Tactic has slightly more M_2 CMA at all cone angles, and therefore shorter slew times in Figure 2.18; however, these results use the flat blade assumption. The nonlinear blade dynamics investigation of Chapter 4.E reveals that this assumption loses validity at the high amplitudes required for maximum M_2. These nonlinear effects reduce the CMA for the Lateral Thrust tactic, while increasing the CMA for the Precession Tactic. Combining that with

the Lateral Thrust Tactic's difficulty generating M_3 at high cone angles makes the Precession Tactic the recommended tactic for large slews and all operations above ~60° cone angle.

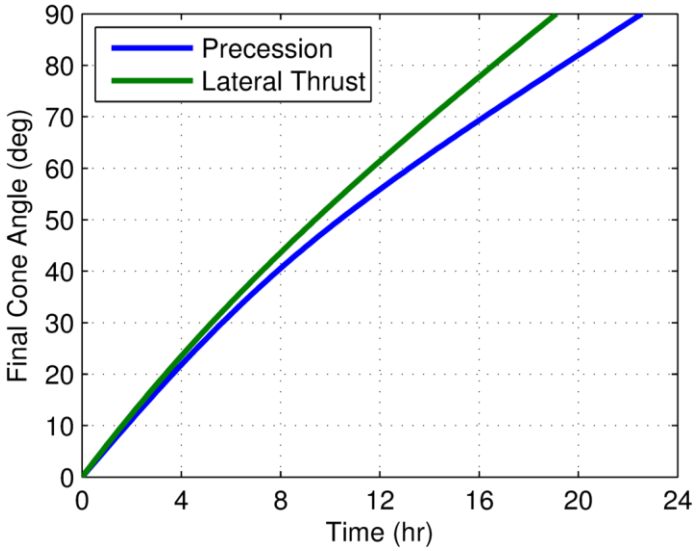

Figure 2.18: Slew angle vs. time for HELIOS

D. Chapter Summary and Recommendations

Table 2.4 summarizes the three attitude control tactics and makes recommendations about their application. Since each of the three tactics can perform all three functions (spin control, precession, and lateral thrust) to some degree, onboard logic might select the one meeting the desired moment vector while maximizing force in a desired direction. Together, these three tactics give the heliogyro full mission capability. Their solutions are an optimal moment vector under the imposed tactic constraints, but they could seed an optimization of all five pitch profile objective variables for all six force and moment component objective functions.

The practicalities of actuating heliogyro blades to achieve desired attitude control moments have not been studied at any length until now. Use of the canonical collective, cyclic, half-p blade pitch profiles one at a time introduces unwanted effects when the heliogyro is not pointed directly at the Sun, complicating attitude control. Combining pitch profiles is simpler and safer than successive application of single pitch profiles at removing these unwanted effects. Furthermore,

three-axis attitude control is always required to counter disturbance torques while simultaneously following a desired trajectory. The three attitude control tactics developed herein optimize the pitch profile to meet concurrent goals and should serve for all typical heliogyro operations. Using these tactics, the heliogyro can produce an attitude control moment in any direction at any attitude, making it a very capable and robust solar sail concept.

Table 2.4: Summary of attitude control tactics

Tactic	**Spin Control**	**Precession**	**Lateral Thrust**
Pri. profile	Collective	Half-P	Cyclic
Sec. profile	Cyclic	Cyclic	Collective
Parameters in 1st column primarily controlled by… (below)			
Ψ	ϕ_{cy}	ϕ_{hp}	ϕ_{cy}
M_{23}	α_{cy}	α_{hp}	α_{co}
M_1	α_{co}	α_{cy}	α_{cy}
$\bar{\alpha_{cy}} \cong$	$-2\gamma/3$	$-\gamma/2$	$-2\gamma/3$
Pros	Best M_1 CMA Good M_{23} CMA at all γ	Best lateral thrust for attitude maintenance when $\gamma > 20°$ Best M_3 CMA at all γ	Good M_1 CMA Best lateral thrust when $\gamma < 20°$
Cons	Lower M_{23} CMA No M_{23} without M_1	Worst M_1 CMA Poor lateral thrust at $\gamma < 20°$	Worst M_3 CMA at $\gamma > 60°$ Moment and thrust directions coupled
Suggested uses	For large changes in spin rate/angular momentum	Large slews Maintaining attitude with $\gamma > 20°$ when lateral thrusting Maintaining attitude at all γ when not lateral thrusting All operations with $\gamma > 60°$	Maintaining attitude with $\gamma < 20°$ when lateral thrusting

This chapter also mapped the achievable moment and thrust versus Sun angle, providing clear insights for mission planners. In particular, trajectory designers should account for the reduction in thrust that attitude maneuvers will require in their force models. Furthermore, the heliogyro's unique lateral thrusting capability allows for rapid changes in thrust direction without precessing its large angular momentum vector. This would be especially useful for planetary orbits or small trajectory corrections where slewing the entire spacecraft is impractical.

CHAPTER 3. EARTH ESCAPE STRATEGIES

Maneuvering in Earth orbit is one of the most difficult applications of solar sail technology, but most near-term missions are low-cost demonstrators that will be launched as secondary payloads in Earth orbit. Heliocentric orbits have such long periods that attitude maneuvers are generally inconsequential to the trajectory dynamics. For example, SPO uses modes 4 & 5 of Table 1.5, and even the 14 hours for the heliogyro to perform the ±35° slew (see Chapter 2.C.2) of mode 5b would be insignificant. This chapter examines how the heliogyro might best accomplish Earth escape and compares its performance to flat sails.

A. Canonical Planetary Escape Strategies

Planetary escape strategies can be grouped as shown in Table 3.1 based on two parameters: the method of changing the thrust direction and the Sun's position relative to the orbit plane. McInnes assumes a flat sail and pitches the entire sail to change the thrust direction.[56] MacNeal uses a cyclic pitch profile to generate thrust perpendicular to the Sun line without slewing, so his trajectories are specific to the heliogyro.[51] Both McInnes and MacNeal use two different orbit families: the first with the Sun-orthogonal to the orbit plane (***s***⊥), and the second with the Sun coplanar with the orbit plane (***s***||). Both also assume circular orbits.

Table 3.1: Planetary escape strategies

Orbit plane / **Thrust vectoring**	**Sun orthogonal (*s*⊥)** e.g. dawn-dusk Sun-synchronous	**Sun coplanar (*s*||)** e.g. geostationary
via spacecraft slewing (MI)[56]	Precess the spacecraft spin axis around a 35° cone once per orbit.	180° slew per orbit 90° sail cone angle for part of each orbit.
via cyclic pitch profile (MN)[51]	One continuous cyclic profile	Four blade pitch profiles per orbit: 0° collective, 42° cyclic, 90° collective (feathered), -42° cyclic

Recall that solar sails generally generate attitude control torques by shifting the CP-CM offset. Shifting the CM does not affect the net solar thrust because the reflective surface is unaffected. Shifting the CP reduces the available solar thrust since it diverts some photons for torque generation. Heliogyros shift the CP with pitch profiles. McInnes assumes that his sails achieve the desired attitudes without affecting thrust, which implies attitude control by some means other than CP shift, such as CM shift. However, his strategies sometimes call for sail cone angles γ of 90°. A solar sail with attitude control by CM shift alone cannot recover from such a condition, as the sail area exposed to sunlight drops to zero. Indeed, solar sail designers often compensate by setting a cone angle limit of 60° to 70°. On the other hand, kite sails (a subset of flat sails) are three-axis stabilized, so they could set the angular velocity when Sun-facing and coast through the edge-on orientation. In practice, these sails would likely need additional, non-SRP, attitude actuators (e.g. reaction wheels), making this strategy somewhat idealized. To allow for a more realistic comparison, one must account for the Precession Tactic required for a heliogyro to follow McInnes' optimal strategies.

1. Sun-orthogonal trajectories ($\boldsymbol{s}\perp$)

The first family of trajectories under consideration have the Sun orthogonal to the orbit plane, for example, a dawn-dusk Sun-synchronous orbit (SSO). The problem is that SSOs do not exist above low Earth orbit (LEO). Consequently, ride-shares to Sun orthogonal trajectories would start deep in the gravity well at altitudes with non-negligible atmospheric drag. Furthermore, the Sun would not stay orthogonal to the orbit plane throughout an escape lasting many months; the Earth's oblateness could only help maintain the geometry for a small fraction of the whole escape.

McInnes' Sun-orthogonal strategy (MI $\boldsymbol{s}\perp$) slews the sail normal (the spin axis for heliogyros) along a 35° cone relative to the Sun every orbit. Note that the half-angle of the

precession cone and the Sun cone angle have the same value. For the ideal sail, this maximizes thrust along the velocity vector at all points for maximum increase in orbit energy. The heliogyro would have to precess the spin axis with a continuous M_3 moment generated by the Precession Tactic. One can estimate the M_3 required without a full dynamics simulation by assuming the rigid body slewing from Eq. (2.35) and a circular orbit. In this case, however, only a fraction (sin γ) of the total angular momentum must be slewed, and the slew is at the mean motion rate n:

$$M_3 = -\omega_{\mathbf{s}\perp}\Omega I_3 \sin\gamma \tag{3.1}$$

$$\omega_{\mathbf{s}\perp} = n = \sqrt{\frac{\mu}{r^3}} \tag{3.2}$$

where μ is the Earth's gravitational parameter and r is the circular orbit radius. Figure 3.1a illustrates the heliogyro orientation in this strategy with the required Precession Tactic in a circular SSO. The precession moment (magenta arrow) is perpendicular to orbit velocity $\boldsymbol{v}$. The required precession moment is large in LEO and drastically reduces the thrust available for orbit-raising.

MacNeal's Sun-orthogonal strategy (MN $\boldsymbol{s}\perp$) uses a cyclic blade pitch profile to generate thrust perpendicular to the Sun and along the velocity vector, as shown in Figure 3.1b with the green force arrows for a 42° cyclic to maximize lateral thrust. The spin axis always points at the Sun, so the slew requirement is only ~1°/day, which I neglect. On the other hand, the maximum lateral thrust a cyclic pitch profile can generate is only 58% that of pitching a flat sail, as was shown in Figure 2.15. This implies less thrust along the velocity vector and therefore less orbit-raising capability. I will show later which has the larger thrust penalty: precessing the spin axis with the Precession Tactic or using a cyclic profile for lateral thrust.

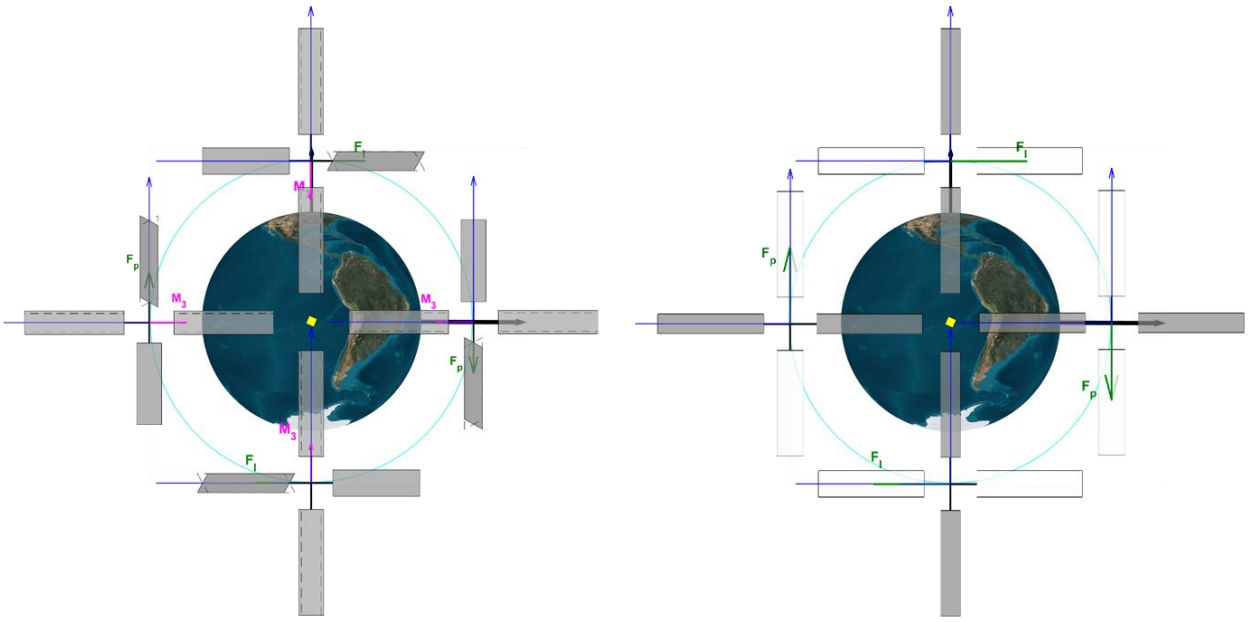

a) McInnes' precessing (MI $s\perp$) **b) MacNeal's non-precessing (MN $s\perp$)**

Figure 3.1: Illustration of Sun-orthogonal ($s\perp$) escape strategies with zoomed heliogyro views

Both McInnes' and MacNeal's Sun-orthogonal strategies are symmetrical around an orbit, so eccentricity stays relatively constant. When starting from LEO, it is important to limit eccentricity and keep the periapse as far from the atmosphere as possible to limit drag. At higher orbits, a large eccentricity may be advantageous for escape when third body effects are included.

*2. Sun-coplanar trajectories (**s**||)*

The second family of trajectories have the Sun coplanar with the orbit plane. An example trajectory would be a geostationary orbit (GEO). The Sun is only perfectly coplanar at the equinoxes, but it stays within ±23° throughout the year. Therefore, the Sun-orbit geometry should be relatively similar throughout escape, regardless of launch epoch, unlike the Sun-orthogonal family. Moreover, with frequent launches to GEO, it should be easier to get ride-shares. GEO is well clear of the atmosphere and has about 80% more orbit energy than LEO, so it significantly shortens the time to escape.

McInnes presents Sun-coplanar strategy (MI **s**||) using a locally optimal steering law. Figure 3.2a illustrates the orbit in GEO, which requires the sail to slew 180° per orbit and an

instantaneous 180° flip every orbit (at the left illustration within Figure 3.2a). This flip is not necessary if both sides of the sail membrane are reflective, which I assume here. Essentially, as the solar sail moves away from the Sun (right illustration), it points directly at it for maximum thrust along the velocity vector. As it moves towards the Sun (left illustration), the sail is "turned off" by using a cone angle of 90°.

The equation for cone angle as a function of true anomaly f with McInnes' locally optimal steering law is Eq. (4.100) of Ref. 56:

$$\gamma = \frac{1}{2}\left[f - \cos^{-1}\left(\frac{\cos f}{3}\right)\right] \tag{3.3}$$

This law maximizes the acceleration along the velocity vector for a flat sail with attitude control by CM shift, but it does not account for the reduction in thrust seen by solar sails performing attitude control by CP shift, such as the heliogyro. Precession rate ω is the derivative of Eq. (3.3):

$$\frac{d\gamma}{df} = \frac{\omega}{n} = \frac{1}{2} + \frac{\sin f}{6\sqrt{1 - \frac{\cos^2 f}{9}}} \tag{3.4}$$

The required control moment is:

$$M_2 = \omega \Omega I_3 \tag{3.5}$$

The limiting case where precession rate is highest occurs at $f = \pi/2$ where $\gamma = \pi/2$. This is, unfortunately, the attitude at which most sails—including heliogyros—have the least CMA.

MacNeal's Sun-coplanar strategy MN $\boldsymbol{s}\|\ 0\tau$ points the heliogyro at the Sun while using cyclic pitch profiles to change the thrust direction. He uses four blade pitch profiles per orbit: 42° cyclic (top illustration in Figure 3.2b), 90° collective (left illustration), –42° cyclic (bottom illustration), and 0° collective (right illustration).* The idea is similar to McInnes', in that the sail

* Ref. 51 uses 30° vice 42° cyclic and 60° vice 90° collective, but the values I use improve performance.

thrusts away from the Sun when moving away, and it turns the thrust off when moving towards the Sun. As with Sun orthogonal, this strategy has a negligible slew rate compared to McInnes' requirements and the cyclic profile cannot produce as much lateral thrust as slewing a flat sail.

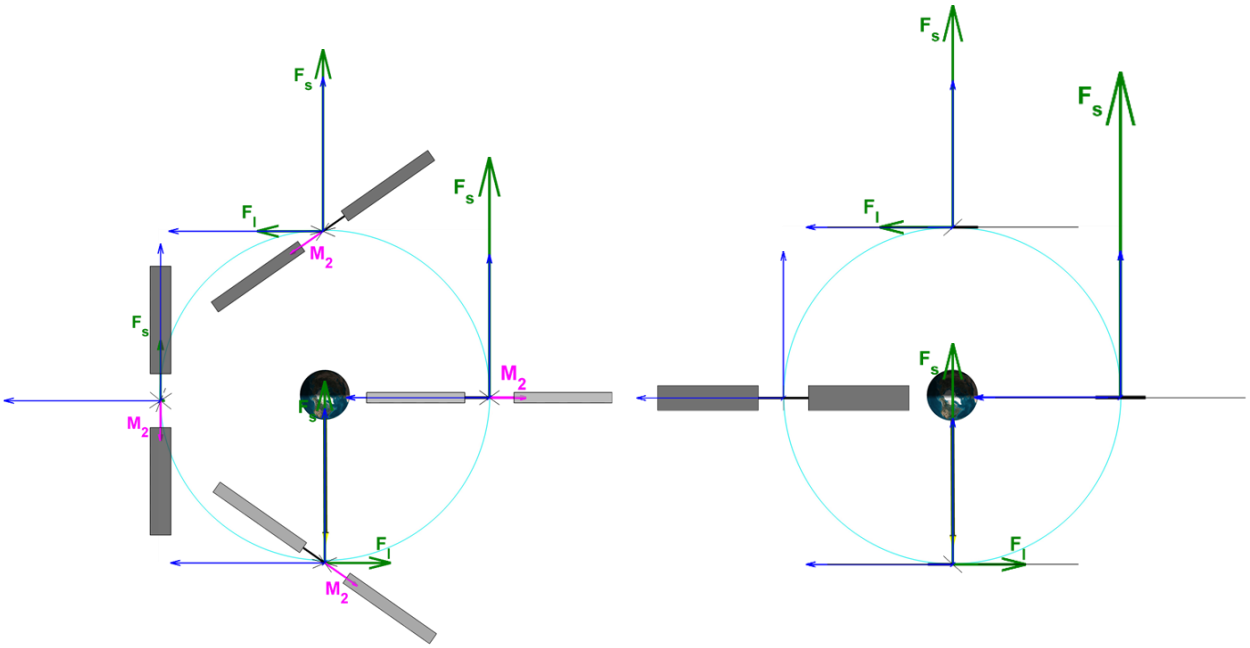

a) McInnes' precessing **b) MacNeal's non-precessing**

Figure 3.2: Illustration of Sun-coplanar (*s*||) escape strategies

Sun-coplanar strategies are asymmetric around the orbit, so eccentricity is continually changing. Initially circular orbits, like GEO, would become more eccentric. Initially eccentric orbits could either become more or less eccentric depending on the angle between the eccentricity vector (the vector pointing at periapse) and the sun. Elliptical orbits could be circularized by choosing a launch epoch that put periapse on the non-thrusting part of the orbit (left illustration in Figure 3.2a & b). The strategy would then raise periapse, a critical issue for ride-shares to geosynchronous transfer orbit (GTO), which have a low periapse with high atmospheric drag.

B. Analytical Performance Metrics

McInnes' compares his escape strategies in Table 4.3 of Ref. 56 using a factor ϵ that I dub the "escape factor":

$$\epsilon = \frac{\Delta r \mu}{a^* r^3} \tag{3.6}$$

This equation assumes a solar sail in a circular orbit with radius r, characteristic acceleration a^*, and a change in radius per orbit of Δr. For other planets, scale the characteristic acceleration relative to the SRP at that planet. McInnes derives this equation from Lagrange's Variation of Parameters for the two-body equations of motion. The escape factor has the advantage of being independent of sail performance (removed by $\Delta r/a^*$), so it is useful for directly comparing escape strategies' relative worth. It is also independent of orbit size for strategies where the sail spin axis is not precessed. For precessing strategies, the precession rate is a proportional to mean motion and therefore inversely proportional to circular orbit radius. Higher precession rates (lower orbits) require larger amplitude pitch profiles, which reduce the net thrust and escape factor. Lastly, it is independent of distance from the sun, so these results hold for other planets.

Eq. (4.89) of Ref. 56 for Δr can be rewritten in terms of ϵ using Eq. (3.6):

$$\epsilon = \frac{2}{a^*} \int_0^{2\pi} a_v(f) df \tag{3.7}$$

Since MacNeal's sun-coplanar law is broken into discrete segments, the escape factor may be calculated analytically.

$$\int_0^{2\pi} a_v(f) df = \int_{-\frac{\pi}{4}}^{\frac{\pi}{4}} {}^{42}_{cy} a_v(f) df + \int_{\frac{\pi}{4}}^{\frac{3\pi}{4}} {}^{90}_{co} a_v(f) df + \int_{\frac{3\pi}{4}}^{\frac{5\pi}{4}} {}^{-42}_{cy} a_v(f) df + \int_{\frac{5\pi}{4}}^{\frac{7\pi}{4}} {}^{0}_{co} a_v(f) df \tag{3.8}$$

The front sub- and superscripts indicate the pitch profile and amplitude respectively during each arc. The acceleration along the velocity vector in terms of the Sun-frame force components is:

$$a_v m = -F_s \sin f + F_l \cos f \tag{3.9}$$

Several of these force components are known:

$$
{}^{90}_{co}F_l = {}^{90}_{co}F_s = {}^{0}_{co}F_l = 0, \qquad {}^{42}_{cy}F_s = {}^{-42}_{cy}F_s, \qquad {}^{-42}_{cy}F_l = -{}^{42}_{cy}F_l,
$$

$$
{}^{0}_{co}F_s = a^* m \tag{3.10}
$$

Substitute Eqs. (3.9) & (3.10) into (3.8) and simplify:

$$
m\int_0^{2\pi} a_v(f)df =
$$

$$
= -{}^{42}_{cy}F_s \int_{-\frac{\pi}{4}}^{\frac{\pi}{4}} \sin f \, df + {}^{42}_{cy}F_l \int_{-\frac{\pi}{4}}^{\frac{\pi}{4}} \cos f \, df
$$

$$
- {}^{42}_{cy}F_s \int_{\frac{3\pi}{4}}^{\frac{5\pi}{4}} \sin f \, df - {}^{42}_{cy}F_l \int_{\frac{3\pi}{4}}^{\frac{5\pi}{4}} \cos f \, df - {}^{0}_{co}F_s \int_{\frac{5\pi}{4}}^{\frac{7\pi}{4}} \sin f \, df
$$

$$
= -{}^{42}_{cy}F_s 0 + {}^{42}_{cy}F_l\sqrt{2} - {}^{42}_{cy}F_s 0 + {}^{42}_{cy}F_l\sqrt{2} + {}^{0}_{co}F_s\sqrt{2}
$$

$$
= \sqrt{2}\left(2\,{}^{42}_{cy}F_l + {}^{0}_{co}F_s\right) \tag{3.11}
$$

Substituting Eq. (3.11) into Eq. (3.6) gives a compact formulation of escape factor for this strategy:

$$
\epsilon = 2\sqrt{2}\left(2\frac{{}^{42}_{cy}F_l}{{}^{0}_{co}F_s} + 1\right) \tag{3.12}
$$

The ratio ${}^{42}_{cy}F_l / {}^{0}_{co}F_s$ = 0.2246 always, regardless of heliogyro dimensions and distance to the sun, and it can be found using the `HGForce` algorithm developed in Chapter 2.A.

Simulations can be used to validate the escape factor using the initial and final semi-major axes, regardless of the number of orbits, as long as the eccentricity stays small. First, maintain the circular orbit assumption so that the time derivative of true anomaly is the mean motion:

$$
\frac{df}{dt} \cong n = \sqrt{\frac{\mu}{a^3}} \tag{3.13}
$$

Then the change in semi-major axis per orbit Δa is:

$$\Delta a = 2\pi \frac{da}{df} = 2\pi \frac{da}{ndt} = 2\pi \sqrt{\frac{a^3}{\mu}} \frac{da}{dt} \tag{3.14}$$

Substitute Eq. (3.14) into Eq. (3.6), integrate, and simplify:

$$\epsilon = \frac{2\pi\mu}{a^* a^3} \sqrt{\frac{a^3}{\mu}} \frac{da}{dt} = \frac{2\pi}{a^*} \sqrt{\frac{\mu}{a^3}} \frac{da}{dt} \tag{3.15}$$

$$\begin{aligned} \epsilon a^* \int_{t_0}^{t_f} dt &= 2\pi\sqrt{\mu} \int_{a_0}^{a_f} a^{-\frac{3}{2}} da \\ \epsilon a^* (t_f - t_0) &= 4\pi\sqrt{\mu} \left(\frac{1}{\sqrt{a_0}} - \frac{1}{\sqrt{a_f}} \right) \end{aligned} \tag{3.16}$$

$$\epsilon = \frac{4\pi}{a^*(t_f - t_0)} \left(\sqrt{\frac{\mu}{a_0}} - \sqrt{\frac{\mu}{a_f}} \right) \tag{3.17}$$

Therefore, the escape factor may be estimated using the initial and final semi-major axis and the simulation duration. Eqs. (3.18) to (3.24) are a collection of the above derivations along with other useful formulations of escape factor:

For a_v constant (Sun-orthogonal strategies): $\epsilon = 4\pi \frac{a_v}{a^*}$ (3.18)

For McInnes' ideal Sun-orthogonal strategy:[56] $\epsilon = \frac{8\pi}{3\sqrt{3}} = 4.84$ (3.19)

For MacNeal's Sun-orthogonal strategy: $\epsilon = 4\pi \frac{{}^{42}_{cy}F_l}{{}^{0}_{co}F_s} = 2.82$ (3.20)

For a_v a function of f (Sun-coplanar strategies): $\epsilon = \frac{2}{a^*} \int_0^{2\pi} a_v(f) df$ (3.21)

For McInnes' ideal Sun-coplanar strategy:[56] $\epsilon = 5.52$ (3.22)

For MacNeal's Sun-coplanar strategy: $\epsilon = 2\sqrt{2} \left(2 \frac{{}^{42}_{cy}F_l}{{}^{0}_{co}F_s} + 1 \right) = 4.10$ (3.23)

For measuring from numerical simulations: $$\epsilon = \frac{4\pi}{a^*(t_f - t_0)}\left(\sqrt{\frac{\mu}{a_0}} - \sqrt{\frac{\mu}{a_f}}\right) \quad (3.24)$$

Another useful comparison is an estimate of the escape time. McInnes develops an analytical estimate of escape time t_∞ by assuming the orbit remains circular and the escape factor is constant. Eq. (3.25) reformulates Eq. (4.113) of Ref. 56 by substituting Eq. (3.21):

$$t_\infty = \frac{4\pi}{\epsilon a^*}\sqrt{\frac{\mu}{a_0}} \quad (3.25)$$

The assumption of constant ϵ may be relaxed by returning to the original integral of Eq. (3.26) and integrating to Earth's sphere of influence (SOI) $r_{SOI} \cong$ 1e6 km.

$$t_\infty = \frac{2\pi\sqrt{\mu}}{a^*}\int_{a_0}^{r_{SOI}} \frac{dr}{\epsilon(a)a^{3/2}} \quad (3.26)$$

I use these two performance metrics, ϵ and t_∞, to compare the relative performance of the escape strategies presented in the next section. The circular-orbit assumption is particularly invalid for Sun-coplanar strategies, so Eqs. (3.25) & (3.26) are only rough approximations for actual escape time. Nevertheless, they are still useful measures of relative performance.

C. Strategy Analysis and Comparison

This subchapter presents the escape factor found for all the strategies presented earlier. Precessing strategies take into account the reduction in thrust when performing Precession Tactic necessary to follow that strategy's steering law. I also ran numerical simulations in the Copernicus trajectory optimizer to confirm the escape factor calculations. Copernicus, developed by NASA Johnson Space Center (JSC), has a relatively low overhead, intuitive GUI, capable optimization module, and great flexibility for representing low-thrust, solar electric propulsion (SEP) trajectories, but it does not simulate solar sails.[55] Through judicious selection of settings,

Copernicus can represent a solar sail trajectory as a series of SEP segments that account for eclipsing and distance from the Sun. The only noteworthy restriction is that the baseline thrust magnitude (before accounting for eclipsing and distance to the Sun) and thrust cone angle (angle between ***F*** and ***s***) must be piecewise linear. The specific settings used are in APPENDIX A.

*1. Sun-orthogonal trajectories (**s**⊥)*

Figure 3.3 presents the escape factors for MacNeal's (MN) and McInnes' (MI) Sun-orthogonal strategies along with two modified strategies that account for the required precession of a heliogyro. As mentioned earlier, the escape factor varies by orbit radius when accounting for the required heliogyro precession torque. Figure 3.3 uses orbit-radii of 7878 km (1500 km altitude) out to 1e6 km, just beyond the Earth's SOI.

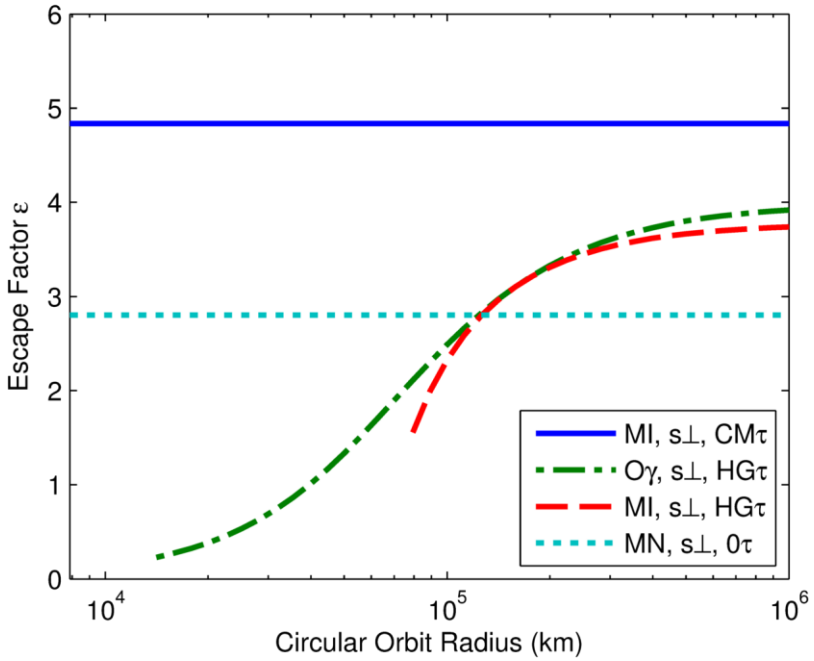

Figure 3.3: Sun-orthogonal (*s*⊥) escape strategy relative performance (MN = MacNeal, MI = McInnes, Oγ = optimized cone angle, CMτ = precession torque by CM shift, HGτ = HELIOS using the Precession Tactic, 0τ = no precession torque required)

MacNeal's original strategy (MN **s**⊥ 0τ) changes the thrust direction with a cyclic profile, so it requires no precession torque (0τ); however, its escape factor is 40% worse than McInnes' ideal strategy (MI **s**⊥ CMτ) that precesses the entire spacecraft. McInnes' strategy implies torque

by CM shift (CMτ) and is therefore possible for kite sails but not for heliogyros. These two escape factors come from Eqs. (3.20) & (3.19), respectively. MI $\boldsymbol{s}\perp$ HGτ diminishes the thrust of McInnes' strategy to account for the torque HELIOS would require (HGτ) to precess its spin axis about a 35° cone. To do this, I find the M_3 required for precession at each orbit radius from Eq. (3.1), then I use the Precession Tactic of Chapter 2.B.2 to determine the required pitch profile and net thrust remaining. Lastly, I convert the reduced thrust to acceleration and substitute into Eq. (3.18). The resulting performance is substantially less than the ideal case. Furthermore, the M_3 required exceeds HELIOS' capability below about 80,000 km.

The optimal cone angle for a heliogyro is no longer 35° since the blade pitch profile required to precess the heliogyro spin axis significantly reduces the available thrust and slightly changes the solar thrust direction. Smaller cone angles require less torque to precess and so have more thrust available, but larger cone angles direct more of the available thrust along the velocity vector. Oγ $\boldsymbol{s}\perp$ HGτ is a new strategy I developed that optimizes the cone angle γ (Oγ) at each orbit radius to maximize thrust in the velocity direction. It follows a procedure similar to that of MI $\boldsymbol{s}\perp$ HGτ, except that it determines the optimal cone angle at each altitude by iteration. Figure 3.4 shows how the resulting cone angle varies with orbit radius. The Oγ $\boldsymbol{s}\perp$ HGτ strategy slightly improves on the non-ideal McInnes' strategy applied to a heliogyro (MI $\boldsymbol{s}\perp$ HGτ) from Figure 3.3. Considering all these strategies, the best Sun-orthogonal strategy for HELIOS would therefore be MacNeal's strategy (MN $\boldsymbol{s}\perp$ 0τ) to an orbit of about 120,000 km and then switch to the optimized cone angle strategy (Oγ $\boldsymbol{s}\perp$ HGτ) for the rest of the escape. This strategy would escape in 2.4 years per Eq. (3.26), too long to be compelling for interplanetary missions, but it could be applied to planetary missions desiring a change in orbit energy without escaping.

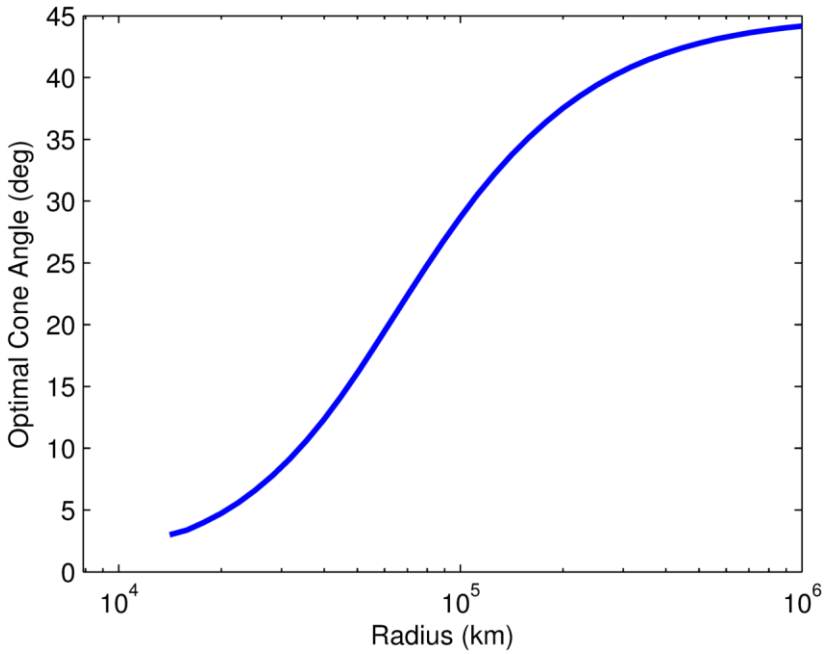

Figure 3.4: Optimal cone angle vs. circular orbit radius in a Sun-orthogonal orbit

Figure 3.5 shows a simulation of MacNeal's strategy in Copernicus using the HELIOS parameters of Table 1.6. The initial orbit is Sun-synchronous at 1500 km altitude to be above most atmospheric effects. It has a 102° inclination, and I choose the epoch and right ascension of the ascending node (RAAN) to make the Sun perpendicular to the orbit plane. In this and all subsequent Copernicus figures, the thick set of axes represent the Earth-fixed coordinates and the thin set of axes are in the Earth-Sun, two-body rotating frame. The Sun lies along the thin x-axis. The spacecraft orbit is the cyan line, and the red lines represent exaggerated thrust vectors at each integration step. This orbit equates to an escape factor of 2.78 using Eq. (3.24), and is therefore only 1% away from the analytical result of 2.82 from Eq. (3.20).

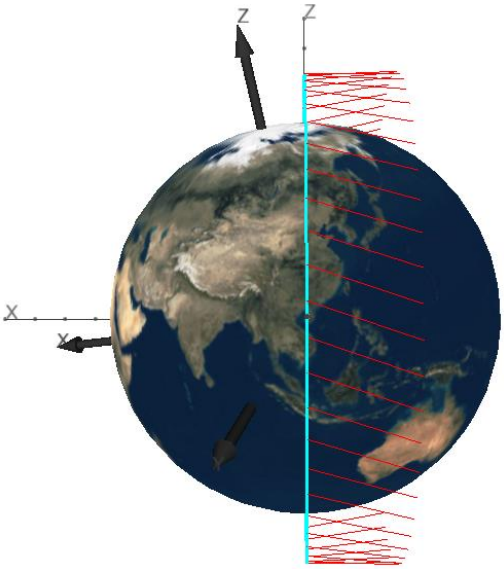

Figure 3.5: MacNeal's MN s⊥ 0τ strategy at a 1500-km altitude SSO

As the orbit grows, it is impossible to maintain Sun-synchronicity, so the Sun cannot stay orthogonal to the orbit plane indefinitely. Figure 3.6 shows a Copernicus simulation of this strategy for 150 days in the Earth-Sun rotating frame. The first 60 days (cyan) have a much smaller change in the relative position of the Sun because the Earth's oblateness precesses the orbit plane. In the last 90 days (green) the orbit plane rapidly rotates with respect to the Sun because the altitude is too high for oblateness to take much effect. After 150 days, the Sun is 42° from the orbit plane, so one would switch to a Sun-coplanar strategy of the next section. Furthermore, while this trajectory does not yet experience eclipse, it will enter Earth's shadow within a further 30 days.

Notice that the orbit does not start orthogonal to the Sun in Figure 3.6. Instead, I optimize the initial epoch and RAAN to maximize the final orbit periapse. When starting from LEO, staying well above the atmosphere is more important than maximizing orbit energy, and maximizing periapse limits eccentricity growth. Even so, eccentricity reaches 0.1. The final change in orbit semi-major axis a is 4076 km, which equates to an average escape factor of 2.63. This is only 6% below the analytical escape factor, which is surprising considering how far from orthogonal the Sun is for most of the trajectory.

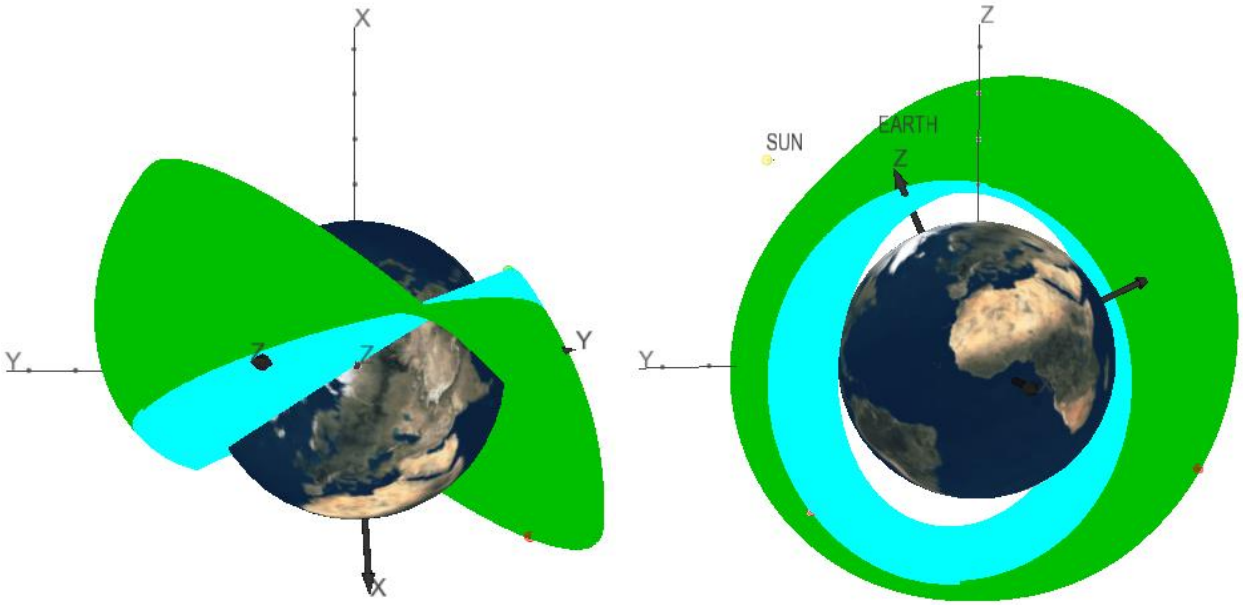

a) Top view looking down from ecliptic north **b) Back view looking towards the Sun**

Figure 3.6: MN s⊥ 0τ for five months starting from a 1500-km altitude SSO

Three design parameters, discussed in Chapter 2.C.2, could be varied to make the precessing strategies more competitive with non-precessing ones: increase the ratio of sail area to blade radius, lower the spin rate, or lower sail loading. Any of these changes would allow the heliogyro to precess at the same rate without diverting as much SRP thrust for moment generation. Figure 3.7 varies the spin rate and shows the orbit radius above which the precessing strategies (MI $\boldsymbol{s}\perp$ CMτ and Oγ $\boldsymbol{s}\perp$ HGτ) just presented have higher escape factors than the non-precessing (MN $\boldsymbol{s}\perp$ 0τ) strategy. Even at a spin rate of 0.1 RPM (which is likely to cause instability[26]) MacNeal's non-precessing strategy (MN $\boldsymbol{s}\perp$ 0τ) is preferable below 27,000 km, well above LEO.

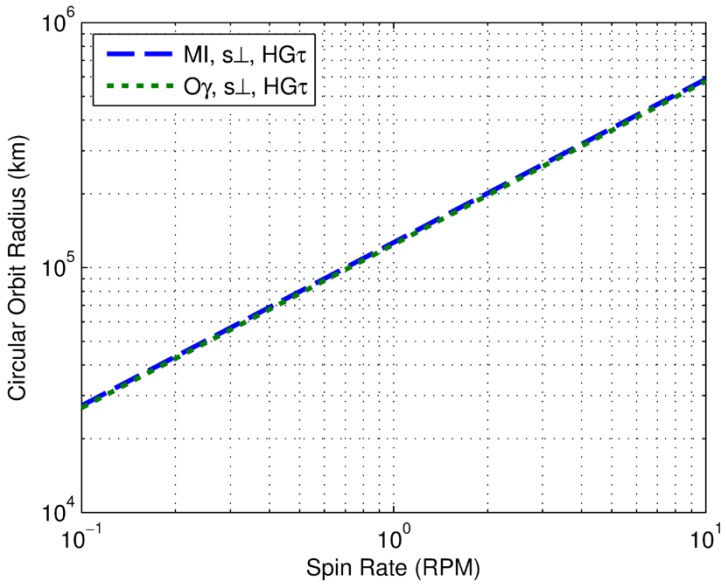

Figure 3.7: Spin rate where the precessing strategies reach parity with MacNeal's MN *s*⊥ 0τ

*2. Sun-coplanar trajectories (**s**||)*

Sun-coplanar strategies would be useful for ride-shares to GEO. MacNeal's original strategy uses four discrete pitch profiles to thrust along the velocity vector, again without precessing the heliogyro. I improve upon his original strategy by iterating to find the locally optimal pitch profile to maximize thrust along the velocity vector for a given true anomaly. Figure 3.8 compares MacNeal's and the optimized blade pitch profiles.

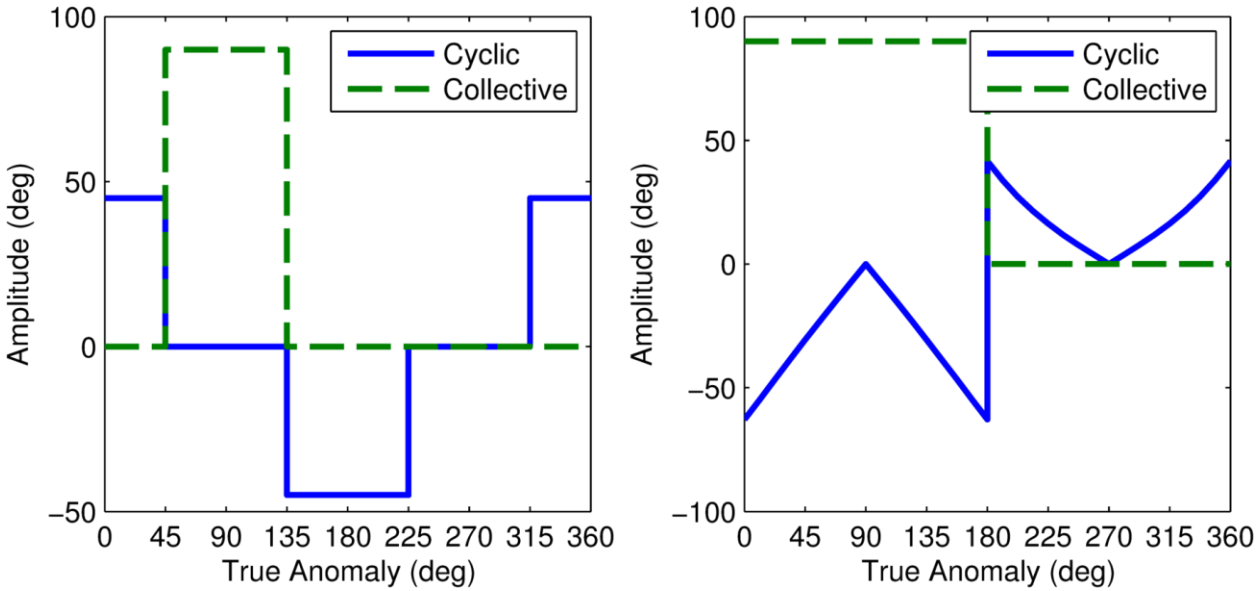

a) MacNeal's concept (MN) **b) New, optimized profile (OP)**

Figure 3.8: Pitch profiles for Sun-coplanar (*s*||), no precession (0τ) strategies

MacNeal's profile makes four discontinuous jumps every 45° true anomaly, while the optimized profile has two discontinuities at 0 and 180° but otherwise varies the profile smoothly. In the optimized profile, the backside of the blades would be illuminated from 0 to 180° true anomaly. This further reinforces the advantages of allowing both sides of the blade to be illuminated when considering blade design. MacNeal's concept would also likely see some backside illumination when at the 90° collective considering flexible blade transients, but this glancing illumination would not drive blade design. Figure 3.9 depicts these two strategies' resulting thrust vectors in orbit to better illustrate the maximization of thrust along velocity.

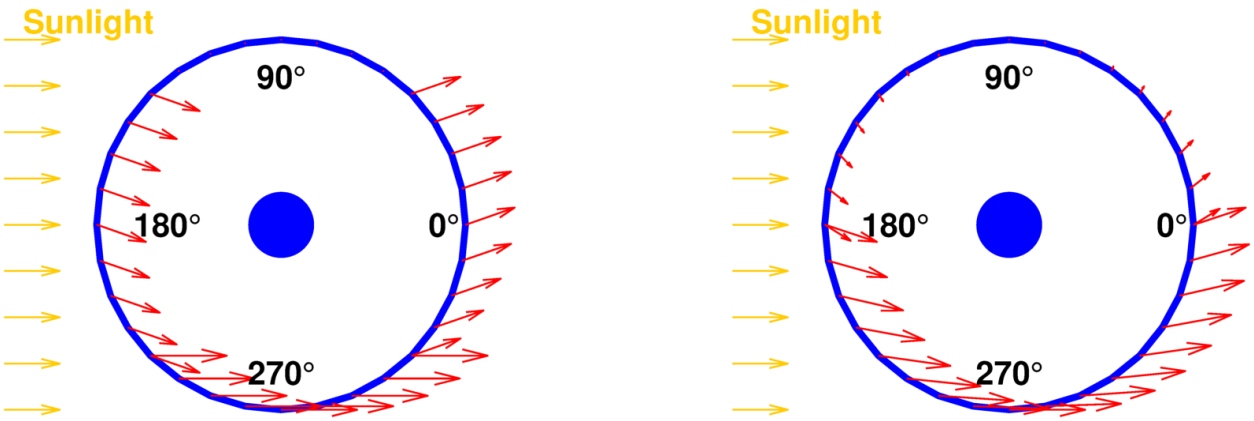

a) MacNeal's original concept (MN) **b) New, optimized profile (OP)**

Figure 3.9 Illustration of thrust vectors (red arrows) for Sun-coplanar (*s*||), no precession (0τ)

Figure 3.10 shows the relative performance of all Sun-coplanar strategies. Three strategies do not vary with orbit radius: McInnes' ideal Sun-coplanar strategy MI ***s***|| CMτ, MacNeal's MN ***s***|| 0τ, and my optimized profile strategy OP ***s***|| 0τ. These lines come from Eqs. (3.22), (3.23), and (3.21), respectively. I determine the acceleration of OP ***s***|| 0τ for use in the integral of (3.21) by using HGForce on the pitch profiles of Figure 3.8b. McInnes' strategy applied to the heliogyro MI ***s***|| HGτ varies with orbit radius because it accounts for the reduction in thrust HELIOS would experience when generating the required torque for precession. I find the required moment M_2 at each point in the orbit from Eq. (3.5), use the Precession Tactic to determine the net thrust and acceleration, and then numerically integrate per Eq. (3.21) for the escape factor at each orbit radius.

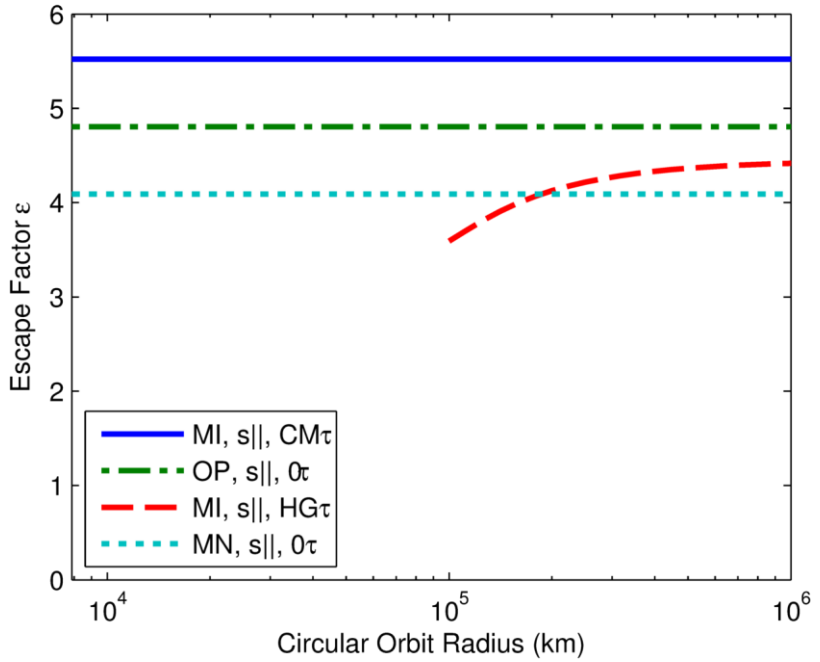

Figure 3.10: Sun-coplanar (*s*||) escape strategy relative performance (MI = McInnes, MN = MacNeal, OP = optimized blade pitch profile, CMτ = precession torque by CM shift, 0τ = no precession torque required, HGτ = HELIOS using the Precession Tactic)

The optimized profile strategy OP ***s***|| 0τ is 17% better than MacNeal's MN ***s***|| 0τ. McInnes' ideal MI ***s***|| CMτ is the highest performer because it uses the full sail area for thrust vectoring, so it does not apply to heliogyros. When accounting for the required precession torque, MI ***s***|| HGτ is worse than MacNeal's original strategy MN ***s***|| 0τ below about 200,000 km, and it is never better than the new, optimized pitch profile strategy OP ***s***|| 0τ. Even if the spin rate were dropped to 0.1 RPM—which would likely lead to blade instabilities—the maximum escape factor would only be 4.4. This is still worse than the optimized pitch profile strategy's escape factor of 4.8. The best strategy for HELIOS to escape from Sun-coplanar orbits would be the new, optimized pitch profile strategy OP ***s***|| 0τ for the entire escape. In fact, it is 87% as good as McInnes strategy MI ***s***|| CMτ that is theoretically the best but invalid for the heliogyro. The escape time estimate from LEO for this strategy is 515 days, 40% shorter than the best Sun-orthogonal strategy. Escape from GEO would only take 150 days, 70% less time than from LEO.

Figure 3.11 shows simulations of HELIOS using the optimized pitch profile strategy OP ***s***|| 0τ at LEO and GEO. Both cases account for eclipsing, as evidenced by the disappearance of red thrust vectors around the –x-axis, and they start at an equinox for worst-case eclipsing.

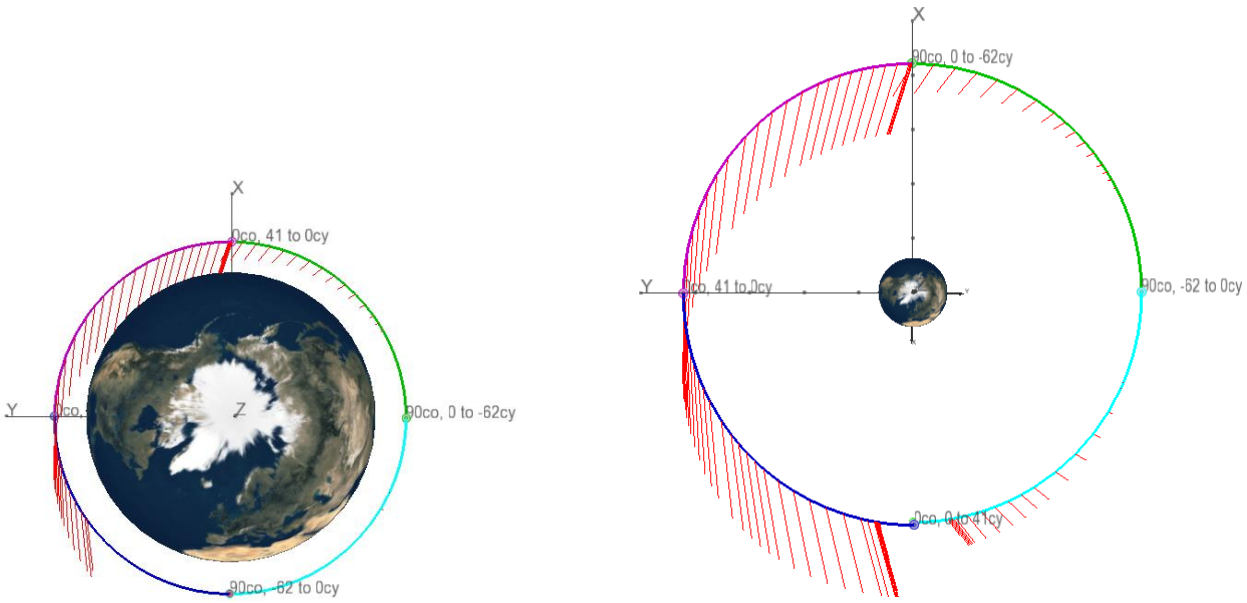

a) 1500-km altitude LEO **b) GEO**

Figure 3.11: OP *s*|| 0τ, accounting for eclipsing

Without eclipsing, the escape factor is 5.16 in LEO and 4.93 GEO, both slightly above the analytical value of 4.8 from Figure 3.10. This small difference may come from inaccuracies in Copernicus' thrust modeling discussed earlier. When accounting for eclipsing, the LEO escape factor drops by 25% to 3.87. Even with this large penalty, however, it is still 37% better than the best heliogyro Sun-orthogonal strategy. The worst-case eclipse penalty in GEO is only 3.2%, dropping the escape factor to 4.77. Furthermore, GEO only experiences eclipse for 46 days twice a year,[61] so the net eclipse penalty is immaterial.

D. Chapter Summary and Recommendations

There is significant reduction in performance of strategies that require precession of the heliogyro spin axis when accounting for the blade pitch profiles required to generate the attitude

control moments. The reduction is such that the non-precessing strategies are preferred out to circular, Earth orbit radii of at least 100,000 km. These non-precessing strategies would change the thrust direction using cyclic blade pitch profiles. Furthermore, the best non-precessing strategy is almost 87% as good as the best, idealized precessing strategy that makes assumptions that are invalid for the heliogyro. Considering that the heliogyro generally at least doubles the characteristic acceleration over other kite sail architectures (see Table 1.7), the heliogyro is still the preferred architecture by a large margin.

Table 3.2 summarizes the Sun-orthogonal and Sun-coplanar strategies. The best Sun-coplanar strategy escapes about 40% faster than the best Sun-orthogonal strategy when starting from the same orbit radius. Moreover, it is easier to get ride-shares above LEO when going to Sun-coplanar orbits (e.g. GEO). Starting from GEO instead of LEO would cut the escape time by 70% from 515 days to only 150 days, a considerable operational savings. Furthermore, the Sun-orthogonal geometry cannot be maintained throughout escape as the Earth orbits the Sun. Therefore, both orbit families would experience eclipsing during escape from LEO, but eclipsing is negligible at GEO or higher. Therefore, I recommend pursuing a ride-share to GEO followed by my new, optimized blade pitch profile (OP $\boldsymbol{s}\|\ 0\tau$) strategy for interplanetary missions where direct injection into heliocentric orbit is impractical.

Table 3.2: Summary of Earth escape strategy results

Initial orbit	**Sun-orthogonal**	**Sun-coplanar**
Highest practical ride-share	LEO	GEO
Max eclipsing per orbit	None initially	LEO: 25%
(cylindrical shadow model)	20% after 6 months	GEO: 5%
Maintaining Sun alignment	<45° for up to 150 days	±23° throughout escape
Eccentricity change	Small	Large
Escape factor of best strategy	2.9	4.8
Estimated escape time	LEO: 860 days	LEO: 515 days
		GEO: 150 days

CHAPTER 4. BLADE CONTROL

In this chapter, I examine the stability and effectiveness of a torque-source motor at the blade root to control blade pitch, as applied to HELIOS. The corresponding controller employs a proportional/derivative/feed-forward (PDFF) law. To perform this analysis, I derive a simplified finite element model (FEM) of a single heliogyro blade with freedom in twist only in Chapter 4.A that I call the membrane ladder. I then convert it to a linear, time-invariant (LTI) state-space system to perform a linear control and stability analysis in Chapter 4.B. This step is a necessary condition for nonlinear controller stability. In Chapter 4.C, I analyze a novel method of blade tip control that varies the local reflectivity to create torques on the blade. I relate the results of experiments to determine the frequency response function (FRF) of a small-scale, hanging blade in a vacuum chamber in Chapter 4.D. This experiment is useful for validating the FEM and estimating material damping. Lastly, I look at nonlinear dynamics in Chapter 4.E. In particular, I develop the nonlinear describing function (DF) to investigate mode frequency shift with amplitude, and I simulate the performance of a nonlinear PDFF controller for a range of practical pitch profile applications. The goal of this chapter is to develop a clear understanding of the relationship between the material damping, controller bandwidth, centrifugal stiffness, and closed loop blade twist stability, tracking, and performance.

A. Finite Element Model

The membrane ladder FEM makes assumptions to lower the computational cost compared to commercial finite element analysis (FEA) programs, make it more accessible to analytical and parametric investigation, and allow for feedback control. Table 4.1 presents the simplifying assumptions alongside their justifications.

Table 4.1: Membrane ladder FEM assumptions

Assumption	Justification
Twist motion is uncoupled from other motions.	Flap and lead-lag bending should be <1° over the length of the blade per Eq. (2.3).
Cross-sections remain undistorted (no blade camber).	HELIOS uses periodic battens to minimize camber.
Elastic stiffness plays no role (membrane material is inelastic in tension and compliant in bending).	Very little tension strain expected. Compliance in bending is a conservative assumption, but bending stiffness is expected to be small.
Material/structural damping is negligible	This is a conservative assumption, but this damping is expected to be small.

This model's equations of motion (EOM) are similar to those first developed by MacNeal,[51] but MacNeal makes the additional assumption of a homogenous blade since he was using continuous equations. The membrane ladder FEM can handle an arbitrary mass distribution, so it allows for blade features like battens and edge reinforcing. One should visualize the membrane ladder as a series of rigid rungs connected by massless membranes with zero elastic torsional stiffness. Each rung contains the mass and moment of inertia of a whole blade element. The free-body diagram of a single rung shown in Figure 4.1 is used to derive the equations of motion. Note that the blade number is unimportant for the individual blade dynamics investigations of this chapter, so the blade pitch subscript is written θ_n to denote the *n*th rung's pitch as opposed to the *i*th blade's pitch in other chapters.

First, the gyroscopic torque τ^g comes from the centrifugal force acting on mass out of the plane of rotation, it tends to restore blade pitch toward zero (blade flat in the plane of rotation), and it is sometimes called the "tennis racket effect" in helicopter blade dynamics:[53]

$$\tau_n^g = -J_n \Omega^2 \sin\theta_n \cos\theta_n = -K_n^g \sin\theta_n \cos\theta_n = -K_n^g \frac{1}{2} \sin 2\theta_n \tag{4.1}$$

$$J_n = \frac{\rho hc^3 \Delta x + m_{n,bar} c^2}{12} \tag{4.2}$$

The cosine factor in Eq. (4.1) comes from the fact that the restoring force is maximized at zero pitch and zero at 90° pitch. The sine factor results from the lever arm of the force being zero at zero pitch and maximized at 90°. The rung's mass moment of inertia J_n includes two terms: the sail membrane and any discrete bar masses $m_{n,bar}$ in that element (e.g. chordwise battens). Point masses at the twist axis do not contribute to J_n, so they do not affect the gyroscopic stiffness K^g.

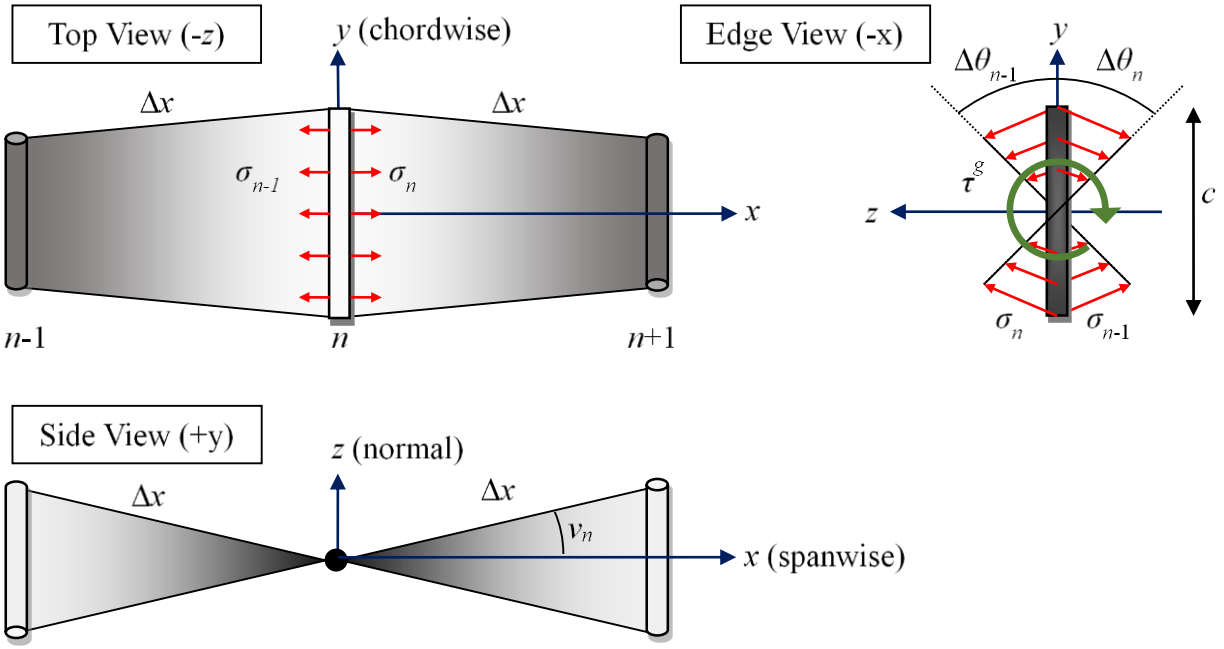

Figure 4.1: Free body diagram of rung *n* in the membrane ladder FEM

Second, the centrifugal torque τ^c is the torque that tends to flatten any twisted membrane under tension. In the heliogyro's case, the centrifugal force provides this tension force as follows:

$$T_n = \Omega^2 \left[\underbrace{\frac{1}{2}\rho hc(R^2 - x_n^2)}_{\text{sail memebrane}} + \underbrace{m_{tip} R}_{\text{all tip mass}} + \underbrace{\sum_{j=\left\lceil (N_{bat}+1)\frac{x_n}{R} \right\rceil}^{N_{bat}} j \frac{m_{bat} R}{N_{bat}+1}}_{\text{evenly-spaced battens}} \right] \tag{4.3}$$

The batten term increases the tension at rungs inboard of each batten's location (a ceiling function determines *j*) and assumes even batten spacing. The tip mass term can include both bar masses (e.g. battens) that contribute to the rotational moment of inertia and point masses that do not.

The membrane ladder assumes this tension is a stress uniformly distributed chordwise:

$$\sigma_n = \frac{T_n}{hc} \tag{4.4}$$

where *hc* is the blade cross-sectional area. This stress always lies in the direction of the attached membrane, so it has a component in the *z*-direction if the membrane is twisted. To find the centrifugal torque, one must integrate the tension and lever arm along *y* over the blade chord *c*:

$$\tau_n^c = \sigma_n h \sin \nu_n \int_{-c/2}^{c/2} y dy \tag{4.5}$$

where ν_n is the vertical membrane deflection angle. Inspection of Figure 4.1 reveals that:

$$\begin{gathered} z = y \tan \Delta\theta_n = \Delta x \sin \nu_n \\ \sin \nu_n = \frac{y \tan \Delta\theta_n}{\Delta x} \end{gathered} \tag{4.6}$$

Substitute Eq. (4.6) into (4.5) and integrate chordwise:

$$\tau_n^c = \frac{\sigma_n h c^3}{12 \Delta x} \tan(\theta_{n+1} - \theta_n) \tag{4.7}$$

Another possible formulation of the centrifugal stiffness used herein I call the rope ladder. The membrane ladder evenly distributes the tension along the chord, while the rope ladder concentrates tension along the leading and trailing edges, as shown in Figure 4.2. The centrifugal torque does not require integration in the rope ladder; just multiply the force and lever arm:

$$\tau_n^c = 2 \frac{T_n}{2} \frac{c}{2} \sin \nu_n = \frac{T_n c^2}{4 \Delta x} \tan(\theta_{n+1} - \theta_n) \tag{4.8}$$

In reality, the stress distribution would lie somewhere between these two extremes, but careful engineering could bring the distributions closer to one or the other of these models.

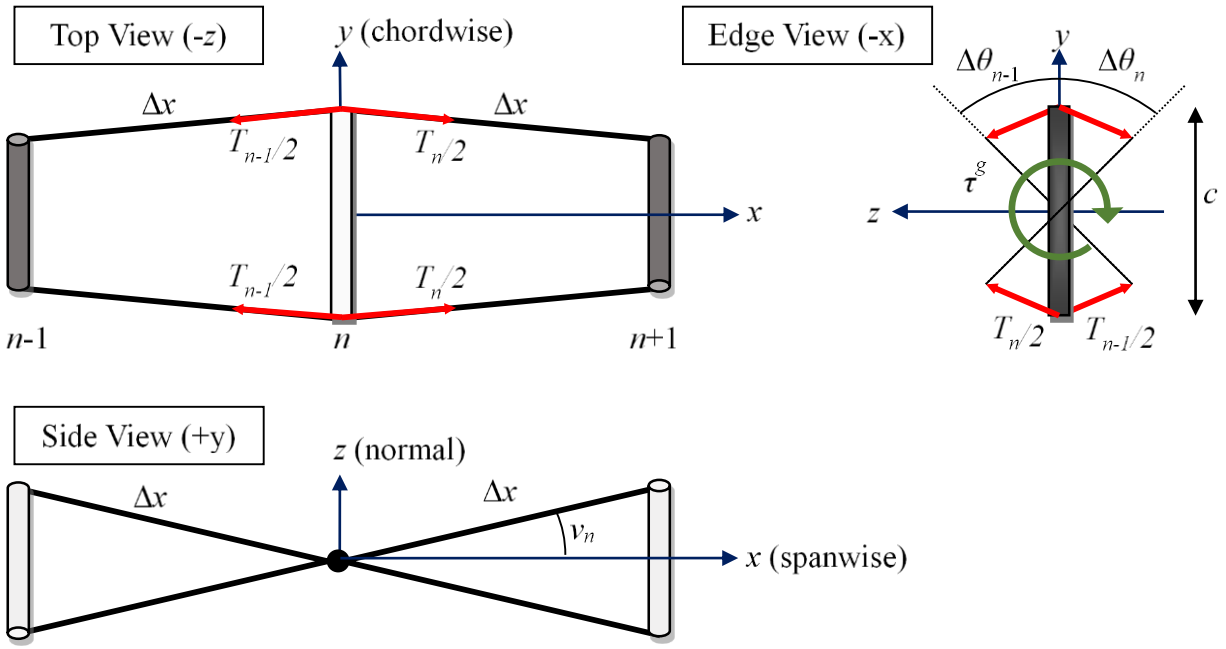

Figure 4.2: Free body diagram of rung *n* in the rope ladder FEM

Centrifugal stiffness is the part of centrifugal torque independent of blade pitch:

Centrifugal stiffness, membrane ladder: $$K_n^c = \frac{T_n c^2}{12\Delta x} \quad (4.9)$$

Centrifugal stiffness, rope ladder: $$K_n^c = \frac{T_n c^2}{4\Delta x} \quad (4.10)$$

Note that the rope ladder has a centrifugal stiffness multiplier in Eq. (4.10) of 1/4th vice the 1/12th of the membrane ladder in Eq. (4.9), thus tripling the centrifugal stiffness. Ref. 54 mentions this tripling and its cause, but without derivation.

The full FEM with *N* elements has *N*+1 blade rungs, and each rung's EOM sums the gyroscopic and centrifugal torques:

$$J_1\ddot{\theta}_1 = -K_1^g \frac{1}{2}\sin 2\theta_1 + K_1^c \tan(\theta_2 - \theta_1) + \tau_1 \tag{4.11}$$

$$J_n\ddot{\theta}_n = -K_n^g \frac{1}{2}\sin 2\theta_n + K_n^c \tan(\theta_{n+1} - \theta_n) - K_{n-1}^c \tan(\theta_n - \theta_{n-1}) \tag{4.12}$$

$$J_{N+1}\ddot{\theta}_{N+1} = -K_{N+1}^g \frac{1}{2}\sin 2\theta_{N+1} - K_N^c \tan(\theta_{N+1} - \theta_N) \tag{4.13}$$

Except at the blade root ($n = 1$) and tip ($n = N+1$), each rung attaches to an outboard and an inboard membrane, so the centrifugal torque has two components. The blade root also has an applied torque τ_1 from the root pitch actuator. The extra Euler and Coriolis terms typical of EOM in a rotating frame are zero for the twist-only case. Note that a blade element with no chordwise bending (camber) does not experience SRP torque since SRP balances about the blade midline.

B. Linear Control and Stability Analysis

While, nonlinear effects play an important part in blade control, linear analysis is crucial to a baseline understanding of the dynamics and control system development. Since any real structure will have some material damping, I add a material damping term to the baseline EOM. This is necessary for the controller bandwidth investigation of Chapter 4.B.4. As with centrifugal stiffening, all rungs except the ends have two components.

$$\tau^d = \frac{\kappa}{\Delta x}\left[\left(\dot{\theta}_{n+1} - \dot{\theta}_n\right) - \left(\dot{\theta}_n - \dot{\theta}_{n-1}\right)\right] = \frac{\kappa}{\Delta x}\left(\dot{\theta}_{n+1} - 2\dot{\theta}_n + \dot{\theta}_{n-1}\right) \tag{4.14}$$

Division by Δx ensures that there is less damping per unit twist angle in long elements and more in short elements; a long element would experience less membrane stretching for the same relative twist across the element. The damping constant κ (Nm^{2}s/rad) is a complex function of temperature, stress, and excitation frequency in polymers, so it must be derived experimentally. Furthermore, this representation of damping produces a linear increase in damping ratio with frequency, and

true material damping may not behave in this fashion. I investigate the blade's true material damping magnitude and character through vacuum chamber experiments in Chapter 4.D.

1. Linearization and conversion to state space

Linearize the EOM by taking small angle approximations of (4.11) to (4.13):

$$J_1\ddot{\theta}_1 = -K_1^g\theta_1 + K_1^c(\theta_2 - \theta_1) + \frac{\kappa}{\Delta x}(\dot{\theta}_2 - \dot{\theta}_1) + \tau_1$$

$$J_n\ddot{\theta}_n = -K_n^g\theta_n + K_n^c(\theta_{n+1} - \theta_n) - K_{n-1}^c(\theta_n - \theta_{n-1}) + \frac{\kappa}{\Delta x}(\dot{\theta}_{n+1} - 2\dot{\theta}_n + \dot{\theta}_{n-1}) \quad (4.15)$$

$$J_{N+1}\ddot{\theta}_{N+1} = -K_{N+1}^g 2\theta_{N+1} - K_N^c(\theta_{N+1} - \theta_N) + \frac{\kappa}{\Delta x}(-\dot{\theta}_{N+1} + \dot{\theta}_N)$$

Eqs. (4.15) represents a LTI system that converts to state-space as follows:

$$\dot{\boldsymbol{X}} = \begin{bmatrix}\boldsymbol{\theta}\\ \dot{\boldsymbol{\theta}}\end{bmatrix} = A\boldsymbol{X} + Bu, \qquad \boldsymbol{Y} = \begin{bmatrix}\theta_1\\ \dot{\theta}_1\\ \theta_{N+1}\end{bmatrix} = C\boldsymbol{X} + D\boldsymbol{u} \quad (4.16)$$

$$A = \begin{bmatrix}[0]_{N+1\times N+1} & [I]_{N+1\times N+1}\\ A^* & D^*\end{bmatrix}$$

$$A^* = \begin{bmatrix} -\frac{K_1^g + K_1^c}{J_1} & \frac{K_1^c}{J_1} & & & \\ \ddots & \ddots & \ddots & & \\ & \frac{K_{n-1}^c}{J_n} & -\frac{K_n^g + K_n^c + K_{n-1}^c}{J_n} & \frac{K_n^c}{J_n} & \\ & & \ddots & \ddots & \ddots \\ & & & \frac{K_N^c}{J_{N+1}} & -\frac{K_{N+1}^g + K_N^c}{J_{N+1}} \end{bmatrix} \quad (4.17)$$

$$D^* = \frac{\kappa}{\Delta x}\begin{bmatrix} -\frac{1}{J_1} & \frac{1}{J_1} & & & \\ \ddots & \ddots & \ddots & & \\ & \frac{1}{J_n} & -\frac{2}{J_n} & \frac{1}{J_n} & \\ & & \ddots & \ddots & \ddots \\ & & & \frac{1}{J_{N+1}} & -\frac{1}{J_{N+1}} \end{bmatrix}$$

$$B = \begin{bmatrix} [0]_{N+1\times 1} \\ B^* \end{bmatrix} = \begin{bmatrix} [0]_{N+1\times 1} \\ J_1^{-1} \\ [0]_{N\times 1} \end{bmatrix}, \qquad \boldsymbol{u} = \tau_1 \tag{4.18}$$

$$C = \begin{bmatrix} 1 & [0]_{1\times N-1} & 0 & 0 & [0]_{1\times N} \\ 0 & [0]_{1\times N-1} & 0 & 1 & [0]_{1\times N} \\ 0 & [0]_{1\times N-1} & 1 & 0 & 0 \end{bmatrix}, \qquad D = [0] \tag{4.19}$$

This form makes many new analyses of the system possible, including the identification of modes and mode shapes, steady-state solutions, and frequency response that are explored subsequently.

One way I validate the membrane ladder is by comparing it with MacNeal,[51,53] who solved the one-dimensional membrane differential equation rather than using finite elements. Figure 4.3 shows the tip/root frequency response amplitude of a homogenous blade without a tip mass using 100 spanwise elements. This plot is obtained by dividing the transfer functions of root torque to tip pitch by root torque to root pitch.

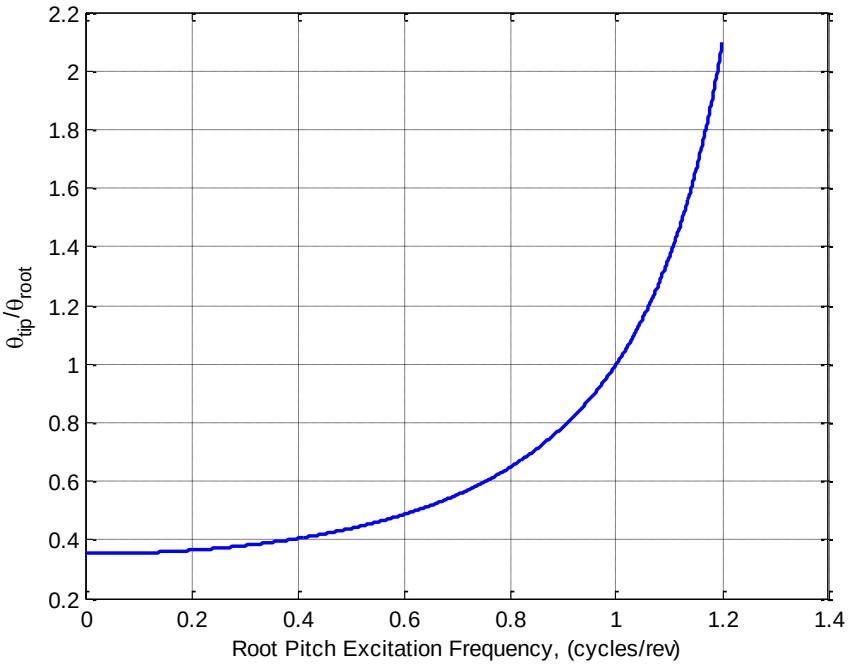

Figure 4.3: Blade tip/root pitch frequency response amplitude

The variation in tip response with frequency arises as the gyroscopic stiffness and inertia torques change their relative magnitudes. During a 1-period cyclic profile, they exactly cancel each other, and the entire blade moves uniformly. The response in Figure 4.3 matches MacNeal's results[53] to a root mean square (RMS) difference of 0.021. MacNeal calculated twist modal frequencies by comparing his linearized one-dimensional membrane equation to Legendre's equation.[53] These correspond to frequencies in the membrane ladder where root torque causes no root motion but blade twist at other locations. That is, modes (poles) in MacNeal's model should correspond to the zeros of the LTI system of Eq. (4.16). Table 4.2 compares his analytical results to the modes of the FEM developed in this section. These mode frequencies match well with 200 elements and approach the analytical solution with additional elements. There is a slight decrease in agreement towards higher frequencies, but this is typical of FEMs.

Table 4.2: MacNeal vs. membrane ladder FEM twist mode frequencies (cycles/rev)

Mode	**MacNeal[53]**	***N* = 200**	Δ	***N* = 1000**	Δ
1	$\sqrt{2} = 1.414$	1.416	0.14%	1.414	0.00%
2	$\sqrt{7} = 2.646$	2.661	0.57%	2.649	0.11%
3	$\sqrt{16} = 4.000$	4.039	0.97%	4.009	0.23%
4	$\sqrt{29} = 5.385$	5.457	1.34%	5.402	0.32%

2. Steady-State Blade Shape and Impedance

As with the tip response in Figure 4.3, the blade mechanical impedance at the blade root (transfer function from motion to effort) varies with frequency as the gyroscopic stiffness and inertia terms vary in relative strength. One may find the blade shape and impedance analytically by looking at the steady-state solution to Eq. (4.16) at the desired frequency. First, assume damping is non-zero, so the transient response decays over time, but that these damping torques

are small enough relative to the stiffness and inertial torques to be neglected. Then, a root torque of cos $\omega_b t$ at a base frequency of ω_b yields the following:

$$u = \tau_1 = \cos \omega_b t\,, \qquad \boldsymbol{\theta} = \boldsymbol{\alpha} \cos \omega_b t \tag{4.20}$$

$$\ddot{\boldsymbol{\theta}} = A^* \boldsymbol{\theta} + B^* \boldsymbol{u} \tag{4.21}$$

$$-\boldsymbol{\alpha}\omega_b^2 \cos \omega_b t = A^* \boldsymbol{\alpha} \cos \omega_b t + B^* \cos \omega_b t \tag{4.22}$$

$$\boldsymbol{\alpha} = -(A^* + \omega_b^2 [I])^{-1} B^* \tag{4.23}$$

where bold indicates vectors defined over the set of spanwise nodes and $[I]$ is an identity matrix.

The spanwise shape vector $\boldsymbol{\alpha}$ is useful for three reasons. First, the root blade impedance is $\alpha_1{}^{-1}$ (Nm/rad). This impedance is zero at the poles of Eq. (4.16) where root motion occurs with zero root torque, and the blade pitches uniformly over the span. The first pole is at 1-period cyclic frequency, so no torque is required to maintain this profile. The impedance is infinite at the zeros of Eq. (4.16), where root torque causes no root motion. Second, multiplying the impedance by the desired pitch yields the steady-state torque required for a given pitch profile. Finally, normalizing $\boldsymbol{\alpha}$ by α_1 reveals the steady-state blade shape along the entire blade, enabling us to choose root reference commands that achieve a desired steady-state blade motion at any other point via:

$$\boldsymbol{\theta_{ss}} = \frac{\boldsymbol{\alpha}}{\alpha_1}\theta_{ref}, \qquad \boldsymbol{\dot{\theta}_{ss}} = \frac{\boldsymbol{\alpha}}{\alpha_1}\dot{\theta}_{ref} \tag{4.24}$$

While pitch rate is not in phase with pitch, the ratio $\boldsymbol{\alpha}$ / α_1 does describes the relationship of root pitch rate to pitch rate along the entire blade.

Figure 4.4 gives the steady-state pitch along the entire span for a collective profile. Again, I use a homogenous blade without lumped masses for comparison against MacNeal. This agrees with MacNeal[51] to an RMS difference of only 0.005, further validating the membrane ladder. Note that the collective twist deflection at the tip is only about 35% of that at the root, termed "wash out", which is characteristic of collective profiles.

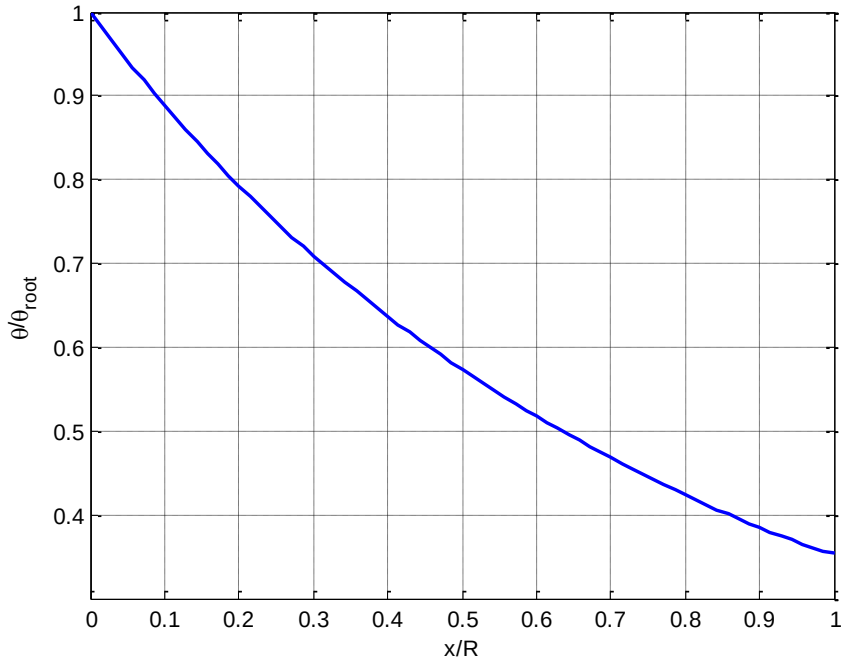

Figure 4.4: Steady-state blade twist for a collective profile

3. Control Law Design and Optimization

As a first pass, I started with an idealized control law for the root motor torque inspired by the root spring-damper design of MacNeal.[53] Crucially, I added feed forward:

$$\tau_1 = K_P(\theta_{ref} - \theta_1) + K_D(\dot{\theta}_{ref} - \dot{\theta}_1) + K_{FF}\theta_{ref} \tag{4.25}$$

The controller has three gains: K_P, K_{FF}, and K_D. I set K_P to the root impedance α_1^{-1} evaluated at the reference/base frequency ω_b. Matching the real part of the controller impedance to the blade impedance (essentially real due to small material damping) should help to minimize reflections at the root motor and maximize energy extraction from traveling waves excited by a change in profile. Setting the feed forward K_{FF} to α_1^{-1} as well provides the pitch profile's proper steady-state torque and eliminates steady-state tracking error. I tune K_D empirically with a simulation of a cyclic profile transient, the most difficult to damp of the three pitch profiles. Figure 4.5 shows the cyclic profile settling times for a variety of rate gains. I define settling time as the point at which the resulting SRP force (averaged over one revolution) changes <10% from one revolution to the next.

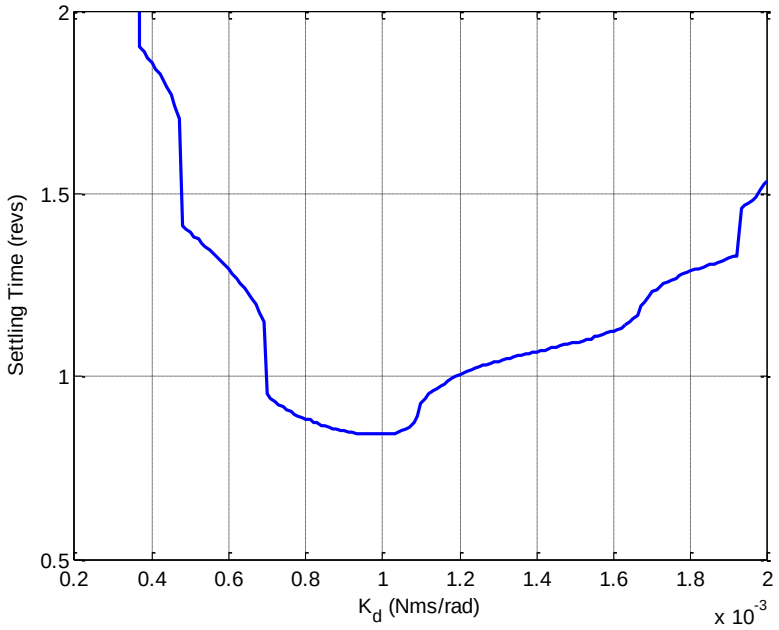

Figure 4.5: Rate gain optimization for cyclic profiles

There is a clear, broad minimum between K_D = 7e−4 to 1.1e−3 Nms/rad, so I set K_D = 9e−4 Nms/rad as the optimal damping constant for the HELIOS design.

An additional design parameter affects the settling time for a collective profile: the rate at which the reference pitch is ramped up to its final amplitude. Figure 4.6 shows the settling time to a collective profile over a spectrum of ramp rates.

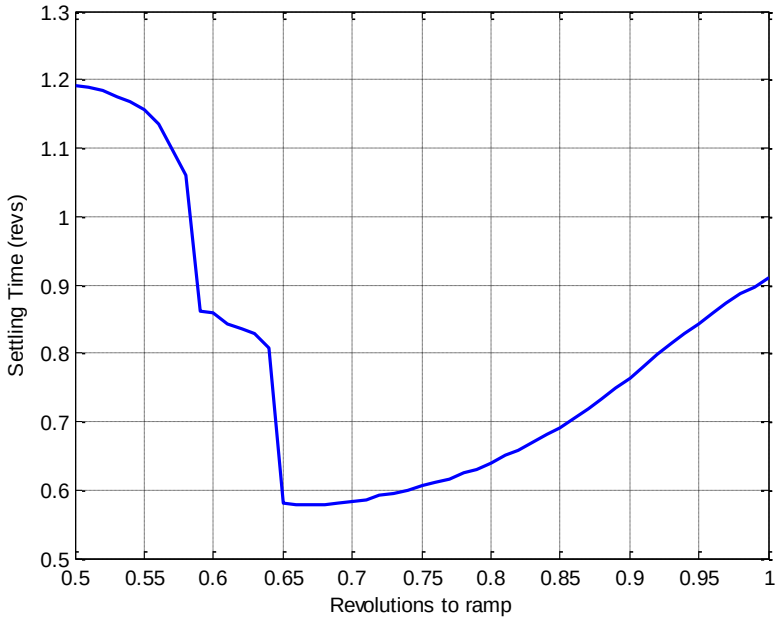

Figure 4.6: Revolutions to ramp optimization for collective profiles

Faster ramp rates disturb the blade more violently, excite more structural modes, and take longer to damp; however, ramp rates that are too slow dominate the settling time. The sharp drop at 0.65 revs to ramp occurs when the first overshoot stays within the 10% settling threshold. I set the ramp rate to 0.75 revs to ramp to avoid this sharp jump.

Figure 4.7 shows the performance of the linear controller for the three pitch profiles. The left subplots show the pitch of the entire blade over time, measured in revolutions. The right subplots compare the root and tip pitch to the reference control signal. In each case, the times marked with the black dashed line indicate the blade's settling time. This root controller performs very well with all three profiles settling in less than one revolution. Additionally, it settles over five times faster than MacNeal's spring-damper system[53] and eliminates steady-state error. MacNeal's system has a steady state error of 25% for collective profiles since there is no feed forward. Nonlinear effects, investigated in Chapter 4.E, will complicate the control problem and increase this settling time, but I will still use a PDFF control law.

This idealized control system makes two simplifying assumptions related to stability: no material damping and infinite controller bandwidth. Any real control system has several characteristics that introduce phase loss in practical implementation. For example, a pitch actuator has a finite bandwidth. Similarly, a differentiator must have a high-frequency gain limit typically achieved with a low-pass filter. Furthermore, a digital controller would apply sampling and an anti-alias filter. All of these aspects add phase loss relative to the baseline controller that is unavoidable in practice. This phase loss destabilizes the high frequency modes unless there is sufficient material damping. Such material damping must be experimentally derived but is expected to be very small. When determined, its value will establish the control system bandwidth (due to the bandwidth-limiting effects above) required for stability based on the analysis below.

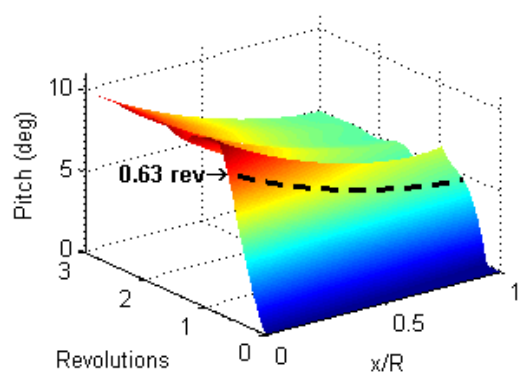

a) 10° collective profile full blade pitch

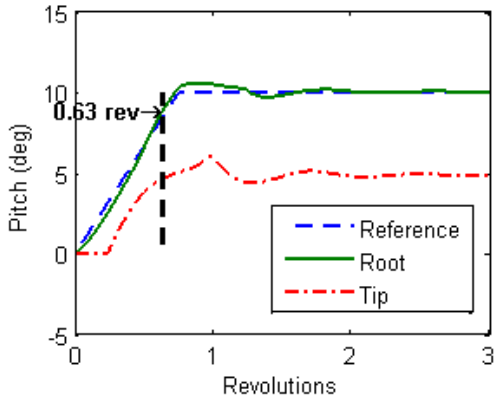

b) 10° collective profile pitch at the root and tip

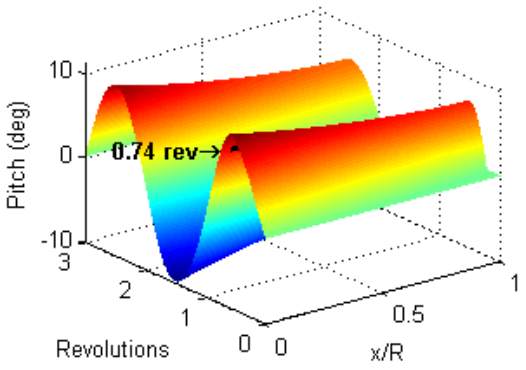

c) 10° half-p profile full blade pitch

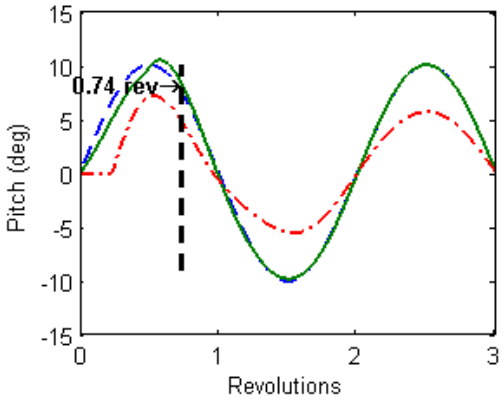

d) 10° half-p profile pitch at the root and tip

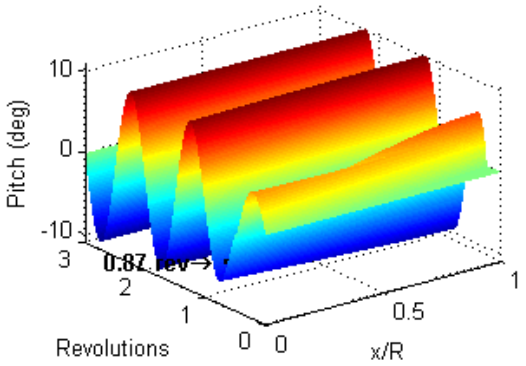

e) 10° cyclic profile full blade pitch

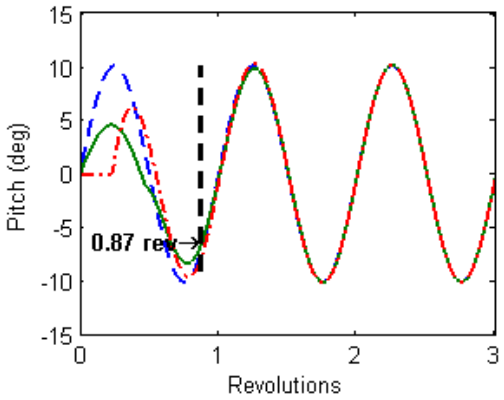

f) 10° cyclic profile pitch at the root and tip

Figure 4.7: Baseline root controller performance for three blade profiles of interest

4. Frequency Response and Stability Analysis

To understand the relationship between control system bandwidth and material damping, I convert the plant of Eq. (4.16) into the frequency domain using Matlab's `bode` function. Figure 4.8 shows the plant pitch response to root torque with a small amount of material damping. This and all other plots in this section use N = 400 blade elements, which is near the maximum

before Matlab returns an ill-conditioned matrix error. This gives a useable frequency range up to 350 cycles/rev, where frequency response was independent of element refinement.

The first mode is a rigid body oscillation, so there is no blade deformation to cause damping. Given κ = 2e−6 Nm^{2}s/rad, the second mode has a damping ratio of 0.002%, which increases linearly with frequency, reaching 0.11% by 100 cycles/rev. The damping coefficient also relates linearly to damping ratio. The tip/root motion does not have any zeros, characteristic of non-colocated transfer functions with a free boundary condition. This would cause large amounts of phase loss in a loop feeding back tip position to root torque, making it very difficult for such non-colocated loops to achieve stability.

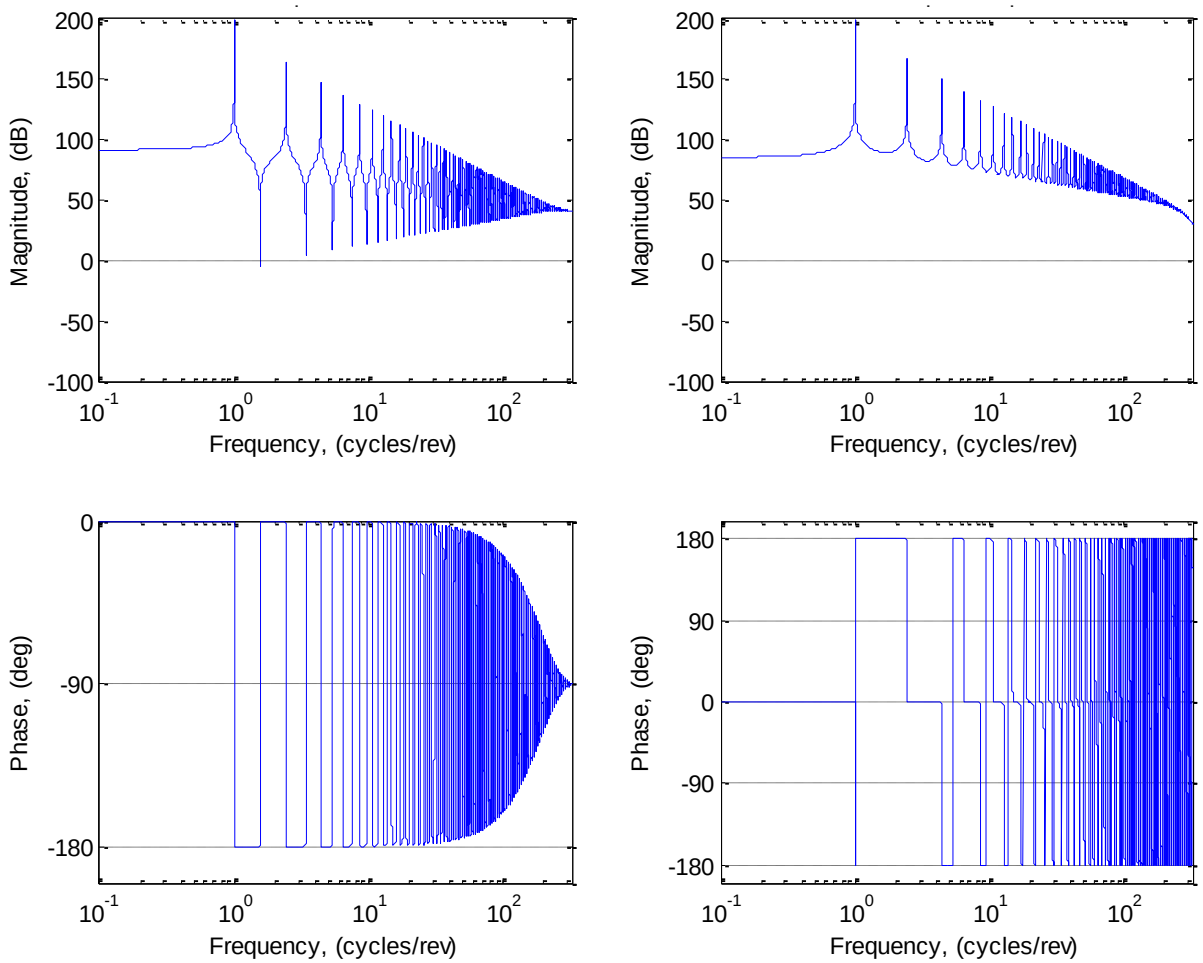

a) Root torque to root pitch Bode plot **b) Root torque to tip pitch Bode plot**

Figure 4.8: Plant response Bode plots with κ = 2e−6 Nm^{2}s/rad

The following examines the loop gain in the root control system to explain the impact on stability and the closed-loop response of finite control system bandwidth and material damping. Figure 4.9 is a block diagram of this more realistic control system with the "lag" block characterizing the dominant control system bandwidth of *w* (rad/s), typically dominated by the actuator bandwidth. It uses a simple proportional/derivative (PD) feedback of root pitch to control root torque using a torque source motor at the blade root. I use the baseline proportional gain K_P for the collective profile, as this is the highest gain and, therefore, most likely to cause instability. I also ignore the feed forward because it does not affect stability.

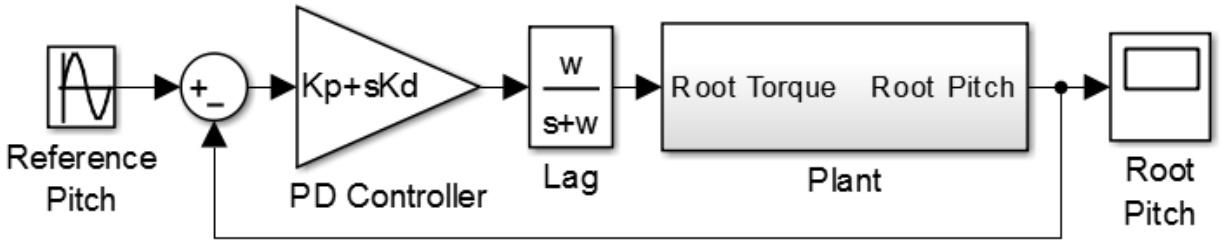

Figure 4.9: Block diagram of the realistic root pitch controller

Figure 4.10 shows the frequency response analysis of this more realistic system. Bode plots of the negative loop gain are on the left (a) and (c), while the right subplots are the Nyquist plots of the negative loop gain (b) and the magnitude of the closed-loop tracking frequency response (d). This case uses a control system bandwidth *w* corresponding to 30 cycles/rev and a material damping of 2e−6 Nm^2s/rad (the same as Figure 4.8). This damping is sufficiently small that it does not visibly affect the response during blade dynamics simulations, and the bandwidth *w* is one decade below the useful frequency range of the plant model. This controller bandwidth and damping level yield a stable system with about 40° of phase margin and root peaking less than 5 dB. The omitted feed forward signal would provide good tracking at root excitation frequencies less than 1.2 cycles/rev. The peaking at the tip reaches around 10 dB—not ideal, but this has a small effect in practice because of the low excitation of higher frequencies.

Note that the additional phase loss in the realistic control system causes the modal loops in the Nyquist plot to rotate clockwise at high frequencies. Without the pinch-off in magnitude of the structural modes at high frequencies due to material damping, these loops would eventually encircle the critical point and destabilize the system. No amount of control system damping (which inserts phase lead) can substitute for this material damping, since such phase lead must eventually disappear at high frequencies for it to be physically implementable. The control system bandwidth used in Figure 4.10 is 30 times the first structural mode frequency. The low rotation rate (1 RPM) makes even this relatively high bandwidth a physically reasonable 0.5 Hz. The material damping value is unknown, however, and much higher bandwidths may be required.

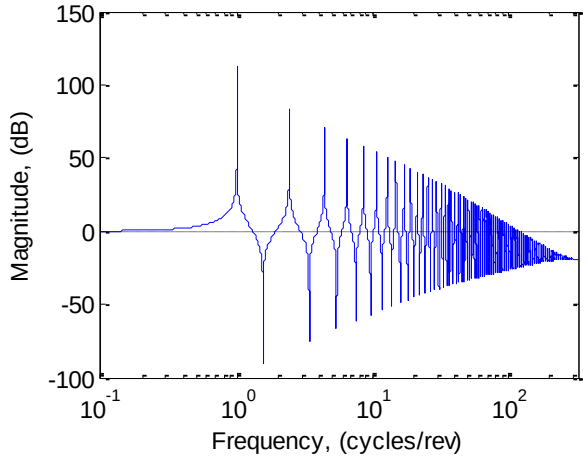

a) Bode magnitude of root pitch loop gain

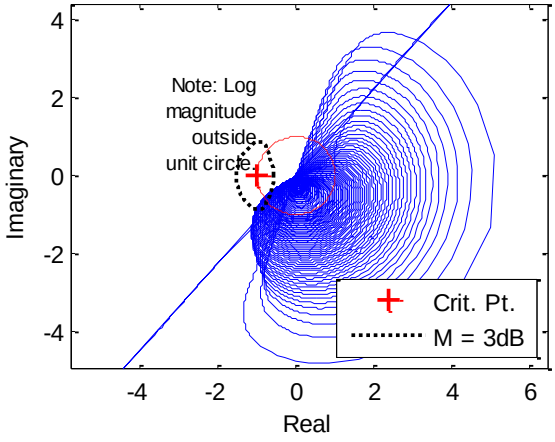

b) Nyquist root pitch loop gain.

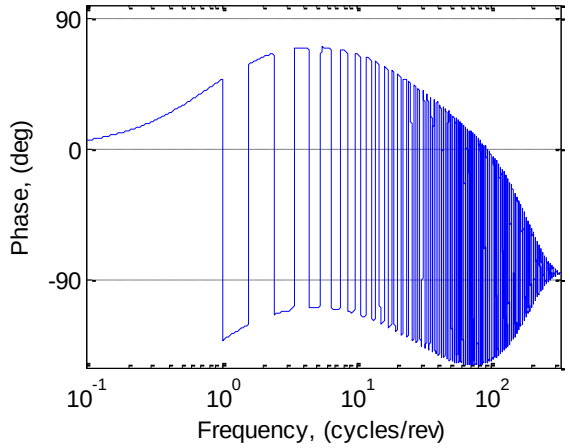

c) Bode phase of root pitch loop gain

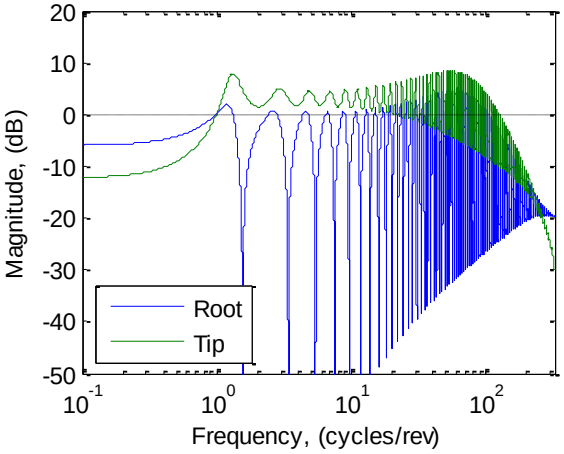

d) Closed-loop tracking of root and tip

Figure 4.10: Closed-loop response with w = 30 cycles/rev (0.5 Hz) and κ = 2e−6 Nm^{2}s/rad

The next study looks at the trade-off between material damping and controller bandwidth to determine their combined effect on stability and the magnitude of the blade's response. Figure 4.11 shows contours of the closed loop response peaking for a range of material damping and control system bandwidths. Dots show the grid of data points for which I conducted the above stability and response analysis with black dots being closed-loop stable, and red dots being unstable.

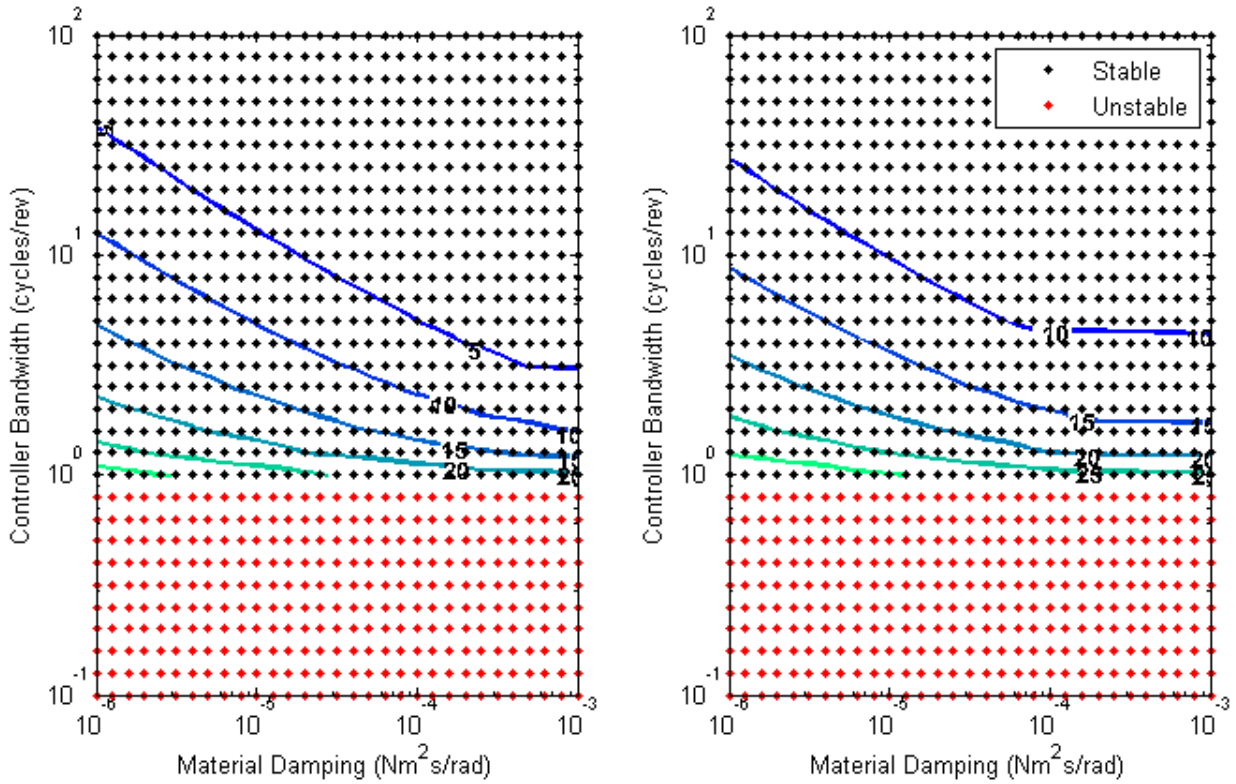

a) Maximum root response (dB) **b) Maximum tip response (dB)**

Figure 4.11: Contours of closed-loop peaking response (dB) vs. material damping and controller bandwidth

In all cases of damping examined in Figure 4.11, the controller bandwidth must be at least 1 cycle/rev (0.0167 Hz or the first mode) to avoid instability. The first mode represents a rigid-body oscillation in this free-free system, so there is no twist bending of this mode, and therefore no material damping. Consequently, this mode must be phase stabilized. This requires that the additional phase lag due to control system bandwidth is less than about 45° at the first mode

frequency to obtain any phase margin, i.e., the control system bandwidth must be no less than the first mode frequency (1 cycle/rev). The ideal PD controller with the optimum damping designed in Chapter 4.B.3 provides 45° phase margin at the first mode, so the lag introduced by a low-pass filter must have a bandwidth of at least the first mode frequency to maintain stability.

The closed-loop performance relationship of damping and bandwidth is nearly linear on a log-log scale for damping values below 1e–4 Nm^2/rad. Once experiments determine material damping levels, a designer could then refer to Figure 4.11 for the required control system bandwidth and allocate acceptable phase loss from the various sources. One can see from the slopes of these contours that the system is relatively insensitive to material damping; bandwidth is much more important. This is comforting since designers have more control over bandwidth than material damping. Additionally, the tip peaking is always higher than the root because the tip is unconstrained. A bandwidth of 30 cycles/rev (0.5 Hz) minimizes response peaking for reasonable damping levels, and higher bandwidths provide little benefit.

C. Blade Tip Control by Local Reflectivity Modulation

The results using root control alone provide an encouraging picture of the feasibility of blade twist control for heliogyros; however, one caveat is that they neglect the coupling between twist, flap, and lead-lag blade motions. Once these motions are included, the damping and stability issue will become more complex. Furthermore, the blade root motor is assumed to be a torque source, but the torques required are on the order of 1 μNm. Friction forces would likely overwhelm this torque in a conventional electromagnetic motor. Therefore, it may be more practical to use a position source motor at the root. These factors may necessitate active damping at the blade tip.

The Ultrasail project proposed a method of blade tip control using small thrusters, [12,13] but this requires propellant, which negates the primary advantage of solar sails. JAXA pioneered an

innovative reflectivity control approach to vary solar radiation pressure acting on the sail membrane of their IKAROS solar sail.[24] They applied a system of thin-film LCDs which transition from diffuse to specular reflection when powered. I refer to this concept more broadly as a reflectivity control device (RCD), since other materials such as electrochromics[63] may prove more effective. RCDs have several advantages as tip actuators: they are flexible, can be rolled up with the blade, require no propellant, use little power, and are solid state. In fact, RCDs could be combined with thin-film photovoltaic (PV) panels to make a self-contained system.

This subchapter examines the effectiveness of the JAXA reflectivity control approach for damping torsional oscillations of a heliogyro blade. I evaluate a system of RCDs distributed near the blade tip with a pitch rate feedback control law. I evaluate this system's settling time performance and closed loop stability in the presence of unavoidable control system phase loss. I trade different RCD properties and feedback sensor configurations to see if such a system is advisable as a tip actuator.

1. Incorporating RCDs into the Membrane Ladder FEM

Figure 4.12 shows the generalized blade dimensions and RCD geometry. There are two RCD regions at the leading and trailing edges over an area at the blade tip. The difference in solar radiation pressure between the on/off specular and diffuse reflectivity states of the RCDs creates a torque on the blade. The RCD configuration is fully defined by any two of the following three parameters: c_{RCD}, R_{RCD}, or f_{RCD} (the fraction of the blade area that is RCD). The "inboard" portion of the blade ($x < R_{RCD}$) has no RCD elements. The "outboard" portion ($x \geq R_{RCD}$) consists of a combination of thin film solar cells and RCD. The RCD is broken into independently controllable segment pairs. The outboard center area contains the PV cells to power the RCDs, and I assign them a c_{RCD} of 0.1 m of the full 0.75 m chord.

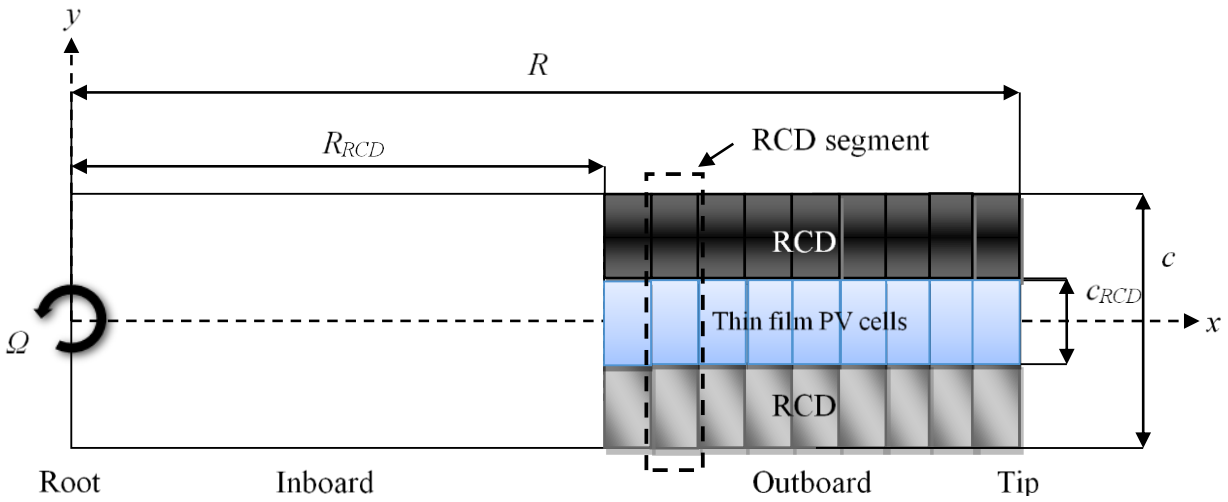

Figure 4.12: Generalized blade RCD configuration

RCD elements along the blade span are divided into a number of leading edge and trailing edge pairs. Segments are nominally 2.5 m spanwise, with the number of segments varying depending on RCD areal fraction. I assume the local solar-radiation-pressure induced torque is continuously variable between the minimum and maximum value, which could be accomplished with pulse width modulation of the RCD switching. For linear stability analysis, I incorporate RCD control into the state space system of Eq. (4.16):

$$\dot{\boldsymbol{X}} = \begin{bmatrix} \dot{\boldsymbol{\theta}} \\ \ddot{\boldsymbol{\theta}} \end{bmatrix} = A\boldsymbol{X} + B_{RCD}\boldsymbol{u_{RCD}} + B_{root}\boldsymbol{u_{root}}, \qquad \boldsymbol{Y} = \begin{bmatrix} \theta_1 \\ \dot{\theta}_1 \\ \theta_{N+1} \end{bmatrix} = C\boldsymbol{X} + Du \tag{4.26}$$

$$B_{RCD} = \begin{bmatrix} 0 & \dots & 0 \\ \vdots & \ddots & \vdots \\ 0 & \dots & 0 \\ J_{nRCD}^{-1} & & \\ & \ddots & \\ & & J_{N+1}^{-1} \end{bmatrix}_{N+1\times N-nRCD}, \qquad \boldsymbol{u_{RCD}} = \begin{bmatrix} \tau_{nRCD} \\ \vdots \\ \tau_{N+1} \end{bmatrix} \tag{4.27}$$

$$B_{root} = \begin{bmatrix} [0]_{N+1\times 1} \\ B^* \end{bmatrix} = \begin{bmatrix} [0]_{N+1\times 1} \\ J_1^{-1} \\ [0]_{N\times 1} \end{bmatrix}, \qquad \boldsymbol{u_{root}} = \tau_1 \tag{4.28}$$

where *nRCD* is the index of the first outboard rung, and the *A*, *C*, and *D* matrices of Eqs. (4.17) & (4.19) are unchanged. This form splits out the root and RCD control systems, as I will treat them separately.

2. RCD Control System

I evaluate three RCD configurations representing different technology levels. The first is based upon IKAROS' flight-proven LCD systems.[24,57] These LCDs are on a flexible substrate and have a density similar to that of the sail but are approximately 40 μm or 16 times thicker than HELIOS' sail membrane. The second is an advanced blade using RCD elements with twice the control moment effectiveness and half the thickness of those flown on IKAROS. I base these upon existing reflectivity control materials without space flight heritage and at a low technology readiness level (TRL); for example, an electrochromic switchable mirror foil.63 The third is an ideal RCD using parameters that illustrate this system's feasible performance limits. Table 4.3 gives the parameters for all three RCD systems. I assign the thin film solar cells along the mid-chord the same density and thickness as the RCD material since their construction is similar.

Table 4.3: Three RCD parameter sets analyzed

	IKAROS	Advanced	Ideal
ON/OFF change in specular reflectivity (ΔC_s)	0.3	0.6	0.8
ON/OFF change in diffuse reflectivity (ΔC_d)	–0.3	–0.6	–0.8
RCD thickness (h_{RCD})	40μm	20μm	2.5μm
RCD density (ρ_{RCD})	3 g/cm^3	3 g/cm^3	3 g/cm^3

To find the control torque generated by opposing RCDs, we must incorporate a more complex reflection force model that includes diffuse and specular terms:[24]

$$\boldsymbol{F_n} = -PA_n(\boldsymbol{n_n}\cdot\boldsymbol{s})\left[(1-C_s)\boldsymbol{s} + \left(2C_s(\boldsymbol{n_n}\cdot\boldsymbol{s}) + B_f C_d\right)\boldsymbol{n_n}\right] \tag{4.29}$$

This assumes emission occurs in all directions and generates no net force. The Lambertian coefficient B_f is 2/3 for uniform diffuse reflection.[24] Taking the component normal to the blade element and subtracting the on/off states yields the differential normal pressure:

$$\Delta P_n = P \cos\theta_n \left[\Delta C_s \cos\theta_n + \frac{2}{3}\Delta C_d\right] \tag{4.30}$$

This assumes the heliogyro is pointing directly at the sun; otherwise, the angle of solar incidence replaces pitch θ_n. The maximum pitching moment per blade element due to a pressure is:[52]

$$\tau_{n,max} = \Delta x \int_{-c/2}^{c/2} P_n(y) y \, dy = \Delta x \frac{\Delta P_n}{8}(c^2 - c_s^2) \tag{4.31}$$

which sets the differential pressure generated by the area with PV cells to zero since its reflectivity is constant and blade camber is assumed zero.

The control law is a rate tracker with limited control authority:

$$\tau_{n,req} = K_{RCD}\Delta x \left(\frac{\alpha_n}{\alpha_1}\dot{\theta}_{ref} - \dot{\theta}_n\right) \tag{4.32}$$

$$\tau_n = \begin{cases} \tau_{n,req} & \text{for } \tau_{n,req} < \tau_{n,max} \\ \text{sign}(\tau_{n,req})\, \tau_{n,max} & \text{for } \tau_{n,req} \geq \tau_{n,max} \end{cases} \tag{4.33}$$

The reference pitch rate at the *n*th rung is a function of the reference pitch rate at the root scaled by the blade shape factor $\boldsymbol{\alpha}$ found using the process of Chapter 4.B.2. I parametrically optimize the gain K_{RCD} to minimize settling time. In this case, the optimum K_{RCD} is 1e−3 N/rad. Increasing controller gain provides little difference in performance since the controller saturates.

I evaluate two sensor configurations: distributed sensing at each blade rung and a single sensor at the tip. For the RCD parameter optimization in Chapter 4.C.3, I assume a position source at the root and distributed sensing. This makes the RCD the sole source of blade damping to isolate its performance from root control, and the distributed sensors ensure stability. I will show in Chapter 4.C.4 that single sensor configurations introduce instability in closed loop due to the

non-colocation of the single sensor with a distributed actuator. In that chapter, I include the feedback control of a torque-source root motor with finite bandwidth from Chapter 4.B.4 to stabilize the complete system in closed-loop. In both cases, I assume a 100 g tip mass ($1/6^{th}$ the nominal blade mass) representing the mass of the control system electronics.

3. RCD Parameter Optimization

Analysis of RCD material properties provides a baseline for future materials research. Increasing the difference in RCD reflectivity between the on and off states increases the differential pressure and, therefore, the control moment available to the system. Sail thickness in general is critical to sail mass and overall acceleration, so the ideal RCD thickness would be close to that of the sail. Thicker RCDs also increase mass moment of inertia making it more difficult to damp twisting. IKAROS' RCDs are approximately 16 times thicker than the 2.5 μm sail material. Figure 4.13 shows how the combination of these two properties affected settling time.

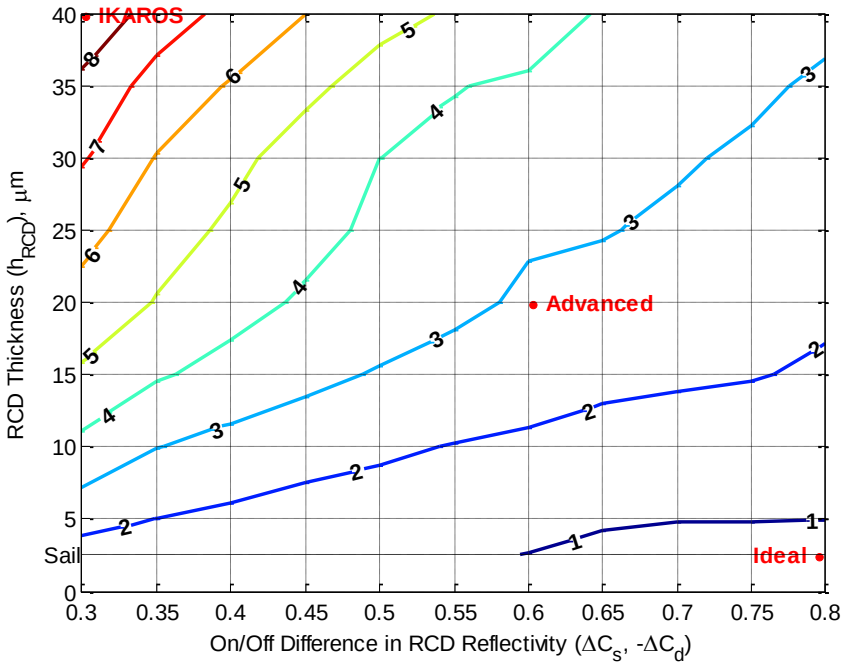

Figure 4.13: Contours of cyclic profile settling time (revs) for a range of RCD properties with 10% f_{RCD}

Variations in either parameter generated significant improvements in settling time. Doubling of ΔC_s & $-\Delta C_d$ yielded a 50% improvement in settling time, regardless of thickness. Halving the thickness only lowered the settling time by 35%, regardless of ΔC_s & $-\Delta C_d$. Improving both factors at once from IKAROS to Advanced yielded a 67% reduction, which is the product of their individual contributions. If settling time were the sole operational concern, increasing the on/off difference in RCD reflectivity would provide the greatest benefit; however, h_{RCD} greatly affects mass and characteristic acceleration, the primary performance metric for solar sails.

The fraction of the blade's area covered in RCD f_{RCD} has a direct impact on the sail's mass, average reflectivity, control authority, and settling time. Advanced RCD materials could meet settling time requirements with a smaller RCD. Figure 4.14 shows how the settling time varied with f_{RCD} for each of the three notional RCD materials. I set a settling time requirement of four revolutions, which is four minutes for HELIOS and fast enough to change the pitch profile many times per orbit in LEO.

The Advanced RCD could achieve the nominal LEO mission settling time requirement with only 5% coverage, and the ideal with only 1%. IKAROS RCDs, on the other hand, are incapable of meeting LEO settling time requirements regardless of size. At 25%, the IKAROS RCDs would more than double the heliogyro's mass, making them impractical. An IKAROS-type RCD would only be effective in at higher altitude orbits, where slower maneuvers are acceptable. The settling time in each case is asymptotic, so sizes larger than 10% should be avoided for mass and complexity reasons. The slight irregularity of settling time determination evident in the plots arose because RCD authority varies with pitch angle, so they do not damp the blade in a precisely exponential fashion.

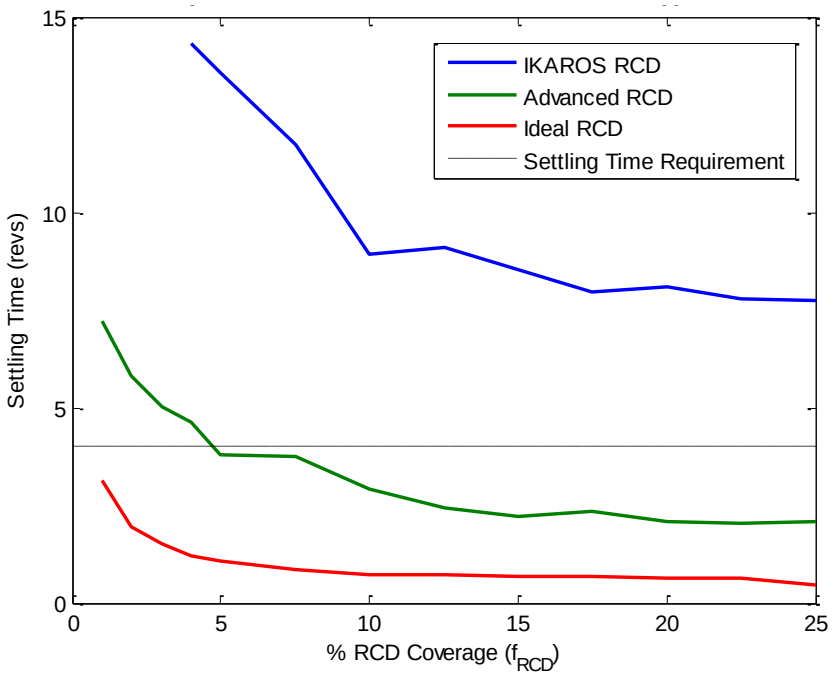

Figure 4.14: Settling time for different RCD size and material properties

Figures 4.13 and 4.14 illustrate how to optimize different RCD systems to meet settling time requirements. In practice, the more important concern is how RCD parameter variation flows down to the heliogyro's characteristic acceleration a^*. All three of the RCD parameters examined affect sail mass or reflectivity and thus characteristic acceleration. Since the RCDs are constantly switching reflectivity states about an average value, variations in ΔC_s & $-\Delta C_d$ do not significantly affect overall RCD reflectivity. The principal effect, therefore, is the RCD's contribution to mass. Improvements in ΔC_s & $-\Delta C_d$ do indirectly affect mass by allowing for a smaller size RCD that still meets settling time requirements.

In order to guide future research in RCD materials, it is important to know which parameter has the greatest effect on overall heliogyro performance: ΔC_s & $-\Delta C_d$ or h_{RCD}. Figure 4.15a varies ΔC_s & $-\Delta C_d$ and f_{RCD} to determine combinations meeting the settling time requirement of four revolutions. Figure 4.15b shows the plot of the spacecraft mass and characteristic acceleration for those combinations. Both plots use a constant-thickness RCD (h_{RCD} = 20 μm). The f_{RCD} of the 4-

revolution settling time contour is used to calculate mass and characteristic acceleration. Note that the x-axis is reversed to put low-mass options towards the origin. Doubling the reflectivity difference from IKAROS RCD value (0.3) to the advanced RCD value (0.6) improves characteristic acceleration by 63%. This shows how f_{RCD} optimization connects increased RCD performance to gains in characteristic acceleration. Further improvement to the technology's practical limit (0.8) was only a 7% additional benefit in a^*.

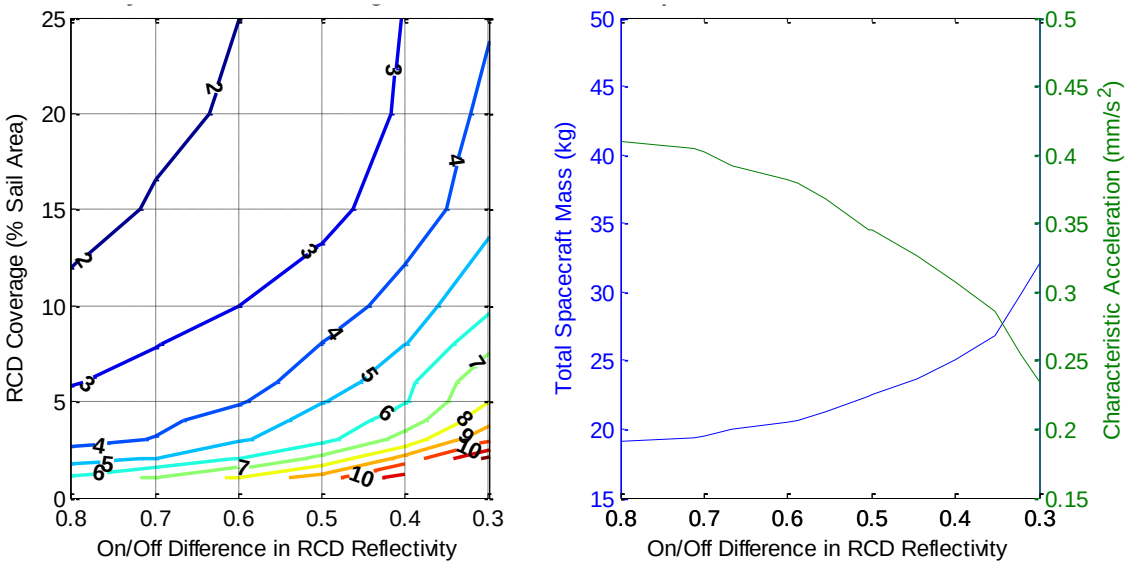

a) ΔC_s & $-\Delta C_d$ and f_{RCD} vs. settling time in revs **b) Mass and a^* with RCD optimized for ΔC_s & $-\Delta C_d$**

Figure 4.15: ΔC_s & $-\Delta C_d$ effect on cyclic profile settling time, optimized f_{RCD}, solar sail total mass and a^*

Figure 4.16 illustrates performance trends for variations in RCD thickness, which has a more direct effect on mass and characteristic acceleration. As with reflectivity, there are substantial initial gains that taper off. Halving in thickness from IKAROS values (40 to 20 μm) improves a^* by 127%, which was twice that realized by doubling reflectivity performance. Further reducing RCD thickness to the sail thickness (from 20 to 2.5 μm) resulted in additional gains in $a^*$of only 17%. Note that doubling the IKAROS ΔC_s & $-\Delta C_d$, *and* halving the IKAROS h_{RCD} (the advanced configuration) could increase a^* by over 200%. This would permit a useful solid-state RCD-based blade damping system for LEO maneuvering applications. Ultimately, settling time

will need to be traded against characteristic acceleration to find an acceptable mission systems design.

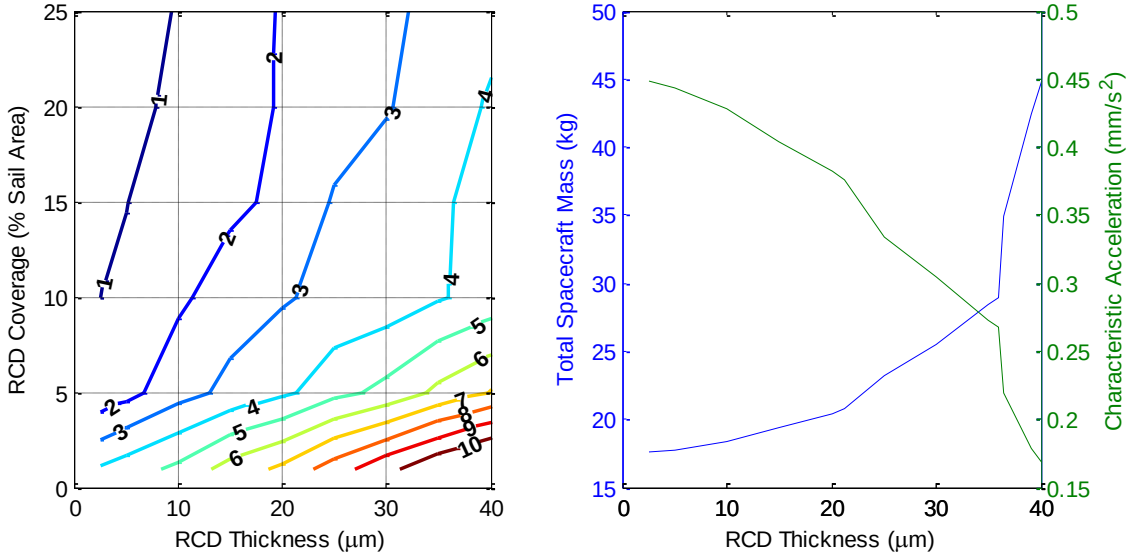

a) h_{RCD} and f_{RCD} vs. settling time in revs **b) Mass and a^* with RCD optimized for h_{RCD}**

Figure 4.16: h_{RCD} effect on cyclic profile settling time, optimized f_{RCD}, solar sail total mass and a^*

Figure 4.17 examines how RCD area fraction f_{RCD} and thickness h_{RCD} affect total heliogyro mass and characteristic acceleration. Dots indicate the optimized parameters for the three RCD systems, and Table 4.4 summarizes these results. Lowering RCD thickness moves down and to the left towards the highest accelerations, while lowering ΔC_s, ΔC_d indirectly moves to the left by allowing for smaller RCDs. These results indicate that improved RCD material systems beyond the existing IKAROS baseline would pay significant performance dividends. Furthermore, IKAROS RCDs are not sufficient for agile heliogyro maneuvering in LEO. Reducing RCD thickness would have the most direct and sizeable benefit to overall heliogyro maneuvering and characteristic acceleration performance.

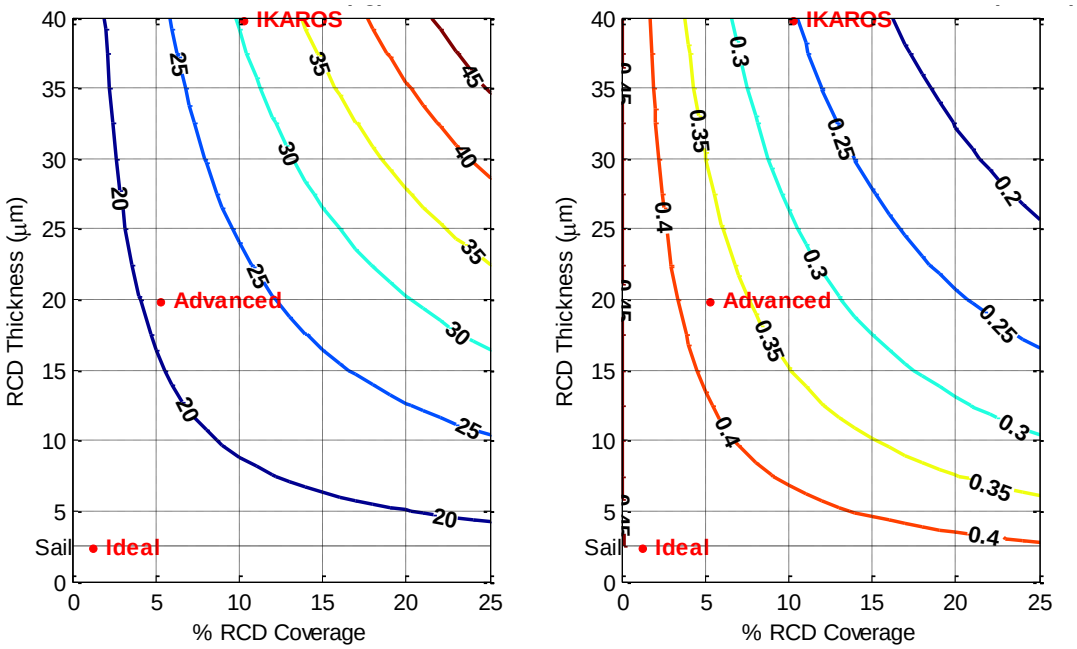

a) f_{RCD} and h_{RCD} vs. total spacecraft mass (kg) **b) f_{RCD} and h_{RCD} vs. a^* (mm/s^2)**

Figure 4.17: Total heliogyro performance variation by RCD size and thickness

Table 4.4 Optimization summary for three RCD parameter sets on the HELIOS baseline

Parameter	IKAROS	Advanced	Ideal
RCD coverage f_{RCD}	10%	5%	1%
Total heliogyro mass m	30 kg	21 kg	18 kg
Characteristic acceleration a^*	0.26 mm/s^2	0.38 mm/s^2	0.45 mm/s^2

4. Closed Loop Linear Stability Analysis

The previous section's analysis assumes a distributed sensing system along the outboard part of the blade for RCD pitch rate feedback. Such a system may be impractical, so this section will look at the problems of using a single pitch sensor at the blade tip. The chief concern is the potential instability arising from the tip sensor not being colocated with portions of the tip RCD actuator. Therefore, I continue to use the linearized EOM to perform classical stability analysis. The previous section also assumes a position source root motor, but this section incorporates the PD control law on a torque source root motor of Chapter 4.B.3. As with Chapter 4.B.4, I omit the feed forward since this term does not affect stability. Figure 4.18 is a block diagram of both loops of the complete control system from Eqs. (4.25) & (4.32). I retain the lag block representing the

root control system bandwidth, but I assume the solid-state RCDs have a sufficiently quick response and high bandwidth relative to the root motor that we can ignore their phase loss.

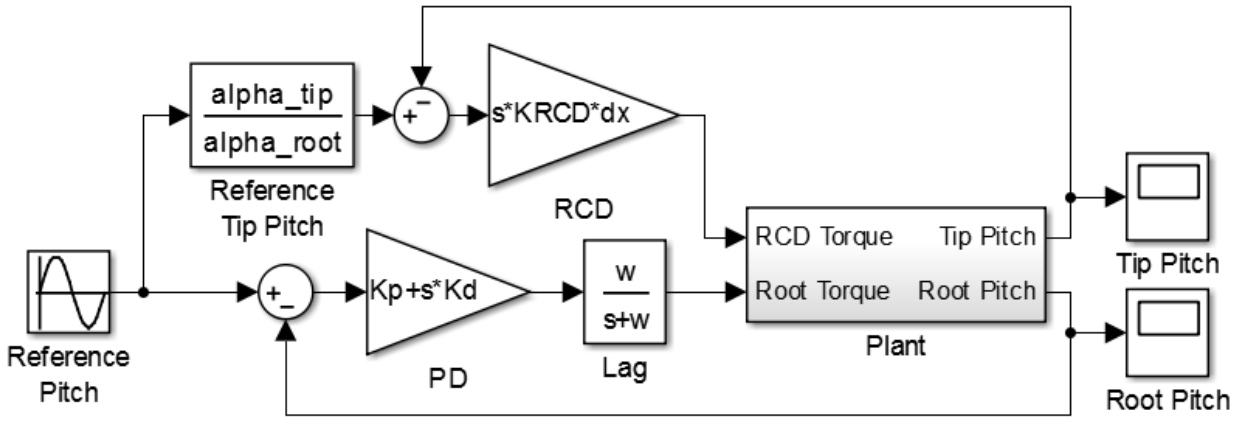

Figure 4.18: Block diagram of the root and RCD control systems

To isolate the RCD's effect on root control, I roll the RCD control loop into the plant dynamics. For stability analysis, I assume that the RCD is never saturated. Substitute the RCD control law of Eq. (4.32) into the state space system of Eq. (4.26), assuming no RCD clipping:

$$\dot{\boldsymbol{X}} = A\boldsymbol{X} + B_{root}\boldsymbol{u_{root}} + B_{RCD}K_{RCD}\Delta x\left(\frac{\alpha_{N+1}}{\alpha_1}\dot{\theta}_{ref} - \dot{\theta}_{N+1}\right) \tag{4.34}$$

$$\dot{\boldsymbol{X}} = (A - B_{RCD}[[0]_{1\times 2N+1} \quad 1]K_{RCD}\Delta x)\boldsymbol{X} + \left[B_{root} \quad B_{RCD}K_{RCD}\Delta x\frac{\alpha_{N+1}}{\alpha_1}\right]\begin{bmatrix}\tau_1\\ \dot{\theta}_{ref}\end{bmatrix} \tag{4.35}$$

$$\dot{\boldsymbol{X}} = \bar{A}\boldsymbol{X} + \bar{B}\bar{\boldsymbol{u}} \tag{4.36}$$

These equations also implement the single tip sensor by only feeding back the tip (rung N+1) pitch rate. $\bar{A}$ and $\bar{B}$ represent the new plant that I subject to the same control analysis of the root loop done in Chapter 4.B.4. Keep in mind that the reference root rate $\dot{\theta}_{ref}$ = 0 for the collective profile under analysis. I set K_{RCD} = 1e−5 Ns/rad since this value results in very little RCD torque clipping in the dynamic simulation, and the linear stability analysis cannot accommodate clipping. I use the Advanced RCD from Table 4.3 and the optimized 5% coverage from Table 4.4. The IKAROS system would be too massive, and the Ideal system is far-term.

The response in Figure 4.19 uses the same material damping and controller bandwidth as in Chapter 4.B.4. It also uses a root controller proportional gain K_P = 4.21e−5 Nm/rad and derivative gain K_D 9e−4 Nms/rad, optimized for collective per the procedure of Chapter 4.B.3. This plot reveals several key benefits and drawbacks to this RCD system when compared to the no-RCD system of Figure 4.10. First, it significantly enhances damping of modes <10 cycles/rev, those that will contain the most energy when the system is disturbed. Second, the tip response rolls off in amplitude 25% sooner. Third, the modes shift up in frequency. This arises from the extra RCD weight at the tip that increases blade tension. Unfortunately, there are also four Nyquist encirclements of the critical point between 10 to 40 cycles/rev. Careful examination reveals that these are counter-clockwise encirclements, and therefore not destabilizing as long as the inner, RCD feedback loop has the same number of pole pairs in the right-half of the complex plane.

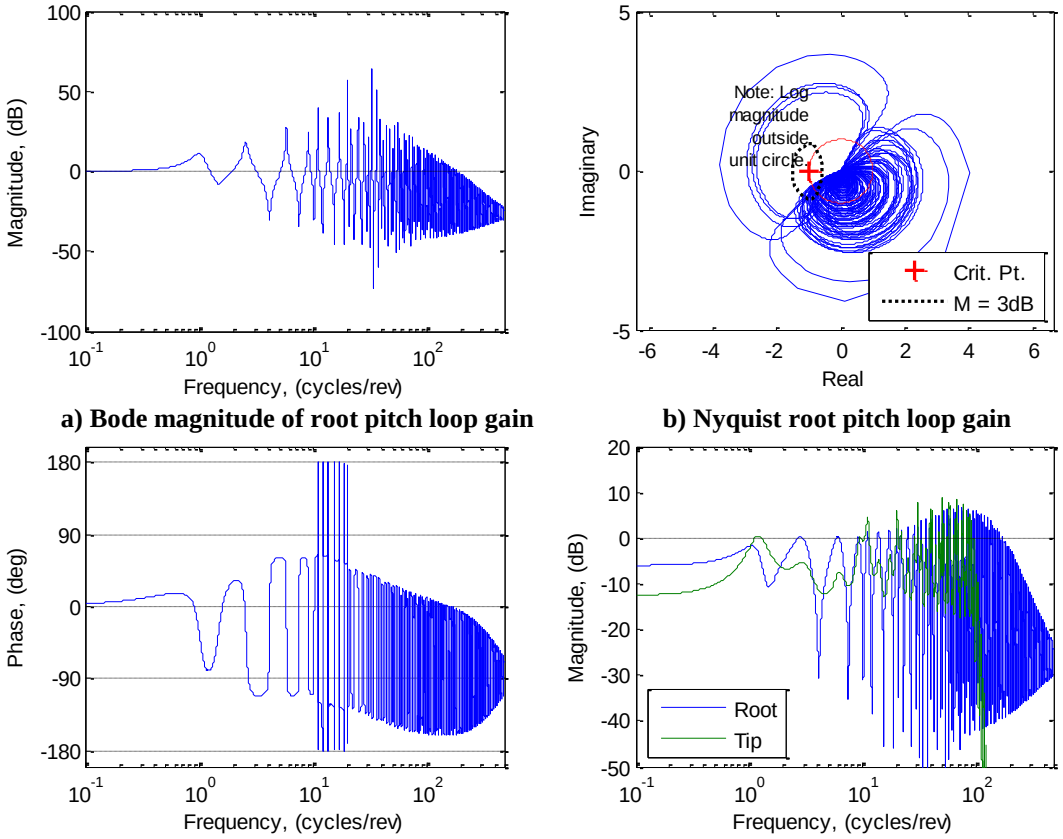

a) Bode magnitude of root pitch loop gain

b) Nyquist root pitch loop gain

c) Bode phase of root pitch loop gain

d) Closed-loop tracking of root and tip

Figure 4.19: Closed-loop response with w = 30 cycles/rev (0.5 Hz), κ = 2e−6 Nm^{2}s/rad, and f_{RCD} = 5%

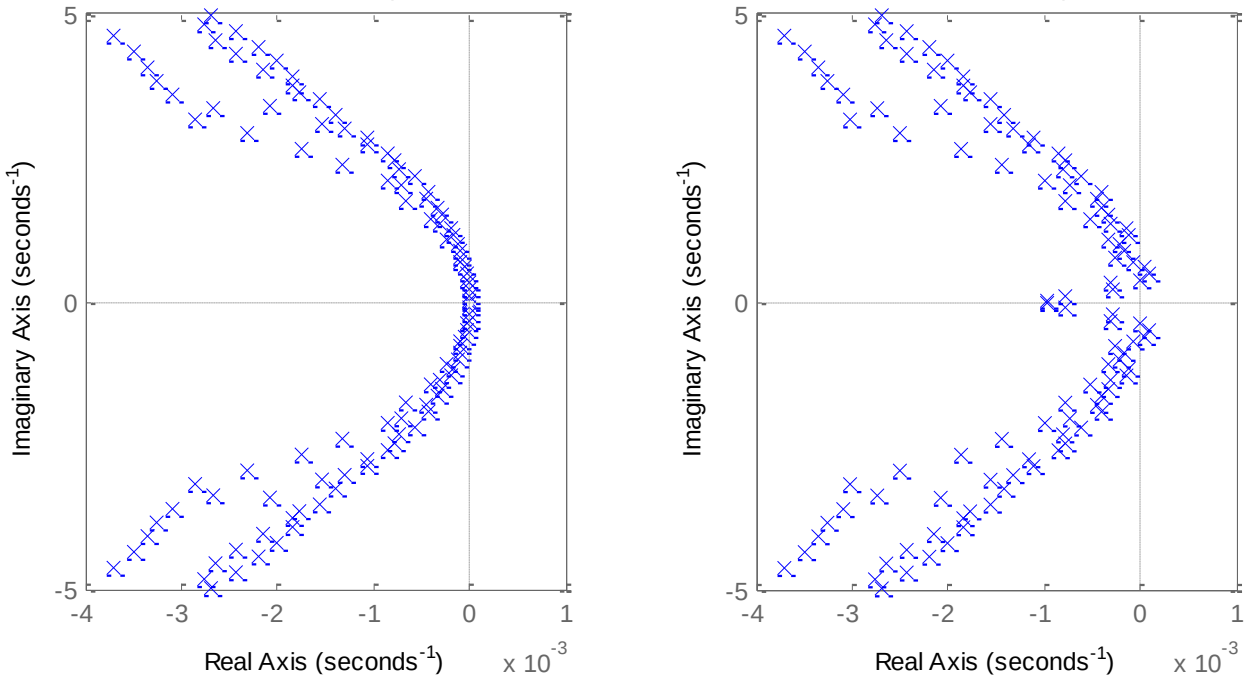

b) K_{RCD} = 0 (controller off) **b) K_{RCD} = 1e−5 (controller on)**

Figure 4.20: Pole-zero maps showing the effect of RCD controller with κ = 2e−6 Nm^{2}s/rad and f_{RCD} = 5%

Figure 4.20 is a zoomed view comparing the pole-zero maps for the blade with the RCD controller on and off. Again, the RCD system increases damping of the first four modes from a) to b) as their real parts shift more negative. Unfortunately, it also shifts the real parts of the next three pole pairs into the right-half plane. These three pole pairs account for the three counter-clockwise encirclements of Figure 4.19b, and the complete system is actually closed-loop stable. Hence, the RCDs alone are a destabilizing influence that the root controller must overcome and stabilize. The destabilizing effect of RCDs in this case arises from the use of a single point sensor and a distributed actuator. The parts of the RCD that are inboard of the tip are non-colocated with the tip pitch sensor, so they destabilize certain mode shapes with nodes within the RCD region. Therefore, larger RCDs destabilize more modes with this control approach.

One possible but somewhat impractical solution is to use a distributed tip pitch sensing system, as I do in Chapter 4.C.3. In this case, each RCD segment pair has its own colocated pitch rate sensor and feedback loop. Figure 4.21 shows the response of this new system. There are no

encirclements of the critical point in this case, so the RCDs do not destabilize the inner loop. On the other hand, the damping of the first few modes is less than with a single sensor. With the single sensor, the entire RCD actuates as a unit, so its authority is concentrated towards damping the lowest modes. With distributed sensing, some segments may be opposing other segments at higher modes shapes. Hence, the control authority is distributed over the frequency spectrum. Other methods—such as frequency domain compensation (filtering)—may work better to concentrate the RCD authority in the first mode while keeping the system stable.

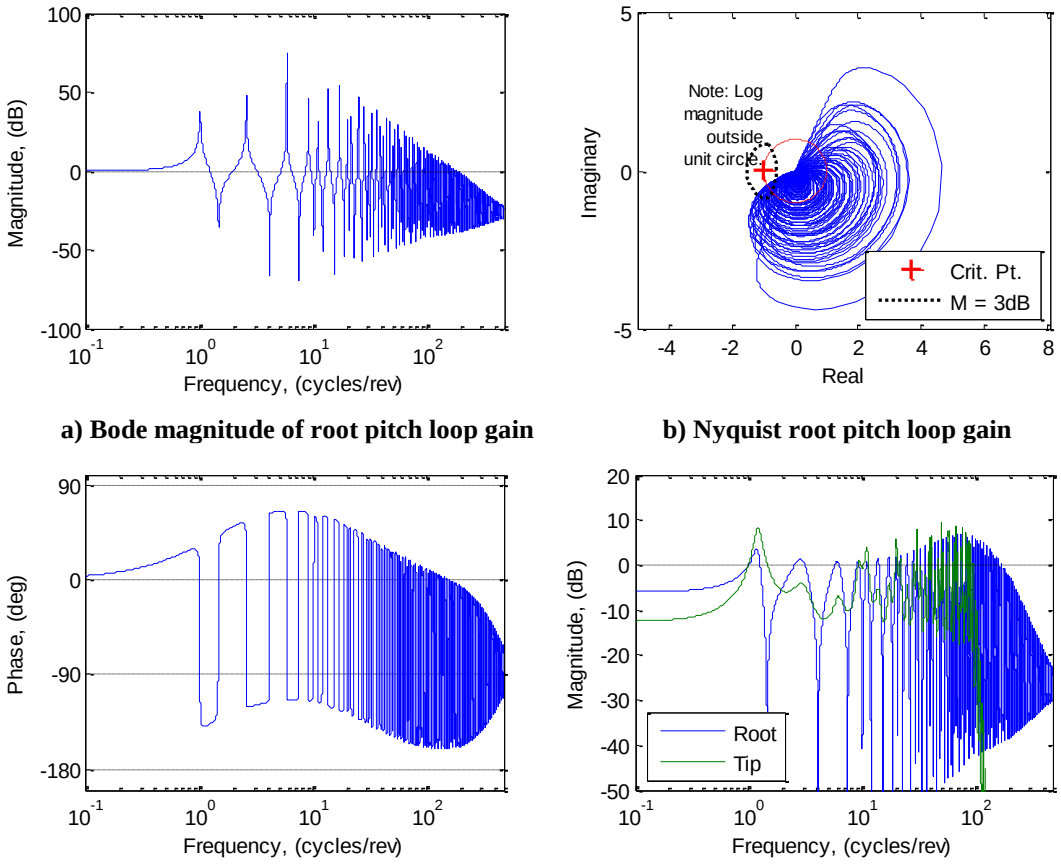

a) Bode magnitude of root pitch loop gain

b) Nyquist root pitch loop gain

c) Bode phase of root pitch loop gain

d) Closed-loop tracking of root and tip

Figure 4.21: Closed-loop response of RCD and distributed pitch sensing with w = 30 cycles/rev (0.5 Hz), κ = 2e-6 Nm^{2}s/rad, and f_{RCD} = 5%

D. Model validation with hanging blade experiments

I conducted dynamics tests on a hanging heliogyro blade specimen in a vacuum chamber at NASA Langley Research Center during the summer of 2012. These tests measured the blade's frequency response function (FRF) at several locations along the blade length. I use these experimentally derived FRFs to verify the membrane ladder FEM, estimate the material damping, find the mode shapes, and discuss coupling between flap bending and twisting motion. There has only been one other documented experiment to verify theories of heliogyro blade dynamics, and it was done in 1971 by MacNeal.[53] He spun a 0.001 in x 2 in x 77 in heliogyro blade for deployment and blade pitch control testing. Several factors limited this test's utility. Chiefly, it was conducted at atmospheric pressure. This meant that no estimate of material damping was possible, and the structural mode frequencies were shifted. Additionally, the blade was only subjected to a pulse transient, so a full FRF could not be determined. Furthermore, metrology was limited to video recordings with displacement measured at only two locations, so results were low fidelity. Consequently, they did not achieve very good theoretical agreement.

1. Experimental Setup

The general idea of the experiment is to hang a small blade sample inside a vacuum chamber, vibrate it at the root (top) over a range of frequencies, and measure the displacement at several points along the blade length. The goals of these this experiment and analysis were threefold:

1. Quantify coupling effects between flap and twist bending by looking at the mode shapes. This is important since the membrane ladder FEM assumes these motions are uncoupled, and coupled motion complicates the control problem.

2. Validate the membrane ladder FEM quantitatively by comparing theoretical and experimental mode frequencies and qualitatively by comparing the general shape of their FRFs.
3. Estimate the test membrane's material damping magnitude and character. Determine if the vacuum chamber pressure was low enough to avoid viscous drag damping.

Since the experimental blade is in a gravity field and not rotating, I modify the equations of motion by removing the gyroscopic force and replacing the centrifugal stiffness K^c with the gravitational tension stiffness K^{grav}. Start by adjusting the blade tension:

$$T_n^{grav} = g\left[\rho hc(R - x_n) + m_{tip}R + \sum_{j=\left\lceil (N_{bat}+1)\frac{x_n}{R}\right\rceil}^{N_{bat}} j\frac{m_{bat}R}{N_{bat}+1}\right] \tag{4.37}$$

$$K_n^{grav} = \frac{T_n^{grav}c^2}{12\Delta x} \tag{4.38}$$

$$J_n\ddot{\theta}_n = K_n^{grav}(\theta_{n+1} - \theta_n) - K_{n-1}^{grav}(\theta_n - \theta_{n-1}) + \frac{\kappa}{\Delta x}(\dot{\theta}_{n+1} - 2\dot{\theta}_n + \dot{\theta}_{n-1}) \tag{4.39}$$

where g = 9.81 m/s^2 is the gravitational acceleration.

Figure 4.22 shows the experimental setup. I excited the blade using a piezoelectric actuator and captured the blade's motion with Laser Doppler Vibrometers (LDVs). I used two different actuators; one actuator vibrated primarily in bending for flap motion and a second actuator primarily generated twist vibrations. In this way, I could look at the twist response coupling to flap actuation and vice versa. The system's input signal was the applied voltage to the actuator. This signal was set to burst random over the range 0.1 to 12.5 Hz in order to capture the blade's first few structural modes. A burst random input is good at capturing the blade damping since it captures the response decay between bursts. The system's outputs were the vibration velocity as measured by the LDVs at ten locations along the blade length. These locations formed a grid that measured the left and right edges of the blade at all five quarter points (0, ¼, ½, ¾, and 1 times the

blade length). The LDVs output an analog signal sensitive to one μm/s, which I sampled at 100 Hz. With only two LDVs, I had to sample each quarter point sequentially rather than capturing all blade motion simultaneously. I captured data at each point until the response's coherence was no longer appreciably improving with each input burst, which was anywhere from 20 minutes to an hour.

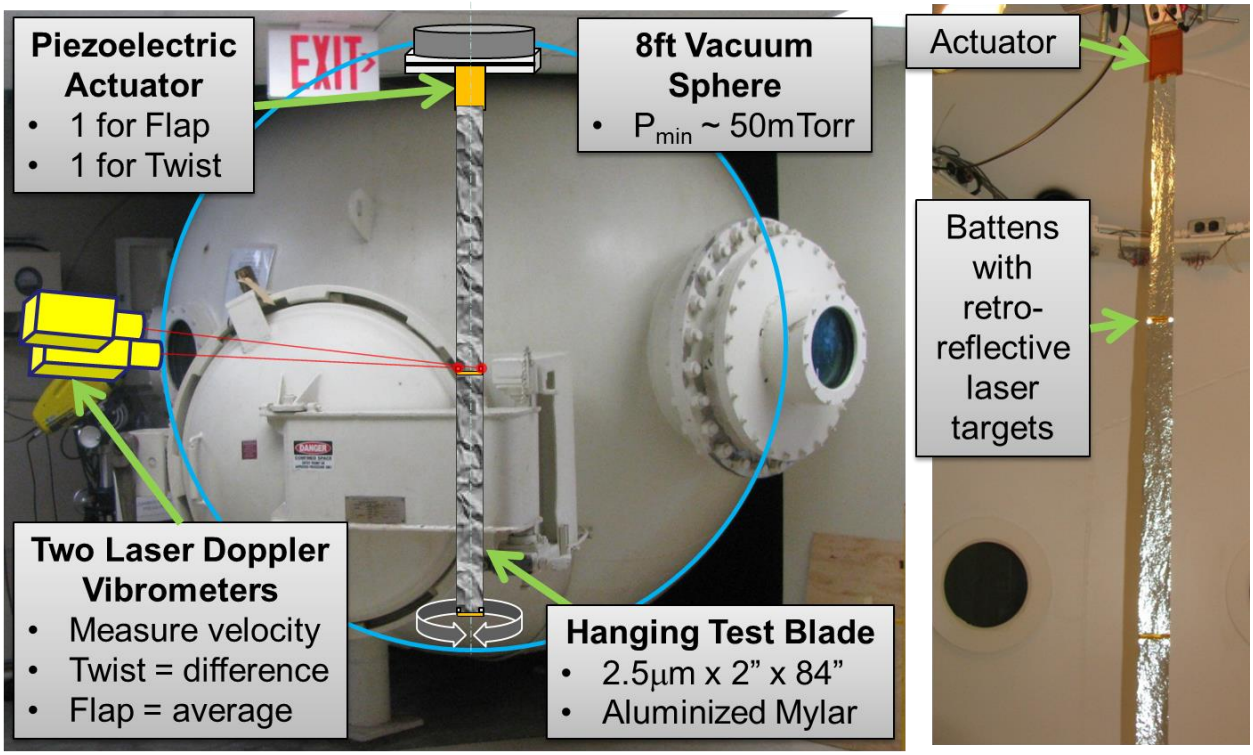

a) Vacuum chamber exterior **b) Mounted test article**

Figure 4.22: Experimental setup

I then post-processed the LDV velocity time histories to extract the blade's FRFs as described below.

1. Remove offsets and linear tilt in the data record via Matlab's `detrend` function.
2. Decimate by a factor of 13 from 100 Hz to 7.7Hz, yielding a Nyquist frequency of 3.8 Hz. Damping acted like a low-pass filter, and noise dominated the response at frequencies above about 3.8 Hz. Filtering the signal focuses the analysis on the frequency range with a good signal-to-noise ratio. Matlab's `decimate` function uses an 8th order Chebyshev infinite

impulse response (IIR) filter run forwards and backwards in time to remove phase shift. Decimate then down samples the signal by the decimation factor. The filter is necessary to avoid aliasing effects in the down-sampled signal.

3. For some of the analysis below, I isolate the twist and flap responses at each quarter-point by either averaging or differencing the left and right LDV time-domain responses per Eq. (4.40):

$$v_{twist} = \frac{v_{left} - v_{right}}{c}\left(\frac{\text{rad}}{\text{s}}\right), \qquad v_{flap} = \frac{v_{left} + v_{right}}{2}\left(\frac{\mu\text{m}}{\text{s}}\right) \tag{4.40}$$

where v is the LDV measurement time history and c is blade chord or width (2 in).

4. Transform the signal to frequency space using `tfestimate` to estimate the transfer function, $V = P_{yx}/P_{xx}$ where P_{yx} is the cross power spectral density (PSD), and P_{xx} is the input PSD. The `tfestimate` function applies a periodic Hamming window, and I find that a 50 sec window (five times the period of the lowest frequency of interest) works well. That way each window contains several copies of the entire spectrum.

5. Change the system input from applied voltage to root motion by dividing by the voltage-to-root frequency response:

$$U_n = \frac{V_n}{V_1} \tag{4.41}$$

where n represents the quarter point index from 1 at the root to 5 at the tip.

The root-to-quarter-point frequency responses U_n are the FRFs that I then analyze using the System Observability Controllability Identification Toolbox (SOCIT) for Matlab developed by Jer-Nan Juang, Lucas Horta, and Minh Phan.[43] This toolbox estimates the linearized system state-space matrices (A, B, C, and D) by taking the singular value decomposition of the Hankel Matrix of observer Markov Parameters. SOCIT derives the observer Markov Parameters from a least squares fit of the discrete FRF data.[42] The program can accept any number of system inputs and

outputs. This system has a single input with ten outputs, one for each grid point. With a state-space system, SOCIT can then compute the modes and mode shapes by finding the eigenvalues and eigenvectors of the system matrix *A*. SOCIT also computes several accuracy indicators, the damping ratio, and other useful parameters.

The state space system can have any number of modes up to the number of discrete frequencies in the FRF, but it is desirable to pick the minimum number of modes to fit adequately the frequency range of interest. This ensures one's selected modes represent physical processes rather than fitting random noise; however, with real world, noisy data it is impossible to avoid some duplicate and computational modes. SOCIT identifies some of these spurious modes with accuracy indicators such as the extended modal amplitude coherence and weighted modal phase colinearity.

2. Experimental Results

Figures 4.23 and 4.24 show the experimental FRFs using the twist and flap actuators, respectively. The subplots are in a grid that mirrors the stations' locations on the test article. These FRFs represent the response of each grid point to excitation at the root. The dashed green line is the system fit found by SOCIT, and the valid modes identified by SOCIT are annotated sequentially. The processed FRFs are very clean, indicating that the measured signals had very low noise and that I gathered sufficient time history for this frequency range. The exception is at the blade tip at higher frequencies, especially for twist motion. The blade tip was as far away from the actuator as possible, so damping (both material and viscous) had the most filtering of high frequencies. Surprisingly, the first mode is not the largest magnitude at most stations. This may be due to viscous damping from residual air in the vacuum chamber. These modes represent pendulum motion and would have the most drag.

Next, one can see that every pole has a corresponding zero at the Q1 station, but there are few to no identifiable zeros at the blade tip (Q4). The number of system zeros drops off from the root to the tip. This is typical of systems with a free boundary condition, as the unrestrained tip cannot have a zero. Lastly, the flap FRFs have an interesting triple mode at modes 3, 4 and 5. This may be due to coupling of twist motion excited by the flap actuator.

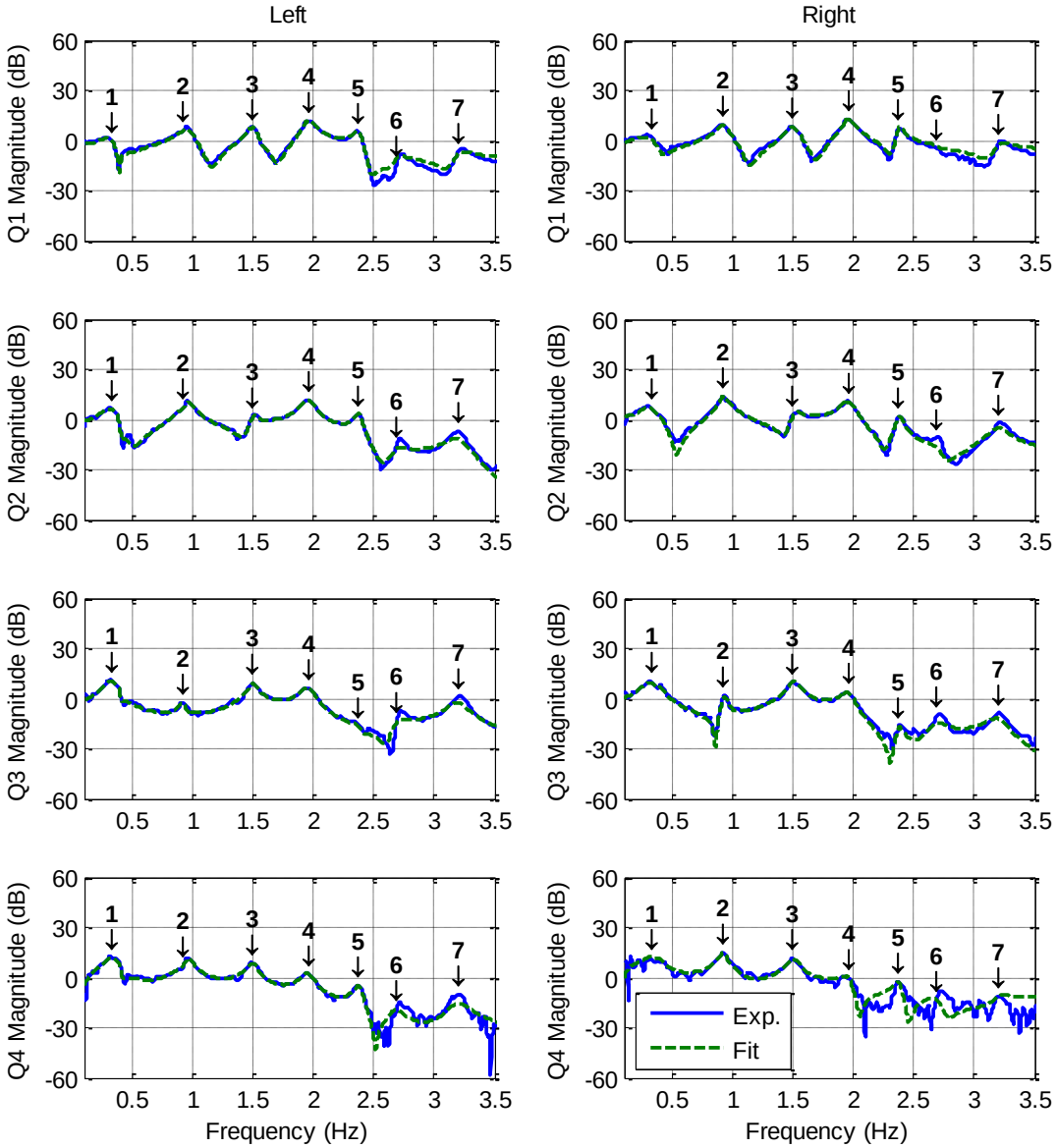

Figure 4.23: Quarter-point FRFs using the twist actuator with the SOCIT identified modes

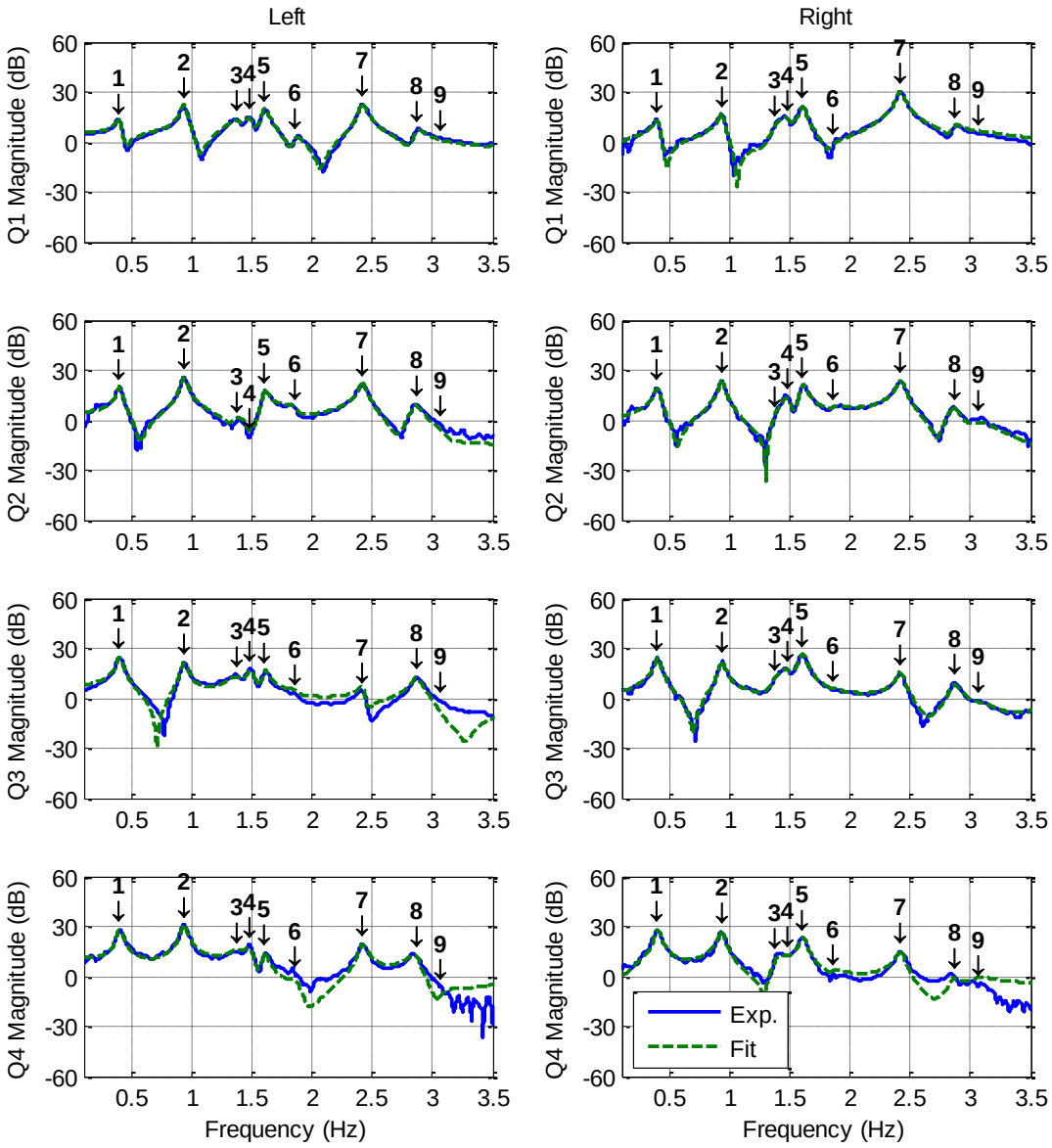

Figure 4.24: Quarter-point FRFs using the flap actuator with the SOCIT identified modes

In order to examine this coupling further, I plotted the mode shapes or eigenvectors at each mode frequency in Figures 4.25 and 4.26. A shaded plane indicates the zero-level on each shape. Each shape is also annotated with the mode frequency, damping ratio ζ, an estimate of the motion's relative flap and twist character, and the motion's mode number in each direction. SOCIT estimates the frequencies and damping from the state space system matrices. I separate the flap and twisting motion in each mode shape (i.e. its character) using Eqs. (4.40). I determine the directional mode (e.g. 1st Twist) by counting the number of node crossings of each motion. Since

there are only five stations, this experiment can only verify up to the fourth mode. It does not have the spatial fidelity to capture all the nodes of higher modes, so they are marked as unknown in Figures 4.25 and 4.26.

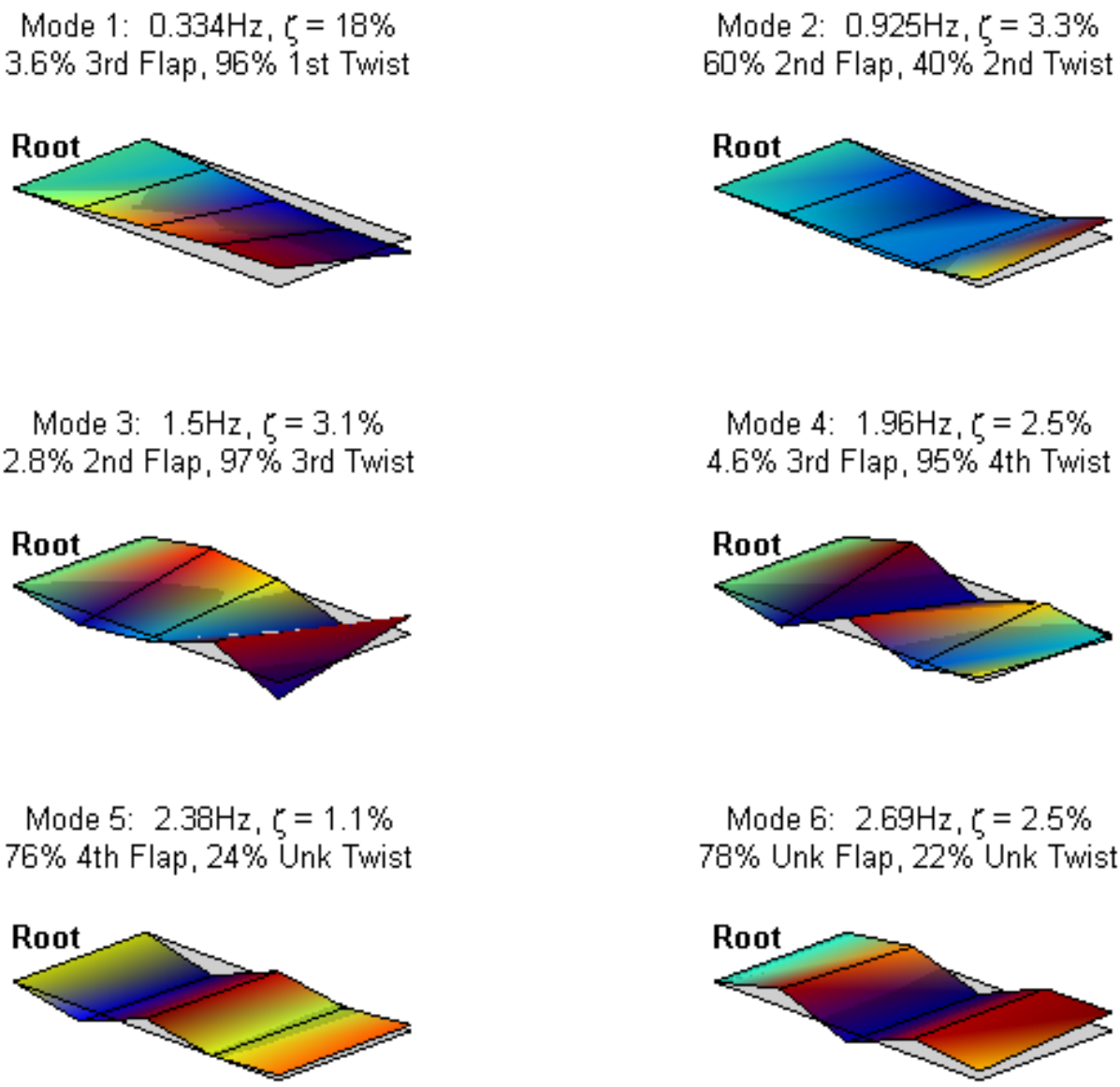

Figure 4.25: Mode shapes for the first six modes using the twist actuator

The pictures of mode shapes give a much clearer idea of what is happening at each mode frequency than the individual FRFs. The twist actuator's 1st, 3rd and 4th modes (Figure 4.25) are almost pure twist, but the 2nd mode is coupled about evenly with flap. This corresponds to the flap

actuator's 2nd mode in Figure 4.26 whose frequency is <1% away. In fact, the 2nd flap and twist modes are so close that there is no forking apparent on their FRFs, even though there is coupling in both cases.

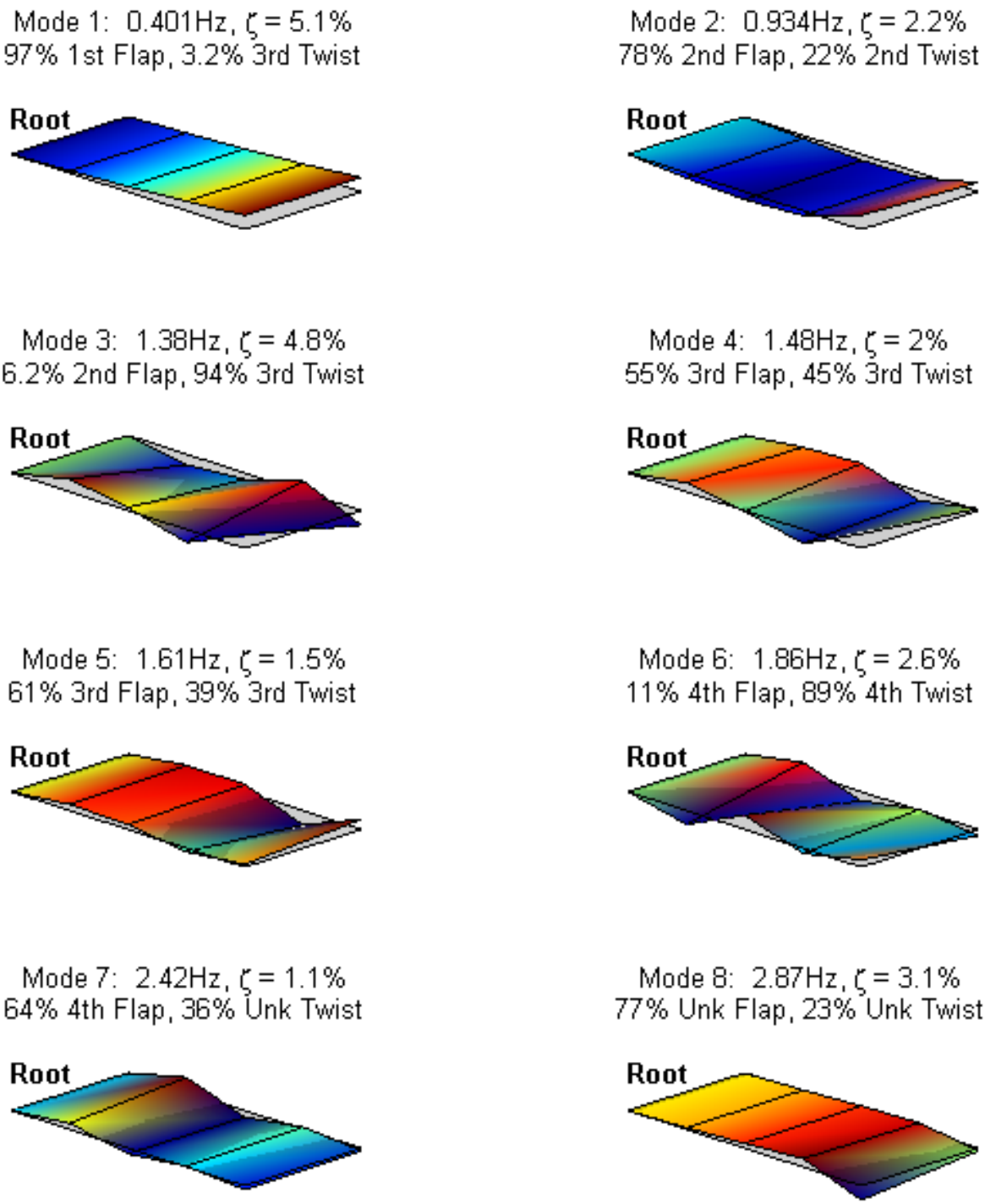

Figure 4.26: Mode shapes for the first eight modes using the flap actuator

The picture for the flap actuator is much less clear. The 1st and 2nd flap modes are easily identified, but the 3rd flap mode is spread between system modes 3, 4 and 5 as seen earlier in Figure 4.24. System mode 3 (1.38 Hz) is almost purely twist coupling, but system modes 4 (1.48 Hz) and 5 (1.61Hz) are a smearing of both the 3rd twist and 3rd flap modes. It appears that system mode 5 is the true 3rd flap mode, as this has the highest response magnitude in flap (see Figure 4.24) and the most flap character (61%) of these three modes. Additionally, system mode 4 is only 1.3% away from the 3rd twist mode for twist actuation in Figure 4.23. Therefore, system modes 3 and 4 are largely the result of twist excitation from flap actuation. System mode 6 is also a result of twist excitation from flap actuation, but its response is hardly noticeable in Figure 4.24. Finally, while the first three flap and twist mode frequencies are nearly identical, the 4th flap mode (system mode 7) is separated 0.46 Hz from the 4th twist mode at 1.96 Hz. This large gap makes it impossible for the two motions to couple, which suggests that coupling should not be as much of a problem at higher modes.

The next experimental goal was to verify the membrane ladder FEM. Since the FEM is one-dimensional, I isolated the experimental twist response to the twist actuator per Eqs. (4.40) for comparison with the twist FEM equation. Similarly, I isolated the flap response to the flap actuator for comparison with the flap FEM equation. Figures 4.27 and 4.28 show the twist and flap comparisons, respectively. In this case, I number the modes according to where they match up with theory, omitting the modes arising from coupling. The flap and twist FEM equations of motion are identical, except that I tuned their mass parameters slightly differently. The flap equation includes the mass of the four chordwise battens (pictured in Figure 4.22) affixed to the test article. The twist equation agrees better with theory with the batten inertia omitted. For some

reason, the additional inertia of the battens plays a larger part in the flapwise motion than the twist motion.

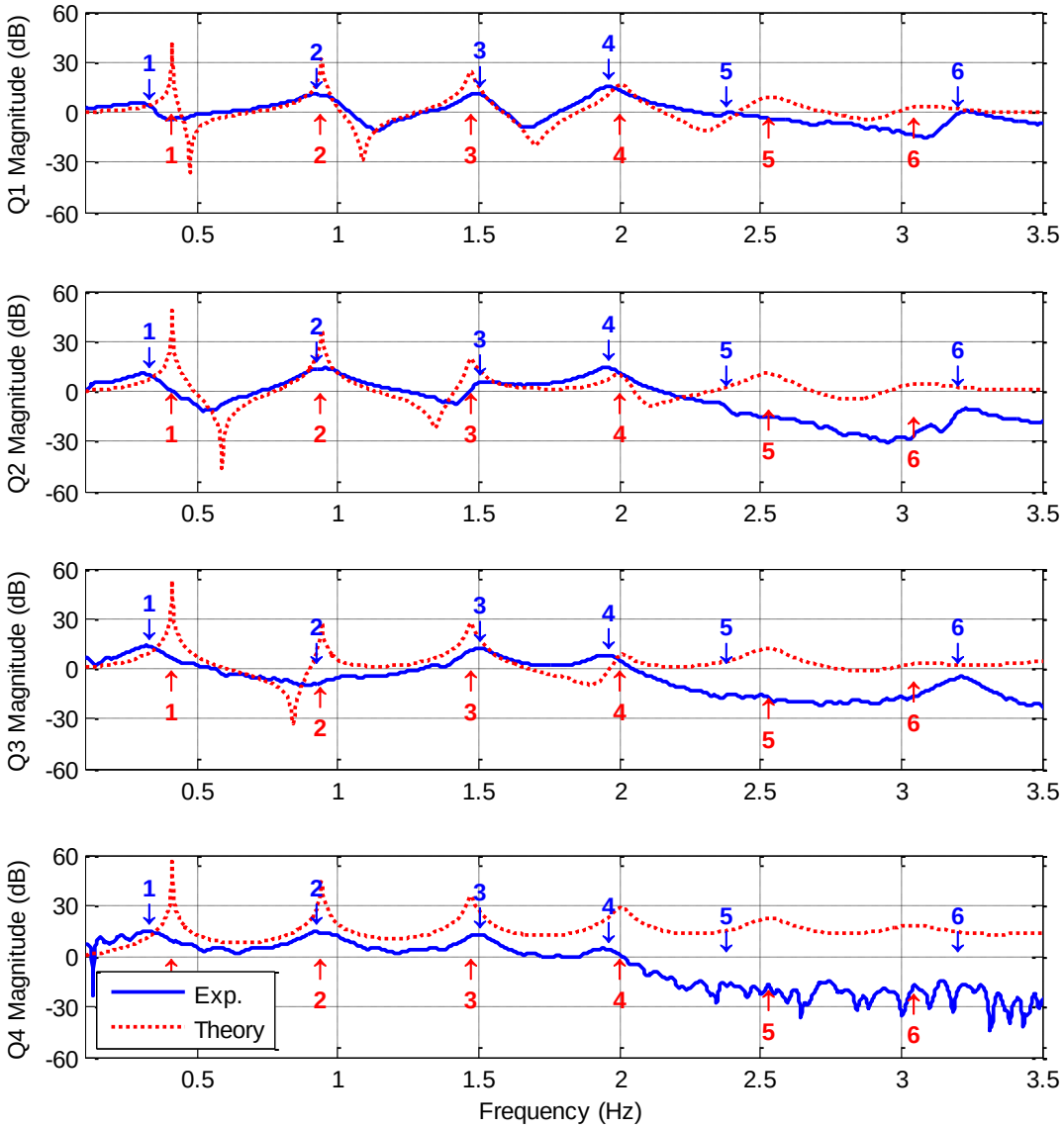

Figure 4.27: Experimental vs. theoretical agreement in twist motion using the twist actuator

Regardless, this test article agrees very well with the theory in both flap and twist after minimal tuning. Quantitatively, the root mean square difference from theory of the modal frequencies in this frequency range (3.5 Hz) is only 8.4% in twist and 4.5% in flap. Tables 4.5 and 4.6 list the differences from theory for each mode individually. Qualitatively, both responses trace similar responses over the whole frequency range.

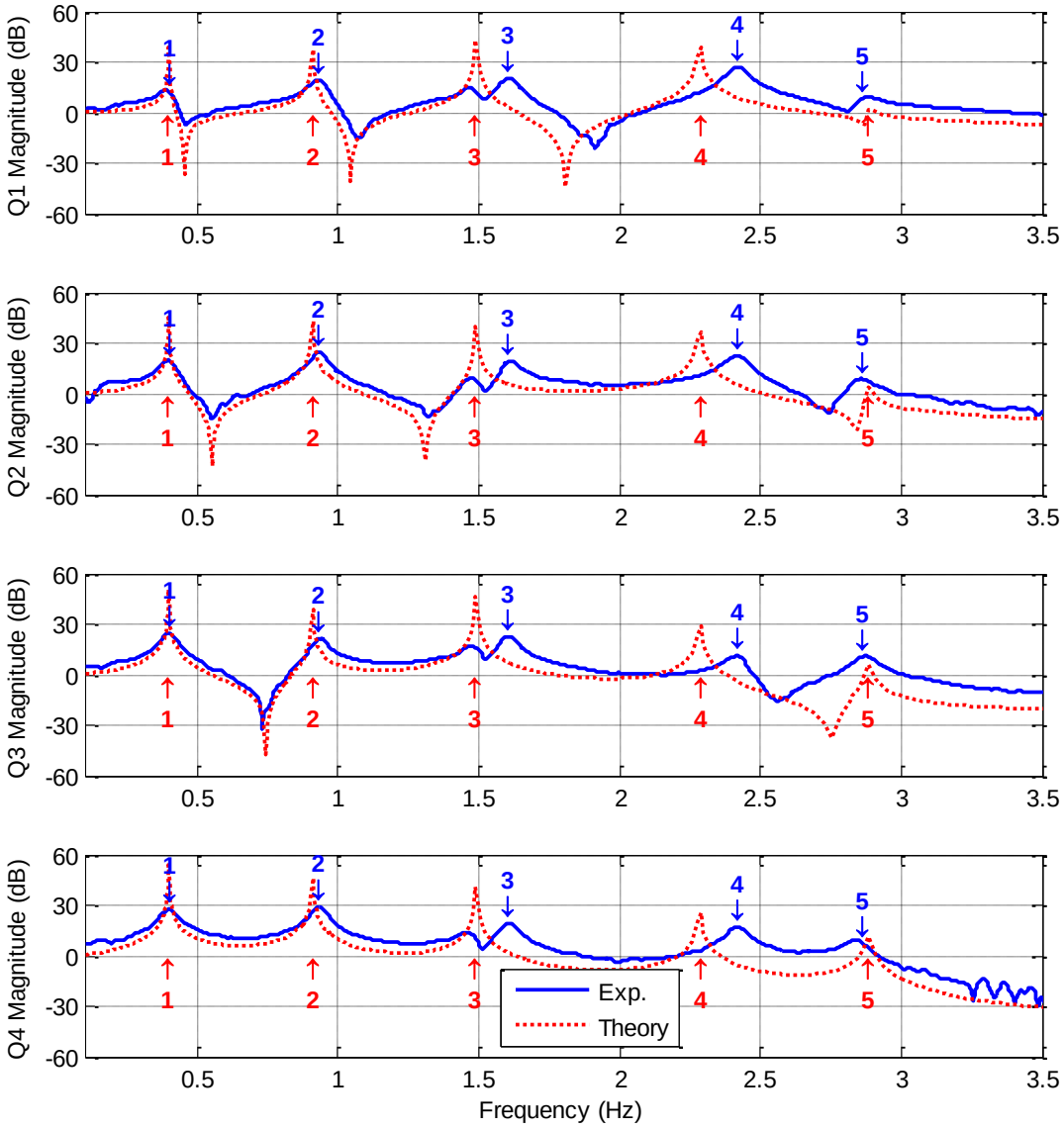

Figure 4.28: Experimental vs. theoretical agreement in flap motion using the flap actuator

The last experimental goal is to estimate the blade's material damping value and character. SOCIT estimated the damping ratio of each mode from the realization of the full system. These values are plotted in Figure 4.29, listed in Tables 4.5 and 4.6, and annotated on the mode shapes in Figures 4.25 and 4.26. Additionally, Figure 4.29 shows the damping ratio as modeled in the membrane ladder FEM.

The chief differences with theory so far result from the model's representation of damping. Eq. (4.39) uses a linear damping term that causes the damping ratio to increase with frequency.

This causes the FEM's modal peaks to start out steep (low damping ratio) and flatten out with increasing frequency. I selected the damping constant κ such that the FEM modal peaks approximately line up in magnitude with the experimental results. This only affects the visualization and does not shift the mode frequencies. Furthermore, the experimental twist response rolls off in magnitude towards the blade tip. I believe this is also due to unmodeled damping effects that are more prominent in twist and towards the blade tip.

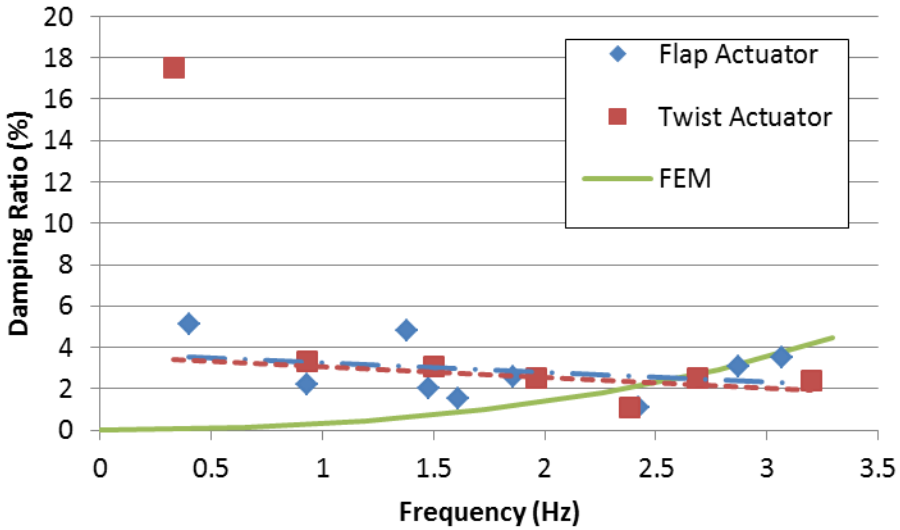

Figure 4.29: Damping ratio of each mode for both actuators with trend lines

The damping character plotted in Figure 4.29 decreases linearly with frequency, which the plotted linear trends illustrate. This contrasts with the FEM where damping increases with frequency, so some other damping model should be considered. The trend lines also show that the damping is independent of the direction of motion (flap or twist). The one exception is the first twist mode, which is an outlier in this experiment and was omitted from the trend line. This may be due to viscous damping having a larger effect on this mode. It would be prudent to investigate this phenomenon with additional tests at lower pressures and with different test article dimensions.

Table 4.5: Twist actuator modal summary

System Mode #	Exp. Freq. Hz	Theo. Freq. Hz	Δ Freq. %	Damping Ratio %	Flap Character %	Flap Mode #	Twist Character %	Twist Mode #
1st	0.33	0.41	18.6	17.5	3.6	3rd	96.4	1st
2nd	0.93	0.94	1.6	3.3	60.4	2nd	39.6	2nd
3rd	1.50	1.48	-1.9	3.1	2.8	2nd	97.2	3rd
4th	1.96	2.00	2.0	2.5	4.6	3rd	95.4	4th
5th	2.38	2.52	5.5	1.1	75.8	4th	24.2	Unk.
6th	2.69	N/A	N/A	2.5	78.0	Unk.	22.0	Unk.
7th	3.20	3.02	-6.1	2.4	47.3	Unk.	52.7	Unk.

Table 4.6: Flap actuator modal summary

System Mode #	Exp. Freq. Hz	Theo. Freq. Hz	Δ Freq. %	Damping Ratio %	Flap Character %	Flap Mode #	Twist Character %	Twist Mode #
1st	0.40	0.40	-0.5	5.1	96.8	1st	3.2	3rd
2nd	0.93	0.91	-2.7	2.2	77.7	2nd	22.3	2nd
3rd	1.38	N/A	N/A	4.8	6.2	2nd	93.8	3rd
4th	1.48	N/A	N/A	2.0	55.0	3rd	45.0	3rd
5th	1.61	1.49	-7.8	1.5	61.5	3rd	38.5	3rd
6th	1.86	N/A	N/A	2.6	11.0	4th	89.0	4th
7th	2.42	2.29	-5.8	1.1	64.4	4th	35.6	Unk.
8th	2.87	2.88	0.5	3.1	77.3	Unk.	22.7	Unk.
9th	3.07	N/A	N/A	3.5	18.2	Unk.	81.8	Unk.

The damping ratios were all surprisingly high. All modes had damping ratios >1% and one as high 18% for the first twist mode. This could make blade controller design easier, as higher modes may not require active damping; however, the damping may still be due to atmospheric influences. I ran this experiment at the lowest pressure achievable with this chamber, about 50 mTorr (7 Pa), but I also did several runs at higher pressures. Figure 4.30 shows the trend in damping ratio with pressure for both the twist and flap actuator cases. I measured these data at only the blade midpoint since a full modal analysis is not necessary to estimate damping.

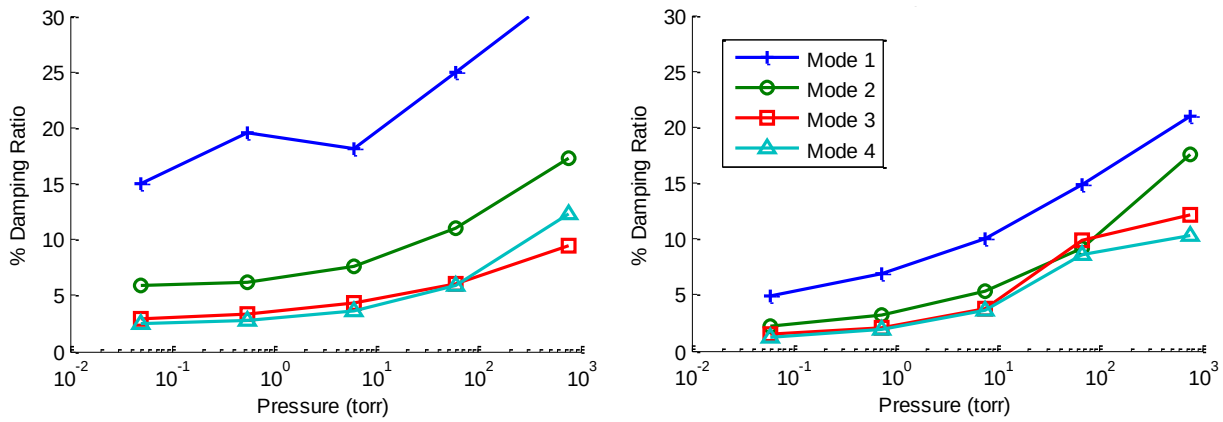

a) Twist actuator **b) Flap actuator**

Figure 4.30: Damping ratio vs. pressure measured at the blade midpoint (Q2)

This figure confirms that the chamber pressure was not low enough to eliminate the viscous damping effects, as the damping ratios' slopes are not quite flat at the lowest pressures. A better vacuum would result in further reductions in measured damping, and perhaps the first mode outliers would converge with the other modes. By visual extrapolation, the true material damping should still be above 0.1%. Regardless, the damping was low enough so as not to appreciably affect mode frequency; the experiment still validates the membrane ladder frequency response.

E. Nonlinear blade control

The blade analysis thus far has remained in the linear regime where excitation amplitude is immaterial and there is no coupling between different frequencies. Furthermore, Chapters 2 and 3 assume that the blades are flat in steady-state oscillation. Unfortunately, simulations show that the nonlinear dynamics of a membrane blade egregiously violate the flat-blade assumption in certain of the common operations listed in Table 1.5. For example, Figure 4.31 plots the root and tip motion for a simulation using the membrane ladder for (a) 25° and (b) 35° cyclic excitation along with the reference root signal. This excitation comes from a torque-source root actuator using a PD controller with root pitch feedback. The tip response for the 25° cyclic root pitch

excitation is very well behaved and quickly settles. In contrast, the tip response for a 35° cyclic—only 10° higher—is unacceptably large.

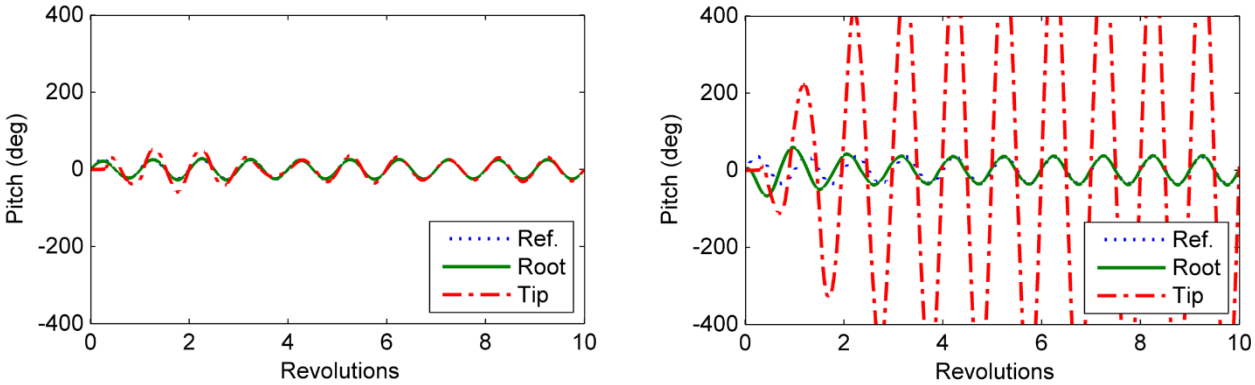

a) 25° cyclic amplitude **b) 35° cyclic amplitude**

Figure 4.31: Dynamic simulations of membrane ladder FEM for cyclic reference signal

This cyclic excitation instability is corroborated with simulations shown in Figure 4.32 using the Abaqus commercial FEA software package. These simulations model a uniform membrane with the HELIOS dimensions of Table 1.6 except there are no features or lumped mass. They use a material and numerical integration damping of 0.1%. This model also incorporates full 3D motion of the blade, SRP, material elasticity, and a free-spinning hub. Consequently, the Abaqus simulations required hours on a dedicated server whereas the membrane ladder simulations completed in a few seconds on a laptop. Note that the Abaqus simulation has more high-frequency excitation because there is no feedback control, whereas the root control law used in Figure 4.31 successfully damps the blades' natural response. While the magnitude of the tip excitation is not as large in Figures 4.32b as 4.31b, the 35° cyclic case is clearly less stable than the 25° case. The steady-state solution developed in Chapter 4.E.1 can guide blade design towards some mitigation of this problem, discussed in Chapter 4.E.2.

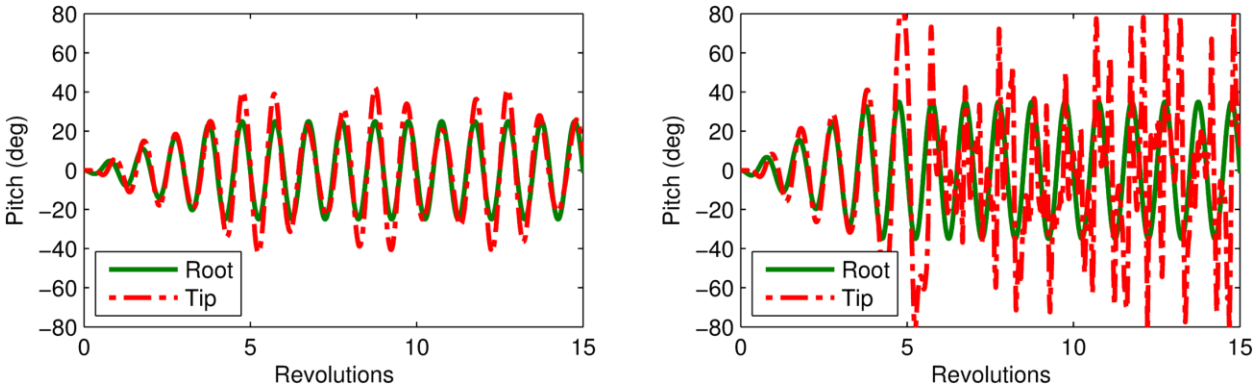

a) 25° cyclic amplitude **b) 35° cyclic amplitude**

Figure 4.32: Abaqus simulations of a membrane blade with cyclic excitation*

The second motivation for developing the steady-state solution is to augment the control law with feed-forward (FF), as discussed in Chapter 4.E.3. The linear controller optimization of Chapter 4.B found that feed forward was critical to enforcing blade pitch tracking, but the steady state solution for the nonlinear EOM is nontrivial. A gyroscopic torque in the rotating reference frame is a nonlinear spring that pulls the blade away from the reference pitch towards the plane of rotation (0° pitch). Without FF, PD feedback gains optimized to rapidly damp transients are too low to provide good tracking of the reference. Conversely gains high enough to enforce tracking result in much longer settling times, since the root actuator impedance becomes large, reflecting rather than absorbing modal oscillations.

1. Steady-state solution by Fourier harmonic expansion

The system of coupled, nonlinear differential equations represented by Eqs. (4.11) to (4.13) cannot be solved for $\theta(t)$ explicitly. One can approximate the solution through a series expansion. A harmonic series is convenient since the control system will excite the blade root sinusoidally at frequencies of multiple 0, ½, or 1 times the heliogyro rotation frequency Ω. Furthermore, simulations shown in section Chapter 4.E.3 reveal that the steady-state response is dominated by

* Abaqus simulations courtesy of Jerry Warren, Structural Dynamics Branch, NASA LaRC.

these frequencies and their harmonic multiples. Assuming such a harmonic series for the motions and efforts with unknown coefficients yields the following steady-state response at each blade rung for the root applied control torque $\tau_1(t)$:[69]

$$\theta_n(\phi) = \frac{\alpha_n^{(0)}}{2} + \sum_k \alpha_n^{(k)} \cos(k\phi) + \sum_k \beta_n^{(k)} \sin(k\phi) \tag{4.42}$$

$$\ddot{\theta}_n(\phi) = -\omega_b^2 \left[\sum_k \alpha_n^{(k)} k^2 \cos(k\phi) + \sum_k \beta_n^{(k)} k^2 \sin(k\phi) \right] \tag{4.43}$$

$$\tau_1(\phi) = \frac{\alpha_\tau^{(0)}}{2} + \sum_k \alpha_\tau^{(k)} \cos(k\phi) + \sum_k \beta_\tau^{(k)} \sin(k\phi) \tag{4.44}$$

where $\phi = \omega_b t$ is the phase parameter, ω_b is the base frequency or first harmonic, and k is the harmonic number. Superscript parentheses denote harmonic number (k) rather than exponents.

Assume a steady-state condition where the root controller has damped out the natural response transients and forced the root to track the reference pitch profile θ_{ref} from Eq. (2.1), shown as a harmonic series in Eq. (4.45). Eqs. (4.46) convert the five pitch profile parameters into their corresponding harmonic coefficients using a half-p base frequency ($\omega_b = \Omega/2$).

$$\theta_{ref}(t) = \frac{\alpha_{ref}^{(0)}}{2} + \alpha_{ref}^{(1)} \cos\phi + \alpha_{ref}^{(1)} \sin\phi + \alpha_{ref}^{(2)} \cos 2\phi + \beta_{ref}^{(2)} \sin 2\phi \tag{4.45}$$

$$\begin{aligned}
&\alpha_{ref}^{(0)} = -2\alpha_{co} && \phi = \omega_b t = \Omega t/2 \\
&\alpha_{ref}^{(1)} = -\alpha_{hp} \sin\left(\frac{\phi_{hp}}{2} + \frac{\pi}{4} \operatorname{sign} \alpha_{hp}\right) && \beta_{ref}^{(1)} = \alpha_{hp} \cos\left(\frac{\phi_{hp}}{2} + \frac{\pi}{4} \operatorname{sign} \alpha_{hp}\right) \\
&\alpha_{ref}^{(2)} = -\alpha_{cy} \sin\phi_{cy} && \beta_{ref}^{(2)} = \alpha_{cy} \cos\phi_{cy} \\
&\alpha_{ref}^{(k)} = 0 \; for \, k > 2 && \beta_{ref}^{(k)} = 0 \text{ for } k > 2
\end{aligned} \tag{4.46}$$

The system of N+1 equations represented by Eqs. (4.11) to (4.13) is underdetermined with N+2 unknowns $\tau_1(\phi)$, $\theta_1(\phi)$, … , $\theta_{N+1}(\phi)$. Applying the steady-state boundary condition that $\theta_1(\phi)$

= $\theta_{ref}(\phi)$ remedies this, but the equations cannot simply be "unzipped" from root to tip since $\tau_1(\phi)$ is still unknown. Therefore, solution by iteration is required. I use Matlab's `fsolve` function for multiple harmonics of interest and `fzero` for a single harmonic. Either forward shooting (working from root to tip) or backward shooting (working from tip to root) will work, but I find backward shooting to converge in fewer iterations and to be more stable. The basic method is:

1. Select the base frequency ω_b and harmonics of interest k. It is neither possible nor desirable to calculate an infinite harmonic series, but most of the blade dynamics are captured with harmonics zero to four of half-p (i.e. k = {0, 1, 2, 3, 4} and $\omega_b = \Omega/2$). See section Chapter 4.E.3 for justification.
2. Make an initial estimate of the tip harmonic coefficients $\alpha_{N+1}^{(k)}$ and $\beta_{N+1}^{(k)}$. Convergence of the multi-harmonic solution with `fsolve` is sensitive to this estimate, but `fzero` for a single harmonic is not sensitive. I use an initial estimate of $\alpha_{N+1}^{(k)} = \beta_{N+1}^{(k)} = 0$ for the `fzero` function. In solving for multiple harmonics, I seed `fsolve` with the results from a single-harmonic run on `fzero` at the harmonic with the largest reference amplitude. This solved the convergence sensitivity issue.
3. Iterate to solve for the actual tip coefficients.
   a. For $n = N+1, \ldots, 2$
      i. Substitute $\alpha_n^{(k)}$ and $\beta_n^{(k)}$ of all harmonics of interest into Eqs. (4.42) and (4.43) to get $\theta_n(\phi)$ and $\ddot{\theta}_n(\phi)$.
      ii. Substitute $\theta_n(\phi)$, $\ddot{\theta}_n(\phi)$, and $\theta_{n+1}(\phi)$ into Eqs. (4.12) or (4.13) and solve for $\theta_{n-1}(\phi)$:

$$\theta_N(\phi) = \theta_{N+1} + \text{atan}\left[\frac{1}{K_N^c}\left(J_{N+1}\ddot{\theta}_{N+1} + \frac{K_{N+1}^g}{2}\sin 2\theta_{N+1}\right)\right] \equiv f_N(\phi)$$
$$\theta_{n-1}(\phi) = \theta_n + \text{atan}\left[\frac{1}{K_{n-1}^c}\left(J_n\ddot{\theta}_n + \frac{K_n^g}{2}\sin 2\theta_n - K_n^c \tan(\theta_{n+1} - \theta_n)\right)\right] \equiv f_{n-1}(\phi) \quad (4.47)$$

iii. Solve for $\alpha_{n-1}^{(k)}$ and $b_{n-1}^{(k)}$ for all harmonics of interest using numerical integration of:[69]

$$\alpha_{n-1}^{(k)} = \frac{1}{\pi}\int_0^{2\pi} f_{n-1}(\phi)\cos(k\phi)\,d\phi$$
$$\beta_{n-1}^{(k)} = \frac{1}{\pi}\int_0^{2\pi} f_{n-1}(\phi)\sin(k\phi)\,d\phi \quad (4.48)$$

b. The error returned to the iterative solver is the difference between the calculated $\alpha_1^{(k)}$ and $\beta_1^{(k)}$ and the reference root excitation coefficients $\alpha_{ref}^{(k)}$ and $\beta_{ref}^{(k)}$.

4. Once the solver converges on the blade pitch harmonic coefficients, the root control torque harmonic coefficients are given by solving Eq. (4.11) for $\tau(\phi)$:

$$\tau_1(\phi) = J_1\ddot{\theta}_1 + K_1^g\frac{1}{2}\sin 2\theta_1 - K_1^c\tan(\theta_2 - \theta_1) \equiv f_\tau(\phi) \quad (4.49)$$

then substituting $\theta_1(\phi)$, $\ddot{\theta}_1(\phi)$, and $\theta_2(\phi)$ and solving for coefficients $\alpha_\tau^{(k)}$ and $\beta_\tau^{(k)}$ with Eqs. (4.48).

I have found the method above to be very stable and always converge on the solution corresponding to dynamic simulation results; however, this does not prove universal convergence or solution uniqueness. This solution of the steady-state blade shape has several uses. For example, section Chapter 4.E.2 will use the steady-state blade response at a single harmonic to improve blade design. Then, section Chapter 4.E.3 will use the root torque multi-harmonic response to augment a blade pitch control system with FF control. Although not discussed here, this solution could also be incorporated into `HGForce` (Chapter 2.A) to optimize the pitch profile for maximum net spacecraft thrust or attitude control torque in a certain direction.

2. Structural Dynamics Concerns and Mitigation with Single Harmonic Solution

This section will examine the blade's steady-state root-to-tip response using the single frequency harmonic expansion and the HELIOS parameters. Only showing the root-to-tip response of a single harmonic still captures the gross blade response while being much simpler to visualize. Higher harmonics do not dominate the dynamics (shown later), and blade pitch is monotonic from root to tip below the second structural mode. Figure 4.33 shows the steady-state response of the membrane ladder FEM found using the iterative procedure above for the three primary pitch profiles at a range of excitation amplitudes. This confirms the unacceptable nonlinear blade response from Figure 4.31 that does not appear in the linearized system: the amplitude of the tip response to half-p and cyclic abruptly jumps much higher than the root as the root amplitude increases. This behavior in the steady state analytic solution confirms that the problem is in the natural dynamics and not with the root controller. For comparison, these responses converge to the linear system response at zero root excitation amplitude in Figure 4.33.

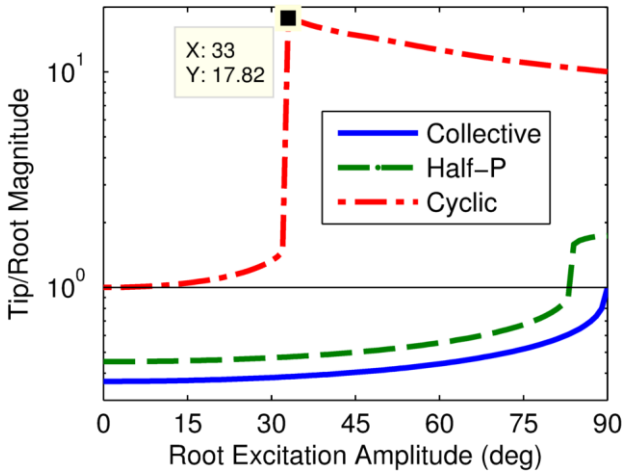

Figure 4.33: Root-to-tip amplitude of the three pitch profiles using the membrane ladder FEM

One can also use the steady-state solution to generate a two-dimensional, nonlinear describing function (DF) showing the blade's response vs. excitation amplitude and frequency.

This DF is similar to that developed in Ref. 45, but their methodology is a quasi-linearization about a range of amplitudes. Figure 4.34 shows the root to tip pitch amplitude DF with the half-p and cyclic curves corresponding to Figure 4.33 overlaid (black lines). The first structural mode from the linear case (drawn at $\alpha_1 = 0°$) initially shifts down in frequency as the root amplitude increases, but the system retains a quasi-linear frequency response. At around 30°, a bifurcation of sorts occurs, and the system behavior becomes distinctly nonlinear. The sharp jumps in cyclic and half-p response of Figure 4.33 correspond to their intersection with this shifting first mode.

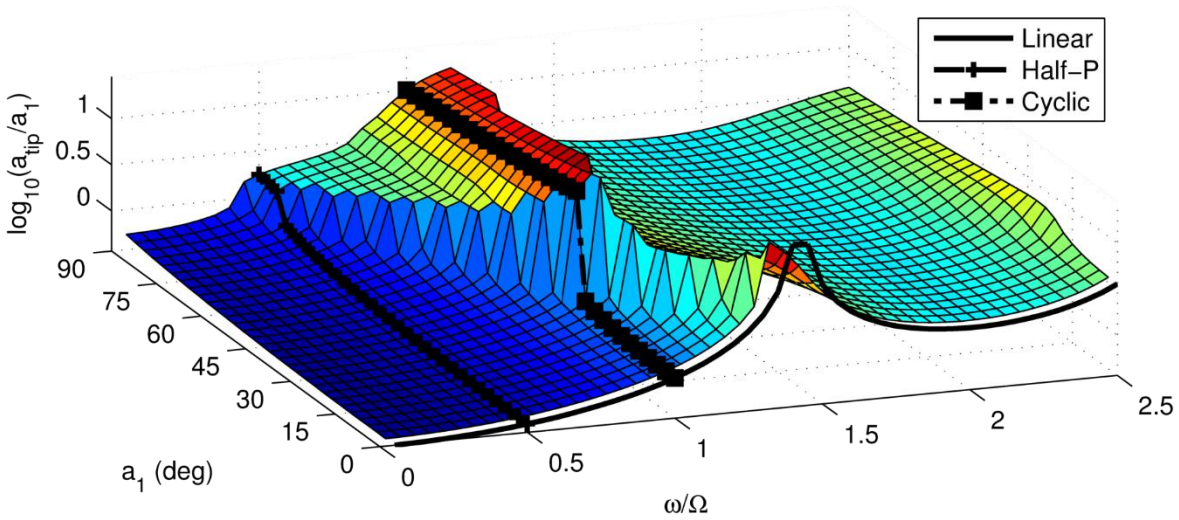

Figure 4.34: Root-to-tip amplitude DF using the membrane ladder FEM

This nonlinear behavior is problematic, but there are several options for keeping the blade acceptably flat. First, limit the root excitation amplitude, for example to <25° for cyclic and <75° for half-p. This would limit operations to the much flatter area below and to the left of the first mode. Unfortunately, cyclic amplitudes of 40° or higher are optimal for attitude and orbit control, so it is beneficial to increase the size of the flatter response area instead to encompass cyclic excitation up to at least 70°. Another option is to implement some form of active blade tip control like the RCDs of Chapter 4.C. This would add complexity and mass to the system, however, and decrease the original appeal of the heliogyro. A third option is to alter the blade's construction so as to increase the centrifugal stiffness relative to the gyroscopic and inertia terms.

Consider two possible variations on the blade construction: one to redirect the tension stress flow and one to increase blade tension. In Chapter 4.A, the rope ladder FEM tripled the centrifugal stiffness over the membrane ladder by concentrating the tension along the leading and trailing edges. This configuration could be approached with edge reinforcing or by "hanging" the blade on edge filaments separated by battens. A thin strip of Kapton tape edge reinforcing on the HELIOS blade would only add about 50 g or 7% to the blade mass. Increasing blade tension also increases the centrifugal stiffness, but the trick is to increase centrifugal stiffness relative to the gyroscopic and inertia terms. All three terms contain Ω^2, so no change in spin rate would achieve the desired outcome. The next easiest way to increase tension is by adding mass to the blade tip. This would shift the mode frequencies up like tensioning a guitar string. Any tip bar mass contributes to the mass moment of inertia *J*, so it would increase the gyroscopic and inertia terms proportionally with little net effect. Therefore, the tip mass should be a point mass at the twist axis so as not to contribute to *J*.

Figure 4.35 compares the effects of 50 g of edge reinforcing versus a 50 g tip point mass. The edge reinforcing has the largest effect by far, dramatically dropping the maximum tip response and smoothing out the abrupt jump in response for cyclic compared to Figure 4.33. The half-p profile now has an acceptable response at all amplitudes. Figure 4.36 gives the DF using both edge reinforcing and a tip mass simultaneously. The offending mode is now shifted up in frequency for all amplitudes and its effects are much smoother at higher amplitudes. The maximum cyclic response ratio is now only 1.8 at 90°, and the 1.25 point is pushed out to 58°, above the 42° optimal cyclic amplitude for lateral thrusting. Because of these improvements, all simulations henceforth incorporate both these blade changes for enhanced flatness.

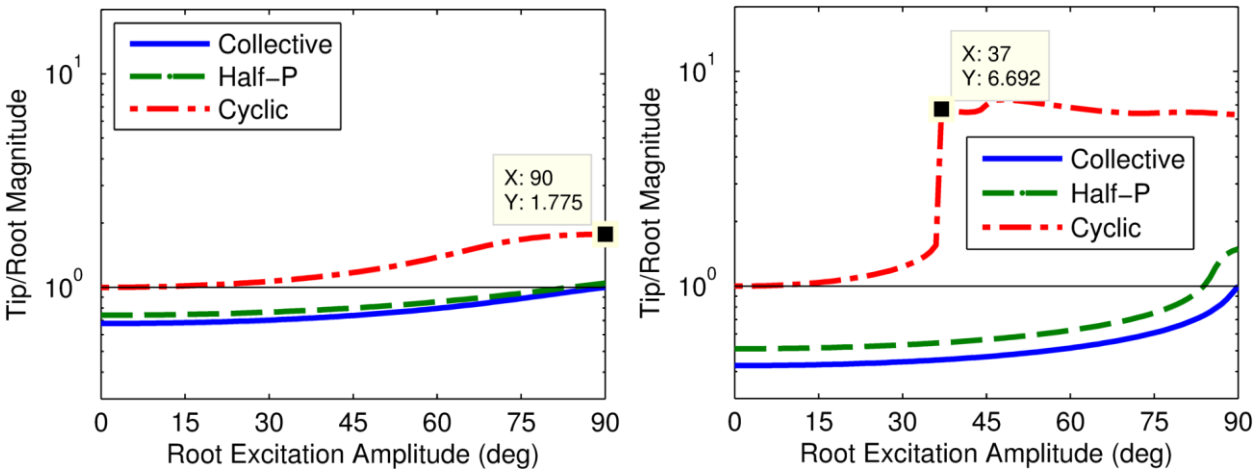

a) 50g of edge reinforcing, rope ladder FEM **b) 50g tip point mass, membrane ladder FEM**

Figure 4.35: Root-to-tip amplitude of the three pitch profiles for different blade construction

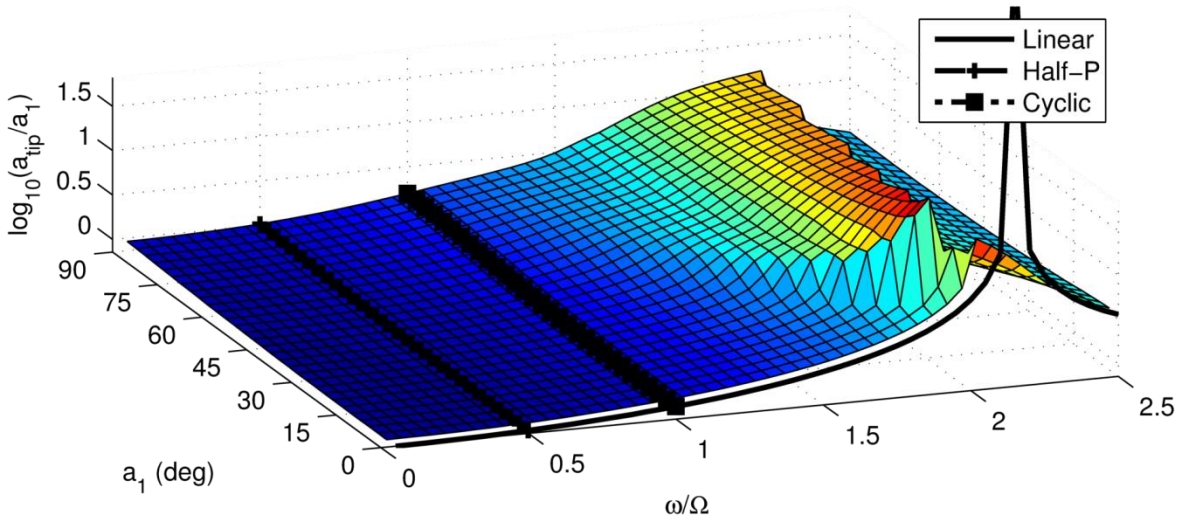

Figure 4.36: Root-to-tip amplitude DF, rope ladder FEM, 50 g edge reinforcing, and 50 g tip point mass

Of note in Figures 4.33 and 4.35, all cases with the same excitation frequency intersect the tip/root = 1 line at the same amplitude, regardless of changes in blade construction. This point corresponds to the first mode of the root torque to root pitch DF, and it represents rigid body motion (a flat, untwisted blade) with zero torque input. For the linearized blade, this occurs at 1 cycle/rev (i.e. cyclic frequency). Since this mode has no membrane deformation, its frequency is unaffected by blade construction, but it is affected by higher harmonics. This mode is not to be confused with the first mode of the root pitch to tip pitch DF, for which the first mode shape is a large tip amplitude and a large root torque with zero root motion (corresponding to the first zero

of the root torque to root pitch DF). Since there is a large twist deflection in this case, it is influenced by changes to the centrifugal stiffness, as was just shown. MacNeal originally derived that this mode occurs at $\sqrt{2}$ = 1.4 cycles/rev for the linearized model of a featureless, uniform membrane (see Table 4.2). This is close to the mode seen for the non-uniform (battened) nonlinear HELIOS blade in Figure 4.34. One can calculate the "rigid body" amplitude a priori for the nonlinear blade by balancing terms from the equations of motion.

Blade tip response to a root excitation is governed by the three terms of Eqs. (4.11) to (4.13): inertia, gyroscopic, and centrifugal. Below the first (rigid body) mode, the gyroscopic term is greater than the inertial term and the blade pitch amplitude decreases from root to tip, dubbed "wash-out". Above this mode, inertia dominates the gyroscopic term and the tip amplitude is higher than the root, dubbed "wash-in". Therefore, the rigid body mode frequency can be found by searching for the balance point between inertia and gyroscopic terms, a function of both excitation frequency and amplitude in the nonlinear system. Start with the first harmonic solution of Eqs. (4.42) & (4.43) at the blade root for a given $\omega_b \neq 0$:

$$\begin{aligned} \theta_1(\phi) &= \alpha_1^{(1)} \cos(\phi) \\ \ddot{\theta}_1(\phi) &= -\omega_b^2 \alpha_1^{(1)} \cos(\phi) \end{aligned} \tag{4.50}$$

and substitute into the root EOM of Eq. (4.11), assume that $\tau_1 = 0$ and $\theta_1 = \theta_2$ for flat plate motion, substitute $K^g = J\Omega^2$, and rearrange terms:

$$g\left(\phi, \alpha_1^{(1)}\right) \equiv \left(\frac{\omega_b}{\Omega}\right)^2 \alpha_1^{(1)} \cos(\phi) - \frac{1}{2} \sin\left[2\alpha_1^{(1)} \cos(\phi)\right] \tag{4.51}$$

which only has an explicit, non-zero solution for $\alpha_1^{(1)}$ when $\omega_b = 0$ (i.e. collective). For $\omega_b \neq 0$, g oscillates, and the flat blade solution is such that the first harmonic Fourier transform G is zero:

$$G\left(a_1^{(1)}\right) \equiv \int_0^{2\pi} g(\phi)\cos(\phi)\,d\phi \overset{?}{=} 0 \tag{4.52}$$

G can be thought of as a "wash factor" in that it is negative for wash-out and positive for wash-in. Furthermore, for all $\alpha_1^{(1)} > 0$ and $\omega_b \geq \Omega$, *G* is always positive, so excitation frequencies at or above cyclic always experience wash-in. For frequencies in the interval $\omega_b = (0, \Omega)$, like half-p, the rigid body mode amplitude $\alpha_1^{(1)}$ is found by iteration to set $G = 0$. Table 4.7 summarizes these results.

Table 4.7: Single-harmonic solution for first rigid-body mode amplitude

Pitch Profile	$\frac{\omega}{\Omega}$	$g(\phi)$	**Rigid-body mode for $\alpha_1^{(1)} \geq 0°$**	**Wash-out/-in (0°, 90°]**
Collective	0	$\sin\left[2\alpha_1^{(1)}\right]$	0°, 90°, 180°…	Wash-out < 90°
Half-p	0.5	$\alpha_1^{(1)}\cos(\phi) - 2\sin\left[2\alpha_1^{(1)}\cos(\phi)\right]$	0°, 83.8°	Wash-out < 83.8° Wash-in > 83.8°
Cyclic	1	$2\alpha_1^{(1)}\cos(\phi) - \sin\left[2\alpha_1^{(1)}\cos(\phi)\right]$	0°	Wash-in > 0°

This rigid-body mode is inherent in the single-harmonic dynamics, so no change in blade dimensions, mass distribution, or spin rate can change the amplitude/frequency combination at which it occurs; however, higher harmonic effects do play a factor for half-p. The balance point for half-p still represents the transition from wash-out to wash-in, but higher harmonics prevent true flat-plate motion. Figure 4.37 shows the half-p profile multi-harmonic solution for both the original and improved blades. The third harmonic is the only noteworthy contributor to half-p response, and it does not affect the balance point amplitude for the original, membrane ladder FEM (compare Figures 4.37a and 4.33). On the other hand, Figure 4.37b shows that higher harmonics combined with the improved blade design do shift the balance point slightly down to 72°, and more energy is transferred to the third harmonic. The response for the improved blade is so much smoother, though, that this makes little difference in practical application, as discussed in the next section.

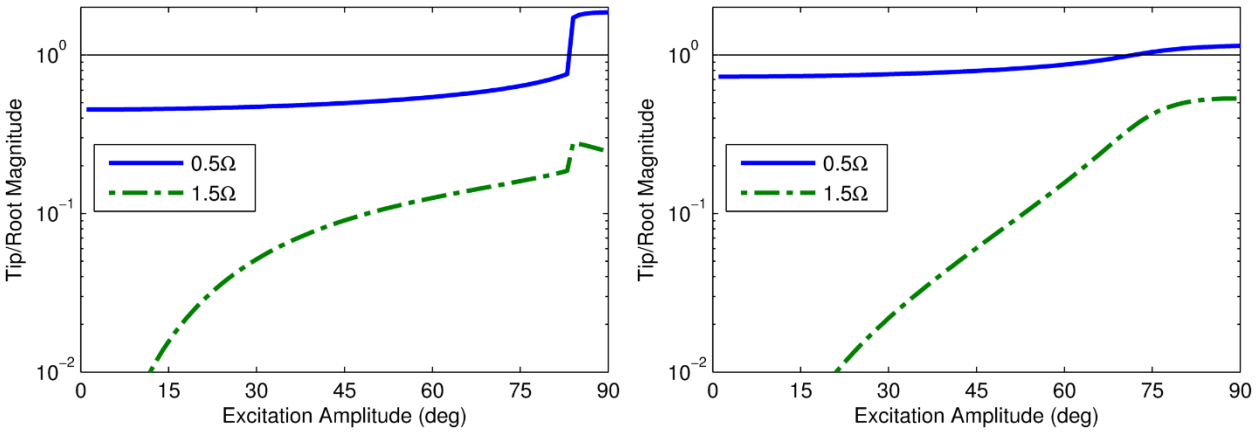

a) Membrane ladder FEM

b) 50 g edge reinforcing, 50 g tip point mass, rope ladder FEM

Figure 4.37: Root to tip amplitude for the half-p pitch profile, multi-harmonic solution

3. Root Control Law Performance with Multi-harmonic Solution

Heliogyros actuate the blades at frequencies very near the first structural mode, and traditional methods of providing acceptable tracking and stability margin (to increase the closed loop damping)—such as structural stiffening or loop gain reduction at modal frequencies—are not feasible. Lowered control gains improve settling time at the expense of root tracking because the root mechanical impedance reduction enables the root to absorb more modal energy. FF compensation provides one workaround by allowing for lower feedback gains, leading to faster settling times, while maintaining acceptable tracking. The FF signal for a root controller may be estimated using the harmonic expansion, but an infinite harmonic expansion is neither computationally possible nor necessary. Fortunately, fast Fourier transforms (FFT) of dynamic simulations of the operational modes of Table 1.5 show that over 99% of the power spectral density is captured in the 0^{th} to 4^{th} harmonic of half-p {0, 0.5, 1, 1.5, 2 cycles per rev}. This leads to the root control law:

$$\tau_1 = K_P\left(\theta_{ref} - \theta_1\right) + K_D\left(\dot{\theta}_{ref} - \dot{\theta}_1\right) + \frac{\alpha_\tau^{(0)}}{2} + \sum_{k=1}^{4} \alpha_\tau^{(k)} \cos(k\phi) + \sum_{k=1}^{4} \beta_\tau^{(k)} \sin(k\phi) \qquad (4.53)$$

Tracking without FF is especially problematic for collective profiles due to the constant restoring gyroscopic torque inducing wash-out. Consider the simulations in Figure 4.38 of a combined 38° collective & 20° cyclic pitch profile for attitude control during blade deployment (mode 1 in Table 1.5). Figure 4.38a shows the proportional-derivative (PD) controller performance with low gains optimized for rapid settling time, which result in poor tracking of the reference. On the other hand, Figure 4.38b uses the high gains required for acceptable tracking, but it takes four times longer to settle. As with the linear analysis, settling time is defined as the point at which the resulting SRP force (averaged over one revolution) changes <10% from one revolution to the next.

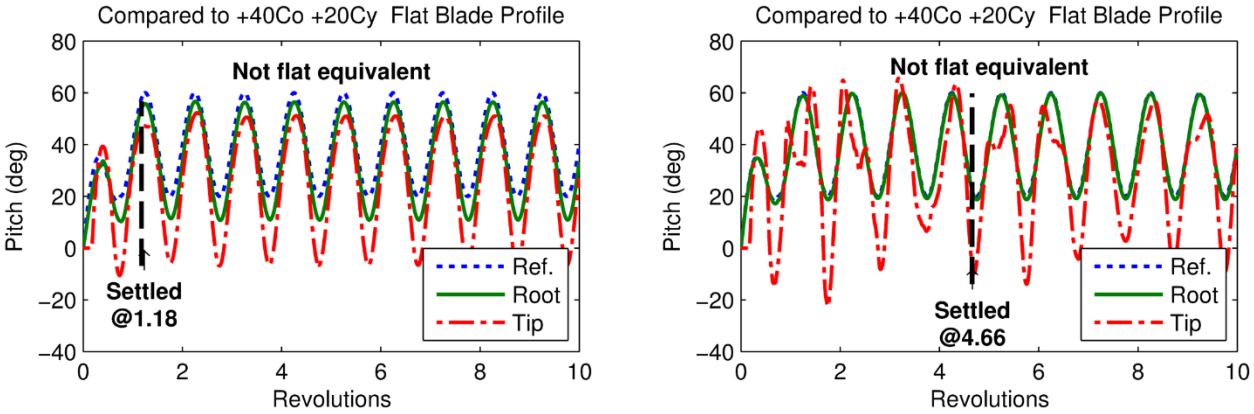

a) Low PD gains (0.002 Nm/rad & 0.01 Nms/rad) **b) High PD gains (0.02 Nm/rad & 0.1 Nms/rad)**

Figure 4.38: Dynamic simulation of rope ladder FEM with 50 g edge reinforcing, 50 g tip point mass, a PD root pitch controller, and 38° collective & 20° cyclic reference

Another problem is that in neither case is the blade "flat equivalent," defined as the time it takes for the net SRP force and moment components on the spacecraft to approach within 10% of the forces and moments generated by an ideal, flat blade with a given pitch profile. This metric is more relevant than settling time because it answers the question, "Is the flat blade assumption valid for attitude and trajectory analyses?" Herein, I manually adjust the root pitch profile so that the net effect of the flexible blade becomes flat-equivalent to the original profile requested by the attitude control law. Ideally, the attitude control tactics of Chapter 2 would incorporate the steady-

state harmonic expansion solution, allowing them to request the optimal root profile to achieve the desired effect with flexible blades. As discussed in Chapter 2, the inverse mapping from blade pitch profile to the resulting total-spacecraft force and moment vectors is challenging even with the flat blade assumption. It is likely that steady-state harmonic inverse solutions can be found with a similar approach, promising increased accuracy over a flat blade assumption. Furthermore, the harmonic expansion is simpler to implement for real-time attitude and trajectory control than the use of a full dynamic simulation approach, which would require iterative correction of reference pitch profiles based on settled simulation behavior.

Combining all of the measures discussed in this sub-chapter (edge reinforcing, tip mass, low PD gains, FF compensation, and root profile adjustment) yields a system that rapidly settles and generally approximates a flat blade within 10%. Figure 4.39 incorporates both the FF compensation and the root profile adjustment for operational mode 1 of Table 1.5. The flexible-blade, root pitch profile becomes 43° collective & 17° cyclic, which generates the forces and moments equivalent to a flat blade profile of 38° collective & 20° cyclic within 1.6 revolutions. Notice the excellent tracking of the root to the reference signal and rapid settling time in Figure 4.39a with the PDFF controller. Figure 4.39b shows the FFT of the blade tip for the last five revolutions of the 10 rev simulation to find the harmonic frequencies excited by the given root profile. I set the simulation time step so that the FFT has a frequency resolution of 1/6 cycles/rev. Note that the zero-frequency FFT coefficient must be halved per Eq. (4.46) to equal the collective pitch. It is apparent in Figure 4.39b that the blade's natural response has decayed, since only harmonics of the forced response remain. This FFT is useful for validating the harmonic expansion methodology by direct comparison with the expansion's tip coefficients.

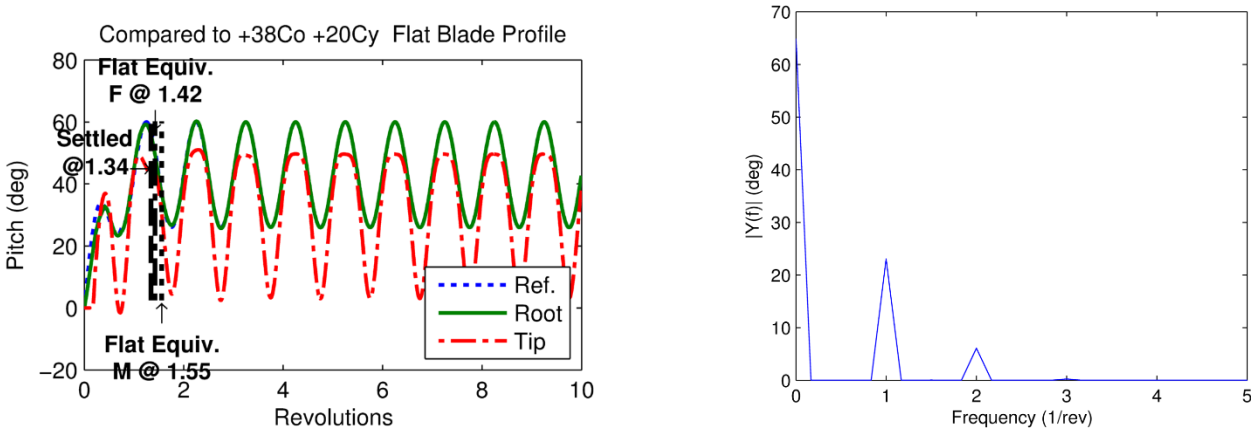

a) Dynamic simulation **b) FFT of tip response for the last five revolutions**

Figure 4.39: Rope ladder FEM with 50 g edge reinforcing, 50 g tip point mass, a PDFF root pitch controller, low PD gains, and 43° collective & 17° cyclic reference

Table 4.8 gives the performance results and validation for all the operational modes of Table 1.5, each of which settles within three revolutions (column 5). The flexible blade profiles (column 3) required to achieve flat blade equivalence (column 4) are usually only a few degrees away from the desired flat blade profile (column 2). The difference adjusts for wash-out/-in so that the controller usually achieves the desired forces and moments in a few revolutions. The blade settles quickly enough to actuate several pitch profiles per orbit, even in low Earth orbit (LEO). The last three columns list the dominant harmonics at the blade tip in each mode (column 6), the FFT coefficients measured after the blade had settled in a dynamic simulation (column 7), and the harmonic expansion coefficient magnitude calculated using the analytical procedure of Chapter 4.E.1 (last column). These columns validate the harmonic expansion methodology, as the harmonic coefficients are in near-perfect agreement with the FFT from the dynamic simulation. Furthermore, it justifies the limitation of the expansion to harmonic numbers 0 to 4 when exciting the blade at up to two frequencies (i.e. half-p and cyclic), as no operational mode significantly excites frequencies above 2 cycles/rev ($k = 4$).

Table 4.8: PDFF root controller performance at the common operational modes of Table 1.5

#	Flat Blade Profile	Flexible Blade Profile	Flat Blade Equivalence (rev)	Settling Time (rev)	k^*	Tip FFT (deg)†	$\left\|\alpha_{tip}^{(k)}, \beta_{tip}^{(k)}\right\|$ (deg)†
1	38° collective 20° cyclic	43° collective 17° cyclic	Force: 1.4 Moment: 1.6	1.3	0 2 4	32.4 23.1 6.1	32.4 23.1 6.1
2	70° half-p	70° half-p	F: No, 20% higher M: No, 23% higher	1.8	1 3	68.4 22.4	68.1 22.0
3a	40° cyclic	37° cyclic	F: 1.5 M: 3.7	1.7	2	41.2	41.3
3b	90° collective 60° cyclic	90° collective 34° cyclic	F: 1.9 M: 3.1	2.2	0 2	90.0 78.6	90.0 79.1
4/ 5a/ 5b	60° half-p -17° cyclic	67° half-p -10° cyclic	F: 2.6 M: No, 23% higher	1.8	0 1 2 3 4	3.0 63.9 15.8 18.0 9.7	2.9 63.8 15.7 17.7 9.6
5b	40° collective 52° cyclic	45° collective 40° cyclic	F: No, 27% lower M: No, 25% lower	1.3	0 2 4	41.9 62.0 22.0	42.2 62.4 21.8
6	70° half-p 52° cyclic	56° half-p 35° cyclic	F: 2.2 M: 3.6	2.3	0 1 2 3 4	6.1 58.4 57.3 19.1 18.6	6.0 58.4 57.5 18.7 18.7

*These are the harmonics of half-p ($\omega_b = 0.5\Omega$) that capture >99.5% of the tip response's power spectrum.
†Coefficients of the 0th harmonic have been halved per Eq. (4.46) for easy comparison with collective input.

The higher harmonics can either help or hurt the net force and moment generated. The only mode where the flexible blade cannot meet or exceed the flat blade force and moment performance is mode 5b (rapid slewing) with collective & cyclic. Fortunately, this mode has an alternative profile using half-p & cyclic that outperforms the flat blade. Cyclic by itself (mode 3) does not excite higher harmonics, but collective & cyclic (modes 1 & 5b) always excites $k = 4$, the 2nd harmonic of cyclic. This harmonic is apparent in Figure 4.39a by observing that the blade tip

spends more time at high pitch angles where less SRP is reflected and vice versa at low sun angles, thus lowering the net force. On the other hand, the half-p profile (modes 2, 4 & 6) always excites its 3rd harmonic, which generally improves the performance of this profile. Looking at the simulation of mode 4 in Figure 4.40a, one can see the 3rd harmonic causes the blade to spend more time at low pitch and less at high pitch, thus increasing the available SRP thrust. The spacecraft's high sun angle during emergency attitude recovery (mode 6) lessens this effect. As might be expected with two excitation frequencies, all five harmonics are only significant in half-p & cyclic profiles (modes 4 & 6). The FFT in Figure 4.40b confirms that these five harmonics and no others are significant for approximating the steady-state dynamics.

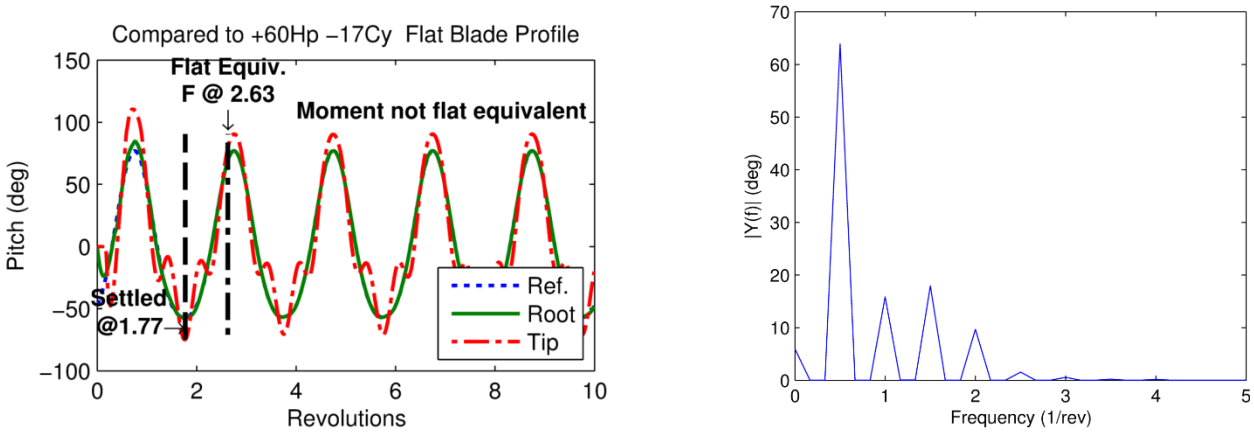

a) Dynamic simulation **b) FFT of tip response for the last five revolutions**

Figure 4.40: Rope ladder FEM with 50 g edge reinforcing, 50 g tip point mass, a PDFF root pitch controller, low PD gains, and 67° half-p & 10° cyclic reference

F. Chapter Summary and Recommendations

A frequency domain analysis reveals the essential nature of feedback control of blade twist using a root actuator: a blade with zero material damping cannot be stabilized by a root control system with finite bandwidth. Fortunately, the material damping required is extremely small (<0.001% at the second mode). Additionally, the first mode represents rigid body motion with this free-free system using a torque-source root motor. This mode always has a response magnitude greater than one and must be phase-stabilized. This requires a controller bandwidth of

at least 1 cycle/rev (0.0167 Hz). A detailed examination of the tradeoff between material damping and controller bandwidth reveals that the closed-loop frequency response peaking can be kept under 5dB at the root and 10dB at the tip with bandwidths of 30 cycles/rev (0.5 Hz) even at extremely small levels of blade material damping (<0.001% at the second mode). The system time-constants are so long that even very small controller bandwidths (when measured in Hertz) yield an acceptable dynamic response.

Should further analysis prove that additional damping is necessary, I evaluate a reflectivity control approach similar to that pioneered with the JAXA IKAROS solar sail as a means of controlling dynamic torsional responses at the tip caused by root pitch inputs. I found IKAROS-like RCDs capable of attenuating blade torsional response, but they almost double the spacecraft mass so are impractical. Torsional control performance could be improved over 200% by a combination of halving RCD thickness and doubling the difference in on/off reflectivity. Unfortunately, single-sensor configurations for feedback destabilize the mid-frequency modes. A distributed sensing system solved this problem, but this arrangement may be impractical.

I also conducted experiments to determine the frequency response of a hanging membrane blade in a vacuum chamber, yielding three key results. First, they quantified the coupling between blade twist and flap motion. Some damping of bending motion may be required to mitigate this problem. Second, the experiments validated the membrane ladder FEM. In fact, the first four experimental and theoretical mode frequencies agreed within 8.4% for twist motion and 4.5% flapwise bending. Lastly, the experiment attempted to estimate the magnitude and character of the material damping, but the damping ratios were much higher than expected. The first mode experienced 5.1% damping in flap and 17.5% in twist. Some of that damping was due to viscous effects still present in the evacuated test chamber, although it is difficult to say how much from

these experiments. Further testing at lower pressures is required to isolate the membrane's material damping. The damping ratios decreased with frequency in a roughly linear fashion, which is opposite the behavior of the current damping model in the FEM. Other methods of modeling damping should be investigated.

Lastly, this chapter investigated the nonlinear blade twist dynamics and control. I first solved the EOM using a Fourier series harmonic expansion for the blade's steady-state response. I used this steady-state solution to explore some dynamic concerns and to improve the blade pitch controller. The heliogyro blade is so flexible that normal operations excite the blade very near the first structural twist mode, and settling time goals preclude traditional controller gain stabilization. Furthermore, spacecraft acceleration goals preclude the addition of massive structural stiffening. Unfortunately, this can lead to an unacceptable twist response in membrane blades. For example, the blade can twist completely around under cyclic excitation of as little as 35° root amplitude. Therefore, it is necessary to increase blade stiffness by enhancing the centrifugal stiffness arising from blade tension. I found two blade construction alterations to improve centrifugal stiffness with marginal mass penalty: a point mass at the blade tip and directing the tension along the blade edges (e.g. by edge reinforcement). The latter was found to be more mass-efficient. With these modifications, additional blade tip control has not been found necessary for reasonable tip/root pitch ratios (using the blade twist-only dynamics).

Feed-forward greatly improves blade root controller tracking and settling time performance, and the steady-state solution by harmonic expansion is an effective way to calculate the nonlinear (amplitude-dependent) feed-forward coefficients. Half-p and cyclic pitch profiles excited harmonics up to 2 cycles/rev with less than 0.5% of the steady-state response's power spectrum above this frequency. Therefore, incorporating frequencies beyond this into the feed-

forward signal is unnecessary. A PDFF control law settles blade motion within 3 revolutions, which is only 3 minutes given a nominal 1 RPM spin rate. Therefore, assuming instantaneous changes to the blade pitch profile would be a reasonable simplification for preliminary attitude and trajectory analyses. Even in LEO, where the orbit period is a relatively short 100 minutes, the heliogyro could vary the pitch profile effectively many times per orbit. The flat-blade assumption is generally reasonable for preliminary attitude and trajectory analyses, but higher harmonics arising naturally can either increase or decrease propulsion and attitude control performance by as much as 25%.

CHAPTER 5. CONCLUSION

A. Contributions to the Field

Heliogyros have the potential to significantly enhance and enable our exploration of the solar system. I have shown how they can generally double acceleration performance over most well-developed solar sail architectures for near- and mid-term missions. The heliogyro truly surpasses other architectures for far-term missions due to its superior scalability to vast areas. These significant benefits come at the cost of increased complexity in the attitude, orbital, and structural dynamics. I have investigated the most significant control issues at each of these scales and developed methods to estimate performance along with several control approaches which should prove useful to future mission designers.

1. Attitude Control Tactics

I performed the first detailed investigation into the use of heliogyro blade pitch profiles to generate attitude control moments from all orientations. I quantified the change in attitude control moments with varying sun angle for a given pitch profile. Then, I determined that a cyclic profile would correct for these changes and restore the desired force and moment direction. Significantly, I developed three tactics optimized to perform attitude stabilization concurrently with one of three other common goals: controlling the heliogyro spin rate, changing the sun angle by spin axis precession, or generating thrust perpendicular to the sun line. These three tactics each combine two canonical pitch profiles, cover all of the most common mission operational modes, and can perform each of the other two functions to a lesser degree.

I quantified each of these tactics' maximum ability to create attitude control moments at all orientations, i.e. their control moment authority. Startlingly, the heliogyro was found capable of achieving and recovering from any orientation as long as the blades are permitted to be

illuminated from either side. Allowing the blades to be illuminated on both sides turned out to be useful in many circumstances, so performance expectations will need to be cut should other considerations prevent this. The control moment authority is useful for estimating the heliogyro's maximum slew rate, and therefore which trajectories it is capable of following. I also compared the tactics' slew rates and lateral thrust capability to determine which tactic is preferred for which mission operational mode.

Lastly, I developed a methodology for determining the pitch profile required to achieve a desired attitude control moment. This represents the inverse of the forward mapping from a given pitch profile to the resulting forces and moments, which is highly nonlinear with many local minima. Through visual inspection and linear regression, I determined the basic topology of this mapping that I then used as an approximate inverse mapping. I also came up with a methodology for determining the exact inverse mapping with a gradient descent optimizer. This work forms the basis of an operational attitude control system that automatically varies the blade pitch to provide a desired moment to control attitude.

2. Orbital Performance for Earth Escape Strategies

Earth escape is the most difficult regime near-term solar sails will face because it requires that the thrust vector be slewed at orbit rates. I implemented a metric, dubbed the "escape factor," for quantifying a given escape strategy's performance without performing full orbital dynamics simulations. This is the first application of this metric to heliogyros, the first direct comparison of heliogyro and kite sail escape performance, and the first to account for the incumbent reduction in thrust when attempting to slew the heliogyro 180° per orbit as required by the ideal, flat sail trajectories. I also developed a new escape strategy specific to the heliogyro that maximized thrust along the velocity vector and improved upon canonical heliogyro strategies by up to 17%. Finally,

I validated these performance estimates by deriving a method of calculating the escape factor from simulation results and then simulating several of the strategies. This method of measuring the escape factor from simulation results is generally applicable to low-thrust trajectories, so it could be used to compare a variety of architectures' performance. This work showed that the heliogyro is 87% as capable as the ideal, flat solar sail of the same characteristic acceleration. Since the heliogyro can usually double the characteristic acceleration versus a kite sail of the same mass, the performance benefits of the heliogyro, even in this most difficult regime, are clear.

3. Structural Dynamics and Control of Blade Twist

I spent the bulk of my efforts investigating blade twist dynamics, as this poses the biggest concern into heliogyro feasibility. To do this, I developed a new finite element model of heliogyro blade torsional dynamics called the membrane ladder. This model has fewer degrees of freedom than commercial FEA software, but it is useful for gaining insight into blade dynamics, allows for closed loop feedback control, is more accessible to analytical analysis, and requires orders of magnitude less computer power. The membrane ladder improved upon previous heliogyro blade twist models[9,12,51,53] by allowing for discrete blade masses, such as battens, and multiple tension stress distributions.

The linearized membrane ladder is easily formulated in state space, making it accessible to classical linear controls analysis. This thesis was the first development of a closed-loop root controller employing feed forward for improved tracking and settling times. It also was the first investigation of the stability of a finite bandwidth controller and its relationship to the blade's material damping. I found that controller bandwidths of 30 cycles/rev (0.5 Hz for HELIOS) should provide sufficient stability margin for all reasonable material damping levels.

I performed the first investigation into the potential for using IKAROS' novel reflectivity control as a blade tip actuator. Root control appears sufficient thus far, but other factors, such as coupling of blade motion, may necessitate tip control. I found the IKAROS' technology to be impractical, but it could be useful should a halving of thickness and doubling of the reflectivity change be possible. The reflectivity control system would be distributed over an area, so non-colocation with a single sensor could destabilize some modes. I found that distributed sensing would solve this problem, but this may be impractical.

The structural dynamics experiments on a hanging heliogyro blade at 1 gravity were the first experimental validation of the heliogyro blade models and the first estimation of the blade's material damping. The experimental FRFs agreed very well with the membrane ladder model out to the fifth structural mode. The measured damping was much higher than expected at a few percent, so further experiments at pressures lower than 50 mTorr are recommended. Lastly, some coupling between flap and twist was identified, but it did not significantly alter mode frequencies and should be damped by the root control system.

While linear stability is a prerequisite for nonlinear stability, nonlinear effects were found to significantly worsen the blade's twist response at moderate excitation amplitudes. This was the first investigation of heliogyro blade nonlinear dynamics, and I developed quantitative predictions of the steady-state response to a given root excitation. By looking at this steady-state solution, I determined that the cause is a down-shift in the first mode frequency with excitation amplitude. I identified increasing the centrifugal stiffness as the primary means of increasing the mode frequencies, thereby moderating and flattening the blade's twist response. The most effective ways to do this are by edge reinforcing to carry the blade stress on the leading and trailing edges and adding a point mass to the blade tip. I also identified frequency coupling that excited higher

harmonics, but that this response is 99.5% confined to only five frequencies: 0 (collective), 0.5 (half-p), 1 (cyclic), 1.5 (3^{rd} harmonic of half-p), and 2 (2^{nd} harmonic of cyclic) cycles/rev. The steady-state solution was also effective for providing the root motor controller feed-forward signal for enhanced tracking and faster settling times. In fact, the blade settled within two to three minutes for all expected blade pitch profiles. Furthermore, with the enhanced centrifugal stiffening, the blade generally approximated the SRP forces and moments of a flat blade, making this a reasonable assumption for preliminary attitude and orbital dynamics analysis. Surprisingly, the naturally arising third harmonic of half-p actually improved force and moment performance by as much as 25%.

B. Future Work

The `HGForce` algorithm to map pitch profiles to their resulting forces and moments of Chapter 2 currently assumes flat blades. This algorithm should be improved by incorporating the nonlinear, multi-harmonic, steady-state solution of blade shape from Chapter 4.E.1. Furthermore, the blade root pitch profile of Eq. (2.1) should include two more terms (for a total of nine pitch profile parameters) to capture all five of the principal flexible blade harmonic frequencies and phases. These two modifications would ensure that the inverse mapping is returning the pitch profile for a flexible blade to optimally meet the desired force and moment vectors. The mapping inversion of `HGForce` for the three attitude control tactics presented here is limited to three inputs and the three moment component outputs. This could be expanded into a more general optimization of the total force and moment vector for any giving pitch profile. As an intermediate step, it would be beneficial to investigate how to optimally create a force in any given direction from any orientation without inducing attitude moments.

I have not found any orbit simulation and trajectory optimization software that adequately accounts for the heliogyros' unique capabilities and limitations. This includes JPL's Mystic & Malto, MSFC's Solar Sail Spaceflight Simulation Software (S5), Princeton Satellite Systems' Solar Sail Toolkit for Matlab, JSC's Copernicus, and Analytical Graphics Incorporated's (AGI) Systems Toolkit (STK). In particular, no system accounts for the reduction in thrust that occurs when a heliogyro diverts some SRP to generate attitude control moments for slewing. Short of building a tool from scratch, one option is to write a custom force model that integrates with currently available software and is called during each integration step. The open development of general solar sail trajectory optimization tools that are versatile, customizable, powerful, and user-friendly (i.e. incorporates a GUI) is another area of investment greatly beneficial to all solar sailors.

I assume blade pitch is controlled by a torque-source root motor in this thesis, but the torques required are extremely small (<1 μNm for HELIOS). Such small torques would generally be overwhelmed by friction forces in conventional electromagnetic motors. Therefore, detailed root actuation mechanical design is needed that takes friction into account. The motor would either need to significantly reduce friction or the control system would have to accommodate a geared, position source root motor with high impedance. The latter would require measurement and feedback of a parameter other than root pitch, which raises other measurement and non-colocation difficulties.

Lastly, structural dynamics simulations will never be fully convincing until they are coupled with attitude dynamics in a total spacecraft model. This simulation would need to be nonlinear, have many nodes per blade, allow three DOF motion at all nodes, incorporate experimental measurements of material elasticity & damping, incorporate a realistic SRP model, and implement a blade pitch controller nested within an attitude control law in a free-floating,

unconstrained, inertial reference frame. Such a simulation would address concerns about the inability to ground test.

These investigations are key to further understanding and optimizing the heliogyro, but I do not foresee them uncovering any show stoppers to implementing the heliogyro. I have investigated key concerns with practical heliogyro operations and not found any insurmountable roadblocks nor any recommended design modifications that would negate the substantial performance gains afforded by this architecture.

REFERENCES

[1] Adeli, S.N., Theodorou, T. & Lappas, V., "Ground Demonstration of a Solar Sail Attitude Control Actuator," *AIAA Guidance, Navigation, and Control Conference*. AIAA 2010-8071, 2-5 August 2010, Toronto, Canada. doi: 10.2514/6.2010-8071

[2] Adeli, S.N., Lappas, V.J. & Wie, B., "A Scalable Bus-Based Attitude Control System for Solar Sails," *Advances in Space Research*, Vol. 48, No. 11, 2011, pp.1836–1847. doi: 10.1016/j.asr.2011.08.024

[3] Alhorn, D. C., et al, "NanoSail-D: The Small Satellite That Could!" *25th AIAA/USU Conference on Small Satellites*, SSC11-VI-1, 2011.

[4] Barnes, Nathan, "Sunjammer Solar Sail Demonstration," *5th Gossamer Workshop*, 7 June 2012, Tustin, CA.

[5] Barnes, N. C., Derbes, W. C., Player, C. J., and Diedrich, B. L., "Sunjammer: A Solar Sail Demonstration," *Advances in Solar Sailing*, Springer, Berlin, 2014, pp. 115–126. doi: 10.1007/978-3-642-34907-2_8

[6] Biddy, C., and Svitek, T. "LightSail-1 Solar Sail Design and Qualification," *Proceedings of the 41st Aerospace Mechanisms Symposium*. Pasadena, CA, 2012.

[7] Blomquist, R., "Design Study of a Solid-State Heliogyro Solar Sail," M.S. thesis, Massachusetts Institute of Technology, Cambridge, MA, September 1990.

[8] Blomquist, R., "Solar Blade Nanosatellite Development: Heliogyro Deployment, Dynamics, and Control," *13th AIAA/USU Conference on Small Satellites*, 1999.

[9] Blomquist, R. S., "Heliogyro Control," Ph.D. Dissertation, The Robotics Institute, Carnegie Mellon University, Pittsburgh, PA, 2009.

[10] Bookless, J., McInnes, C., "Control of Lagrange point orbits using solar sail propulsion," *Acta Astronautica*, Vol. 62, No. 2-3, 2008, pp.159–176. doi: 10.1016/j.actaastro.2006.12.051

[11] Borggräfe, A., Heiligers, J., Ceriotti, M., and McInnes, C. R., "Distributed Reflectivity Solar Sails for Extended Mission Applications," *Advances in Solar Sailing*, Springer, Berlin, 2014, pp. 331-350. doi: 10.1007/978-3-642-34907-2_22

[12] Botter, T., Coverstone, V. L., and Burton, R. L., "Structural Dynamics of Spin-Stabilized Solar Sails with Applications to Ultrasail," *Journal of Guidance, Control, and Dynamics*, Vol. 31, No. 2, March-April 2008, pp. 402-413. doi: 10.2514/1.27609.

[13] Burton, R. et al, "UltraSail – Ultra-Lightweight Solar Sail Concept," *41st AIAA/ASME/SAE/ASEE Joint Propulsion Conference & Exhibit*, AIAA 2005-4177, 10-13 July 2005, Tucson, Arizona. doi: 10.2514/6.2005-4117

[14] Burton, R., et al, "Initial Development of the Cubesail/Ultrasail Spacecraft," *Joint Army Navy NASA Air Force (JANNAF) Spacecraft Propulsion Subcommittee Meeting*, Colorado Springs, Colorado, May, 2010.

[15] Cantrell, J., and Friedman, L., "Lightsail 1 – Flying for Less," *Proceedings of the Second International Symposium on Solar Sailing*, New York, NY, 2010.

[16] Dachwald, B., "Optimization of Interplanetary Solar Sailcraft Trajectories Using Evolutionary Neurocontrol," *AIAA Journal of Guidance, Control, and Dynamics*, Vol. 27, No. 1, 2004, pp.66–72. doi: 10.2514/1.9286.

[17] Dachwald, B., Ohndorf, A., Wie, B., "Solar Sail Trajectory Optimization for the Solar Polar Imager (SPI) Mission," *AIAA/AAS Astrodynamics Specialist Conference and Exhibit*, 21-24 August 2006, Keystone, CO, AIAA 2006-6177. doi: 10.2514/6.2006-6177.

[18] Farrés, A., Jorba, À., "Periodic and quasi-periodic motions of a solar sail close to SL 1 in the Earth–Sun system," *Celestial Mechanics and Dynamical Astronomy*, Springer Science, Vol. 107, No. 1-2, 2010, pp.233–253. doi: 10.1007/s10569-010-9268-4.

[19] Farrés, A., Jorba, À., "Dynamics of a solar sail near a Halo orbit," *Acta Astronautica*, Vol. 67, No. 7-8, 2010, pp.979–990. doi: 10.1016/j.actaastro.2010.05.022.

[20] Flotow, A. H., "A Traveling Wave Approach to the Dynamic Analysis of Large Space Structures," *24th AIAA Structures, Structural Dynamics, and Materials Conference*, 1983, AIAA-1983-964-125. doi: 10.2514/6.1983-964

[21] Friedman, L., et al, "Solar Sailing—The Concept Made Realistic," *AIAA 16th Aerospace Sciences Meeting*, Huntsville, AL, 16–18 January 1978. doi: 10.2514/6.1978-82

[22] Friedman, L., "Solar Sailing Development Program (FY 1977) Final Report Vol. I," Report 720–9, Jet Propulsion Laboratory, 30 January 1978.

[23] Fu, B., and Eke, F. O., "Attitude Control Methodology for Large Solar Sails," *AIAA Journal of Guidance, Control, and Dynamics*, Vol. 38, No. 4, 2014, pp. 662-670. doi: 10.2514/1.G000048

[24] Funase, R., et al., "On-orbit Verification of Fuel-Free Attitude Control System for Spinning Solar Sail Utilizing Solar Radiation Pressure," *Advances in Space Research*, Vol. 48, No. 11, 2011, pp. 1740–1746. doi: 10.1016/j.asr.2011.02.022

[25] Geppert, U., Biering, B., Lura, F., Reinhard, R., "The 3-step DLR-ESA Gossamer Road to Solar Sailing," *2nd International Symposium on Solar Sailing*, New York, NY, July 20-22, 2010, published in *Advances in Space Research*, Elsevier, Vol. 48, No. 11, 2011, pp. 1695-1701, doi: 10.1016/j.asr.2010.09.016

[26] Gibbs, S., Dowell, E., "Solarelastic Stability of the Heliogyro," *Advances in Solar Sailing*, pp. 661-665, Springer-Praxis, Springer Berlin Heidelberg, 2014. doi: 10.1007/978-3-642-34907-2_40

[27] Gibbs, S. C., "Stability of Beams, Plates and Membranes due to Subsonic Aerodynamic Flows and Solar Radiation Pressure" Ph.D. Dissertation, Department of Mechanical Engineering and Materials Science, Duke University, NC, 2014.

[28] Gong, S., Baoyin, H., Li, J., "Solar Sail Three-Body Transfer Trajectory Design," *AIAA Journal of Guidance, Control, and Dynamics*, Vol. 33, No. 3, 2010, pp.873–886. doi: 10.2514/1.46077

[29] Guerrant, D., Wilkie, W. K., Lawrence, D, "Heliogyro Blade Twist Control via Reflectivity Modulation," *13th AIAA Gossamer Systems Forum*, AIAA 2012-1746, Honolulu, Hawaii, 23-26 April, 2012. doi: 10.2514/6.2012-1746

[30] Guerrant, D., Lawrence, D., Wilkie, W. K., "Performance of a Heliogyro Blade Twist Controller with Finite Bandwidth," *AIAA/AAS Astrodynamics Specialist Conference*, AIAA 2012-4661, Minneapolis, MN, 13-16 August 2012. doi: 10.2514/6.2012-4661

[31] Guerrant, D. and Lawrence, D., "Heliogyro Solar Sail Blade Twist Stability Analysis of Root and Reflectivity Controllers," *AIAA Guidance, Navigation and Control Conference*, AIAA 2012-4842, Minneapolis, MN, 13-16 August 2012. doi: 10.2514/6.2012-4842

[32] Guerrant, D. and Lawrence, D., "Heliogyro Attitude Control Moment Authority via Blade Pitch Maneuvers," *3rd International Solar Sail Symposium*, Glasgow, UK, June 11-13, 2013, published in *Advances in Solar Sailing*, Springer, Berlin, 2014, pp. 667-686. doi: 10.1007/978-3-642-34907-2.

[33] Guerrant, D., Lawrence, D., Heaton, A., "Earth Escape Capabilities of the Heliogyro Solar Sail," *Advances in the Astronautical Sciences: Proceedings of the AAS/AIAA Astrodynamics Specialist Conference*, Hilton Head, SC, 11-15 August 2013, Vol. 150, AAS 13-743, American Astronautical Society, Washington, DC, 2014, pp. 639-658.

[34] Guerrant, D., Lawrence, D., "Nonlinear Torsional Dynamics and Control of Heliogyro Solar Sail Blades," *2nd AIAA Spacecraft Structures Conference*, Kissimmee, FL, 5-9 January 2015. doi: 10.2514/6.2015-0435.

[35] Guerrant, D., Lawrence, D., "Tactics for Heliogyro Solar Sail Attitude Control via Blade Pitching," *AIAA Journal of Guidance Dynamics and Control*, [accepted for publication 9 February 2015]. doi: 10.2514/1.G000861.

[36] Hargens-Rysanek, J., Coverstone, V. L., and Burton, R. L., "Orbital Precession Via Cyclic Pitch for the UltraSail System," *Advances in the Astronautical Sciences*, Vol. 127, 2007, pp. 1009-1028.

[37] "Heliogyro Preliminary Design, Phase II Final Report," NASA Contractor Report CR–157128, MacNeal-Schwendler Corp., January 1978.

[38] Huang, Y.-R., Juang, J.-N., Hung, C.-H., and Wilkie, W. K., "Dynamics of a Coupled Pendulum Model of a Heliogyro Membrane Blade," *Advances in Solar Sailing*, Springer, Berlin, 2014, pp. 687-704. doi: 10.1007/978-3-642-34907-2_42

[39] Johnson, L., Young, R., Barnes, N., Friedman, L., Lappas, V., and McInnes, C., "Solar Sails: Technology and Demonstration Status," International Journal of Aeronautical & Space Science, Vol. 13, No. 4, pp 421-427, 2012. doi:10.5139/IJASS.2012.13.4.421

[40] Johnson, L., Young, R., Montgomery, E., Alhorn, D., "Status of Solar Sail Technology within NASA," *Advances in Space Research*, Vol. 48, 2011, pp. 1687-1694. doi:10.1016/j.asr.2010.12.011.

[41] Johnson, L., et al., "NanoSail-D: A Solar Sail Demonstration Mission," *Acta Astronautica*, Vol. 68, No. 5-6, 2011, pp. 571-575. doi: 10.1016/j.actaastro.2010.02.008

[42] Juang, Jer-Nan. Applied System Identification. Englewood Cliffs, NJ, Prentice Hall, 1994.

[43] Juang, Jer-Nan, Horta, Lucas, and Phan, Minh, System/Observer/Controller Identification Toolbox User's Guide, NASA Langley Research Center, May 2000.

[44] Juang, J.-N., Lu, H.-H., Horta, L. G., and Wilkie, W. K., "Challenges Associated with System Identification and Control of a Heliogyro Membrane Blade," *Advances in Solar Sailing*, Springer, Berlin, 2014, pp. 705-716. doi: 10.1007/978-3-642-34907-2_43

[45] Kryloff, N., Bogoliuboff, N., *Introduction to Non-Linear Mechanics*, Princeton University Press, Princeton, NJ, 1947

[46] Lappas, V., Adeli, N., Visagie, L., Fernandez, J., Theodorou, T., Steyn, W., Perren, M. "Cubesail: A Low-Cost Cubesat-Based Solar Sail Demonstration Mission," *Advances in Space Research*, Vol. 48, No. 11, 2011, pp. 1890-1901. doi: 10.1016/j.asr.2011.05.033

[47] Liewer, P. C., et al., "Solar Polar Imager: Observing Solar Activity from a New Perspective," NASA Vision Mission Study Final Report JPL D-33704, December, 2005, Pasadena, CA. doi: 10.2514/5.9781600866920.0001.0040

[48] Lisano, M. Lawrence, D., and Piggot, S., "Solar Sail Transfer Trajectory Design and Stationkeeping Control for Missions to the Sub-L1 Equilibrium Region," *15th AAS/AIAA Space Flight Mechanics Conference*, Copper Mountain, Colorado, January 23-27, 2005.

[49] Macdonald, M., McInnes, C., "Realistic Earth Escape Strategies for Solar Sailing," *AIAA Journal of Guidance, Control, and Dynamics*, Vol. 28, No. 2, 2005, pp.315–323. doi: 10.2514/1.5165.

[50] MacDonald, M., McInnes, C., "Solar Sail Science Mission Applications and Advancement," *Advances in Space Research*, Vol. 48, No. 11, 2011, pp. 1702-1716, doi: 10.1016/j.asr.2011.03.018

[51] MacNeal, R. H., "The Heliogyro: An Interplanetary Flying Machine," NASA Contractor's Report CR 84460, June 1967.

[52] MacNeal, R. H., Hedgepeth, J. M., Schuerch, H. U., "Heliogyro Solar Sailer Summary Report," NASA Contractor's Report CR–1329, Astro Research Corporation, June 1969.

[53] MacNeal, R. H., "Structural Dynamics of the Heliogyro," NASA CR–17445A, 1971.

[54] MacNeal, R. H. and Hedgepeth, J. M., "Helicopters for Interplanetary Space Flight," *34th National Forum of the American Helicopter Society*, Washington, D. C., May 1978.

[55] Martin, V., Williams, J., Senent, J., "Copernicus User Guide," NASA Johnson Space Center, Revision 2, October 14, 2011.

[56] McInnes, Colin R., Solar Sailing: Technology, Dynamics and Mission Applications, 1st ed., Springer-Praxis, Chichester, UK, 1999. doi: 10.1007/978-1-4471-3992-8

[57] Miyazaki, Yasuyuki, et al., "Conserving Finite Element Dynamics of Gossamer Structures and Its Application to Spinning Solar Sail IKAROS," *52nd AIAA/ASME/ASCE/AHS/ASC Structures, Structural Dynamics and Materials Conference*, 4–7 April 2011, Denver, Colorado. doi: 10.2514/6.2011-2181

[58] Mu, J., Gong, S. and Li, J., "Coupled Control of Reflectivity Modulated Solar Sail for GeoSail Formation Flying," *AIAA Journal of Guidance, Control, and Dynamics*, April 2014. doi: 10.2514/1.G000117

[59] Price, H., Ayon, J., Garner, C., Klose, G., Mettler, E., Sprague, G., "Design for a solar sail demonstration mission," *Space Technology and Applications International Forum (STAIF-2001)*, Feb 11, 2011, Albuquerque, NM, http://hdl.handle.net/2014/12303.

[60] Scholz, C., Romagnoli, D., Dachwald, B., and Theil, S., "Performance Analysis of an Attitude Control System for Solar Sails Using Sliding Masses," *Advances in Space Research*, Vol. 48, No. 11, 2011, pp. 1822–1835. doi: 10.1016/j.asr.2011.05.032

[61] Soop, E. M., *Handbook of Geostationary Orbits*, Space Technology Library, Springer, Netherlands, 1994, pp. 111. doi: 10.1007/978-94-015-8352-7

[62] "Solar Sail Technology Readiness Report," Jet Propulsion Laboratory Report 720–1, 18 July 1977.

[63] Tajima, K., Hotta, H., Yamada, Y., Okada, M., Yoshimura, K., "Electrochromic switchable mirror foil with tantalum oxide thin film prepared by reactive DC magnetron sputtering in hydrogen-containing gas," *Surface & Coatings Technology*. Vol. 205 (2011), pp. 3956–3960.

[64] Tsuda, Y., et al, "Flight Status of IKAROS Deep Space Solar Sail Demonstrator," *Acta Astronautica* (2011), doi:10.1016/j.actaastro.2011.06.005.

[65] Wie, B., "Solar Sail Attitude Control and Dynamics, Part 1", *AIAA Journal of Guidance, Control, and Dynamics*, Vol. 27, No. 4 (2004), pp. 526-535. doi: 10.2514/1.11134

[66] Wie, B., "Solar Sail Attitude Control and Dynamics, Part 2," *AIAA Journal of Guidance, Control, and Dynamics*, Vol. 27, No. 4 (2004), pp. 536–544. doi: 10.2514/1.11133

[67] Wie, B., Thomas, S., Paluszek, M., Murphy, D., "Propellantless AOCS Design for a 160-m, 450-kg Sailcraft of the Solar Polar Imager Mission," *41st AIAA/ASME/SAE/ASEE Joint Propulsion Conference & Exhibit,* AIAA 2005-3928, 10-13 July 2005, Tucson, AZ. doi: 10.2514/6.2005-3928

[68] Wie, B., Murphy, D., "Solar-Sail Attitude Control Design for a Flight Validation Mission", *Journal of Spacecraft and Rockets*, Vol. 44, No. 4 (2007), pp. 809-821. doi: 10.2514/1.22996

[69] Weisstein, Eric W., "Fourier Series," *MathWorld*—A Wolfram Web Resource, http://mathworld.wolfram.com/FourierSeries.html, [cited 31 March 2015].

[70] Weisstein, Eric W., "Moment of Inertia." *MathWorld*—A Wolfram Web Resource. http://mathworld.wolfram.com/MomentofInertia.html [cited 31 March 2015].

[71] Wilkie, W. K., et al. "The Heliogyro Reloaded," *JANNAF 5th Spacecraft Propulsion Subcommittee Joint Meeting*, December 2011.

[72] Wilkie, W. K., et al., "Heliogyro Solar Sail Research at NASA," *3rd International Solar Sail Symposium*, Glasgow, UK, June 11-13, 2013, published in *Advances in Solar Sailing*, Vol. 1, Springer, Berlin, 2014, pp. 631-650. doi: 10.1007/978-3-642-34907-2.

[73] Wilkie, W., et al., "Recent Progress in Heliogyro Solar Sail Structural Dynamics," *European Conference on Spacecraft Structures, Materials and Environmental Testing*, Braunschweig, Germany, 1-4 April 2014.

[74] Wilkie, W. K., et al, "Recent Advances in Heliogyro Solar Sail Structural Dynamics, Stability, and Control Research," *2nd AIAA Spacecraft Structures Conference*, Kissimmee, FL, 5-9 January 2015. doi: 10.2514/6.2015-0431

APPENDIX A. COPERNICUS SETTINGS TO SIMULATE A SOLAR SAIL

These settings are under the Segment Definition > Maneuvers > Finite Burn tab. First, set the thrust magnitude in the Finite Burn Engine tab by selecting an engine control that includes Power to activate SEP. I use Cev & Power. Power and mass flow rate relate to thrust & Cev by:[55]

$$Power\ (W) = \frac{1}{2} Cev(km/s) \cdot 1000 \cdot Thrust(N) \tag{A.1}$$

$$\dot{m}(kg) = \frac{Thrust(N)}{1000 \cdot Cev(km/s)} \tag{A.2}$$

A solar sail has no mass flow rate, so I set Cev to an arbitrarily high 1e9 km/s. Calculate the thrust and power externally for a sail at 1 AU, as Copernicus does not have a solar sail module. Once an engine control with power is selected, activate SEP under Options > Power source > Solar Electric. This will automatically vary the thrust magnitude with distance from the sun. One can also select a shadowing model, if desired, to turn the thrust off in eclipse.

Next, set the thrust direction in the SOC FB Maneuver tab. Select a controls frame that points the thrust vector in the desired direction. For Earth escape, I choose the LVLH 2-body rotating frame with the sun as the main body (makes $\boldsymbol{s}$ the z-axis) and the Earth as the Aux body (makes $\hat{\boldsymbol{\imath}}$ the x-axis). A right ascension (Alpha) of 0° points thrust along the velocity vector, and declination (Beta) is the compliment of the thrust cone angle.

If the thrust magnitude and thrust cone angle vary continuously (e.g. OP $\mathbf{s}\|\ 0\tau$), I approximate the changes as piecewise linear. I calculate the thrust and declination externally to Copernicus from the data in Figure 3.9. I then perform a least squares fit to get the coefficients for input into Copernicus. The fits returned R^2 of 99.7% for declination and 97.6% for thrust magnitude, so the simulations are accurately representing the solar sail thrust.

APPENDIX B. ACRONYM GLOSSARY

AU	astronomical unit, 1 AU = 1.496e8 km, the average Earth-Sun distance
CM	center of mass
CMA	attitude control moment authority
CP	center of pressure
DCM	direction cosine matrix
DOF	degrees of freedom
EOM	equations of motion
FEA	finite element analysis
FEM	finite element model
FF	feed forward
FFT	fast Fourier transform
GEO	geosynchronous Earth orbit
GUI	graphical user interface
HELIOS	High-Performance, Enabling, Low-Cost, Innovative, Operational Solar Sail
IKAROS	Interplanetary Kite-craft Accelerated by Radiation of the Sun
JAXA	Japan Aerospace Exploration Agency
JPL	NASA Jet Propulsion Laboratory
LaRC	NASA Langley Research Center
LCD	liquid crystal device
LDV	laser Doppler vibrometer
LEO	low Earth orbit
LTI	linear, time-invariant

MIT	Massachusetts Institute of Technology
MSFC	NASA Marshall Space Flight Center
PD	proportional/derivative
PDFF	proportional/derivative/feed forward
PV	photovoltaic
RAAN	right ascension of the ascending node
RCD	reflectivity control device
RMS	root mean squared
SOCIT	System Observability Controllability Identification Toolbox
SOI	sphere of influence
SPO	solar polar orbiter
SRP	solar radiation pressure
SSO	Sun-synchronous orbit